Molecular beam epitaxy of GeTe-Sb_2Te_3 phase change materials studied by X-ray diffraction

D I S S E R T A T I O N

zur Erlangung des akademischen Grades

doctor rerum naturalium
(Dr. rer. nat.)
im Fach Physik

eingereicht an der
Mathematisch-Naturwissenschaftlichen Fakultät I
Humboldt-Universität zu Berlin

von
Herr M. Sc. Roman Shayduk

Präsident der Humboldt-Universität zu Berlin:
Prof. Dr. Dr. h.c. Christoph Markschies

Dekan der Mathematisch-Naturwissenschaftlichen Fakultät I:
Prof. Dr. Lutz-Helmut Schön

Gutachter:
1. Prof. Dr. Klaus H. Ploog
2. Prof. Dr. Ted Masselink
3. Prof. Dr. Andreas Wieck

eingereicht am: 26 Oktober 2009
Tag der mündlichen Prüfung: 20 Mai 2010

Here I express my deepest gratitude to my wife Elena for all the asperities and problems she had to overcome during my work (e.g. my absence during night shifts, conferences and others). She was always delivering me her love and care I needed so much and through the whole work. This work would not be finished without her and I dedicate this work to her.

Abstract

The integration of phase change materials into semiconductor heterostructures may lead to the development of a new generation of high density non-volatile phase change memories. Epitaxial phase change materials allow to study the detailed structural changes during the phase transition and to determine the scaling limits of the memory. This work is dedicated to the epitaxial growth of Ge-Sb-Te phase change alloys on GaSb(001). We deposit Ge-Sb-Te (GST) films on GaSb(001) substrates by means of molecular beam epitaxy (MBE). The film orientation and lattice constant evolution is determined in real time during growth using grazing incidence X-ray diffraction (GID). The nucleation stage of the growth is studied *in situ* using reflection high energy electron diffraction (RHEED).

Four growth regimes of GST on GaSb(001) were observed: amorphous, polycrystalline, incubated epitaxial and direct epitaxial. Amorphous film grows for substrate temperatures below 100 °C. For substrate temperatures in the range 100–160 °C, the film grows in polycrystalline form. Incubated epitaxial growth is observed at temperatures from 180 to 210 °C. This growth regime is characterized by an initial 0.6 nm thick amorphous layer formation, which crystallizes epitaxially as the film thickness increases. The determined lattice constant of the films is 6.01 Å, very close to that of the metastable GST phase. The films predominantly possess an epitaxial cube-on-cube relationship. At higher temperatures the films grow epitaxially, however the growth rate is rapidly decreasing with temperature. At temperatures above 270 °C the growth rate is zero.

The composition of the grown films is close to 2:2:5 for Ge, Sb and Te, respectively. The determined crystal structure of the films is face centered cubic (FCC) with a rhombohedral distortion. The analysis of X-ray peak widths gives a value for the rhombohedral angle of 89.56 °. We observe two types of reflections in reciprocal space indicating two FCC sublattices in the structure. The analysis of X-ray structure factors give the same averaged electron density ratio in the two FCC sublattices as in the GeTe or the metastable $Ge_2Sb_2Te_5$ with 20% vacancies. No tetrahedrally coordinated atoms are observed.

Zusammenfassung

Die monolithische Integration von Phasenwechselmaterialien mit Halbleiter-Heterostrukturen eröffnet neue Perspektiven für zukünftige Generationen von nichtflüchtigen Speicherbauelementen. Diese Arbeit befasst sich mit dem epitaktischen Wachstum von Ge-Sb-Te Phasenwechselmaterialien. Dazu wurden Ge-Sb-Te(GST) Schichten mittels Molekularstrahlepitaxie (MBE) auf GaSb(001)-Substraten abgeschieden. Die kristallografische Orientierung und die Veränderungen der Gitterkonstante während des Wachstums wurden mittels Röntgenbeugung unter streifendem Einfall (GIXRD) bestimmt. Das Nukleationsverhalten zu Beginn des Wachstums wurde mittels Hochenergie-Elektronenbeugung unter streifendem Einfall (RHEED) untersucht.

Das Wachstum kann an Hand der Substrattemperatur in vier Bereiche unterschieden werden: amorph, polykristallin, inkubiert epitaktisch und epitaktisch. Amorphe Filme wachsen bei Substrattemperaturen unter 100 °C. Für Substrattemperaturen zwischen 100 und 160 °C wächst die Schicht in polykristalliner Form. Inkubiertes epitaktisches Wachstum wird bei Substrattemperaturen zwischen 180 und 210 °C beobachtet. In diesem Bereich bildet sich zunächst eine 0.6 nm dicke amorphe Schicht, die bei weiterem Wachstum kristallisiert. Die Gitterkonstante des epitaktischen GST beträgt 6.01 Å, was dem Literaturwert für die metastabile kubische Phase des GST in gesputterten Filmen sehr nahe kommt. Die Epitaxie bildet eine dominante kubisch-auf-kubisch-Orientierung aus. Bei höherer Substrattemperatur wachsen die Schichten direkt ohne amorphe Schicht epitaktisch auf das Substrat auf, die Wachstumsrate geht jedoch mit zunehmender Temperatur rapide zurück. Oberhalb von 270 °C ist die Wachstumsrate null.

Die chemische Zusammensetzung der abgeschiedenen Filme liegt in der Nähe von 2:2:5 für Ge:Sb:Te. Die Kristallstruktur der Filme ist kubisch flächenzentriert (FCC) mit einer rhomboedrischen Verzerrung. Aus der Breite der Röntgenbeugungsreflexe ergibt sich ein Rhomboederwinkel von 89.56°. Im reziproken Raum können zwei Arten von Reflexen unterschieden werden, woraus sich die Existenz zweier FCC-Untergitter in der Struktur ergibt. Eine Analyse der Röntgenstrukturfaktoren ergibt dasselbe mittlere Elektronendichteverhältnis in den beiden FCC-Untergittern wie in GeTe oder $Ge_2Sb_2Te_5$ mit 20% Leerstellen. Tetraedrisch koordinierte Atome konnten nicht nachgewiesen werden.

Abbreviations

AFM	Atomic Force Microscopy
BCC	Body Centered Cubic
DSC	Differential Scanning Calorimetry
EBSD	Electron Back-Scattering Diffraction
EXAFS	Extended X-ray Absorption Fine Structure
FCC	Face Centered Cubic
FWHM	Full Width at Half Maximum
GID	Grazing Incidence Diffraction
GST	Ge-Sb-Te
HRTEM	High Resolution Transmission Electron Microscopy
MBE	Molecular Beam Epitaxy
PCM	Phase Change Materials
RHEED	Reflection High Energy Electron Diffraction
SEM	Scanning Electron Microscopy
UHV	Ultra High Vacuum
XAFS	X-ray Absorption Fine Structure
XANES	X-ray Absorption Near Edge Structure
XRD	X-ray diffraction
1D	One-dimensional
2D	Two-dimensional
3D	Three-dimensional

Contents

Introduction

Motivation. It is difficult to overestimate the role of electronic equipment in everyday life. If one looks carefully around, it is amazing how much and important work we entrust to digital electronics today. A pilot, for example, manages an airliner relying only on what is shown on a computer screen. Diagnostic devices in medicine are now more and more equipped with electronics. One cannot imagine our entertainment hours without something containing electronics.

In the heart of almost any electronic device there is an integrated circuit, implementing basic computation or/and memory functions. The circuit consists of a few types of logical elements, like transistors, capacitors and resistors. The more elements are present in the circuit, the more data can be stored, the smaller the size of the elements and the faster the calculation.

In 1965 Gordon Moore [1] published his observation that the number of elements in a single silicon chip increases by a factor of two every two years. This rate of progress was astonishing, but even more so is the fact that his predictions are still essentially true today. For example, in 1970 the Intel 4004 processor had a few thousands transistors. It has now evolved into the Intel Pentium QuadCore with a few billion transistors per chip. The fast growth in the number of elements per chip was only possible due to the colossal effort directed to making transistors smaller. Usually, the limiting factor preventing further miniaturization is the smallest possible feature size in the photolithographic process. Since the smallest feature size in photolithography is determined by the wavelength, size reductions are often achieved by shifting the wavelength used to smaller lengths, and finding appropriate photosensitive materials.

If the progress of miniaturization proceeds at the same rate, the transistor gate sizes will shrink to 20 nm in about 2016 [2]. With the advent of this length scale, problems with leakage currents will become dominant, and will act to limit the miniaturization process [3, 4, 5]. Therefore, a new concept, quite likely beyond charge manipulation is required.

Data storage devices are probably the most widely used components of modern digital electronics. The wide variety of requirements of electronics cannot be fulfilled by a single memory type. Thus, memory technologies are less unified than their computation counterparts. For example, the main computer memory DRAM (dynamic random access memory) is made of CMOS and based on charge storage. It is fast, but the drawback is that it requires constant power to not loose its information. As hard disk memory is based on magnetic domains, it does not require power to maintain the data, but it is very slow compared to DRAM and cannot serve as the main computer memory. Furthermore, the presence of a read-write head a hundred nanometers away from the disk surface makes the whole device shock sensitive. FLASH memory is compact and non-volatile, but expensive, very slow and has now exhausted its scaling possibilities.

As an alternative to charge storage memory, three generations of quite novel non-volatile optical memory already exist. These are the CD (compact disk), DVD (digital

versatile disk) and Blue-ray disks. This technology has been rapidly developing since 1990, and nowadays a lot of disk types are available. Second and third generation disks are now unified by using the same physical phenomenon, which is an order-disorder phase transition under a laser pulse irradiation[6, 7, 8]. Different values of the optical constants in the amorphous and crystalline states are used to store the data. The choice of working material has fallen on doped Ge-Sb-Te chalcogenide glasses [9, 10].

Scientific research activity in the field of Ge-Sb-Te chalcogenides (which are now called phase change materials) has been increasing dramatically during the last fifteen years. The reasons are the approaching limits of CMOS technology and, at the same time, the potentials of Ge-Sb-Te based phase change materials for electrically switched memory. From the discovery of chalcogenide glasses, some time ago already [11], it was known that the phase transition could be induced by an electric current pulse. However, the technology was not commercialized due to the ultra high power consumption during switching. Today, the situation has changed. Optimizing the chalcogenide materials for DVD, people noticed that the switching time of the material can be as short as few tens of nanoseconds [12], which immediately surpasses FLASH and HDD technology. There are reports on phase change memory cells surviving up to 10^{12} switching cycles without bit loss [13, 14]. The switching properties of the material are getting better as the size shrinks [15], due to the reduction in power-voltage requirements, which in turn opens the door for further miniaturization. Phase change memory has a low sensitivity to radiation and magnetic fields. It can even be easily integrated with CMOS technology. With all these advantages, the main one remains - phase change memory is non-volatile. Therefore, today Ge-Sb-Te based phase change materials are seriously considered by big companies (IBM, STMicroelectronics) as a replacement of FLASH technology and even DRAM. It would be very attractive to be able to turn on your computer and have it ready immediately. You would not need to beg a service company to restore your data from the hard disk you dropped or from a cracked DVD. Memory cards with phase change technology could be several orders of magnitude faster and more durable.

Considering not only chalcogenide glasses, huge efforts have been directed to the search of the best phase change material. To the moment, some of the best switching properties are found for materials lying near the GeTe-Sb_2Te_3 pseudobinary line [16, 17, 18]. Despite rather good progress in the material search, there is still no complete theory which can explain the ultra fast switching speed, high stability and high endurance of the Ge-Sb-Te alloys. If one could provide such a theory, one would tremendously simplify the search and optimization of new materials.

A major breakthrough in understanding the switching of $Ge_2Sb_2Te_5$ phase change material is the "umbrella flip" model [19]. This model proposes a local mechanism of phase transition, where no big diffusion of atoms is required. There is only one species of atoms performing site-to-site jumps, while other atoms remain basically in place during the process.

Currently, the majority of phase change studies are made on sputtered samples, where orientational disorder complicates the atomic structure study during the amorphization–crystallization cycle. If it were possible to orient each individual crystal coherently with the others, it could significantly simplify the structure study during switching. Molecular beam epitaxy (MBE) is the ideal method for doing this. Moreover, molecular beam epitaxy allows for sub-monolayer control of thicknesses, which allows to investigate the full scaling potential of phase change materials.

The bulk growth of Ge-Sb-Te alloy single crystals due to the high temperature required leads to the growth of the hexagonal phase stable at higher temperatures. However, it was shown [20] that fast switching occurs in between the amorphous and metastable cubic phases. The lattice constant of cubic metastable Ge-Sb-Te is 6.02A, closely matching that of GaSb and InAs substrates. Thus, it is very interesting to investigate the possibility of epitaxial growth of Ge-Sb-Te alloys on these substrates.

Goals and results

The aim of the research. The aim of this research is to investigate the possibility of epitaxial growth of $Ge_2Sb_2Te_5$ phase change materials. The aim involves:

- Developing a method for preparing an atomically smooth GaSb(001) surface.
- Developing a method for calibration of the Ge, Ga, Sb and Te effusion cells.
- Performing growth experiments of Ge-Sb-Te on GaSb(001) wafers. Determination of the film orientation on the surface.
- Determination of the film parameters: density, thickness, surface roughness, interface roughness.
- Determination of the growth phase diagram indicating different growth regimes: amorphous, polycrystalline, incubated epitaxial and epitaxial.
- Determination of material growth rate depending on substrate temperature
- Suggestion of a growth mechanism explaining the observed growth behavior.
- Data acquisition optimization with six circle diffractometer
- Development of a method for crystal structure analysis of epitaxially oriented Ge-Sb-Te phase change materials
- Determination of the crystal structure of the film

Scientific novelty. In this work, the epitaxy of Ge-Sb-Te phase change materials has been demonstrated for the first time. The epitaxial cube-on-cube orientation of the metastable $Ge_2Sb_2Te_5$ has been demonstrated, which is of paramount importance for successful crystal structure determination and switching studies.

A poor temperature stability of epitaxial Ge-Sb-Te phase change material films in vacuum was discovered. This significantly complicates annealing experiments with the film. It was also shown that a relatively thick film desorbs non-congruently upon annealing, leaving a pure Ge film on the surface, while a thin film can be desorbed completely. An effect of Te etching of the Ge-Sb-Te film has been discovered at elevated temperatures. It was shown that an initially nucleated Ge-Sb-Te alloy could be completely removed from the surface upon annealing above 300 °C and simultaneous supply of Te flux.

A mechanism of epitaxial growth was suggested for Ge-Sb-Te alloys on GaSb(001).

A thermodynamical approach to explain the high film volatility of Ge-Sb-Te alloys under vacuum conditions was suggested.

During the work, a motor synchronization algorithm was developed for diffractometers with complicated geometry. It was shown that the X-ray data acquisition rate

could be enhanced by almost factor of two in a conventional six circle diffractometer if synchronization was used.

For non-synchronized diffractometer movements during a stepped scan, the maximum deviation from trajectory points in reciprocal space was evaluated. The error-free scan directions in reciprocal space have been identified. The algorithm has been experimentally proven and implemented at our PHARAO beamline diffractometer.

Scientific and practical value. The fabricated epitaxial films are now being used in laser switching experiments within the PHARAO phase change project. The films promise to provide direct access to the structural changes during switching. The suggested phase diagram curve for Ge-Sb-Te alloys is playing a key role in the epitaxy of these materials. The desorption rate approach used in this work could be extended to all common chemical elements used in MBE, allowing a new substrate temperature calibration method. The suggested advanced data acquisition method is actively used with our six circle diffractometer and could be used in many other diffractometers with complicated geometry worldwide.

Reliability of the results is assured by the use of an advanced molecular beam epitaxy and X-ray diffraction setup. The first results of the work are already published in international high impact journals (Journal of Applied Crystallography, Applied Physic Letters, Journal of Crystal Growth). The growth results were presented at International (Vancouver 2008) and European (Zakopane 2009) conferences on molecular beam epitaxy.

Contribution from the author. All the epitaxial growth methods were developed and growth results were acquired by the author himself. The diffraction methods were developed and the crystal structure was determined by the author himself. The laser switching results are achieved by the collaborating colleagues Timur Flissikowski and Manfred Ramsteiner at PDI. In the film properties analysis like composition and resistivity, several collaborative and non-collaborative external colleagues were involved. During the work, the author has participated in the PHARAO beamline upgrade. The X-ray synchrotron beamline alignment procedure was guided by the author.

Publications. The author of the work has also significantly contributed to the *in situ* X-ray characterization of Fe_3Si/GaAs(001) growth, which results are not described in this manuscript. These results and the results of this work are published [21, 22, 23, 24, 25].

Main results of this work. The main results of the work are:

1. Motor synchronization algorithm for continuous scans in complicated geometries, allowing for faster data acquisition rate.

2. Epitaxy as a method for fabricating the oriented cubic phase of GeTe-Sb_2Te_3 alloys.

3. A growth phase diagram and its explanation. Statement that epitaxy of cubic GeTe-Sb_2Te_3 phase at high temperatures would not be possible due to high volatility of the material.

4. Crystal structure of epitaxial GeTe-Sb_2Te_3 phase change alloys and the determination method.

Structure of the manuscript. The manuscript consists of introduction, goals and results, 5 chapters and a summary.

In the first chapter we give a short introduction to the field of phase change materials. We focus on the known structure details of GeTe-Sb_2Te_3 pseudobinary alloys, which are studied in this work.

The second chapter contains three main sections. In the first two sections the basic formulas of the X-ray kinematical theory are derived and the main components of our experiment are described. The third section is the author's original work in which the experiment for the X-ray structure factors determination is designed and the necessary geometry corrections are derived.

The third chapter is more technical and contains two main sections. In the first section a synchronization method for diffractometer stepper motors is developed, which allows for continuous data sampling in the reciprocal space. For the case of non-synchronized movements, the deviation of the sampling point in hkl space is calculated, which describes the second section. Since the calculations yield a small deviation values for our experimental geometry, the method was implemented, and the validity of the approach was proven experimentally with our six-circle diffractometer.

The growth experiments of GeTe-Sb_2Te_3 alloys on GaSb(001) are described in the chapter four, which is divided onto 5 sections. First, we describe the preparation procedure of atomically smooth GaSb(001) surface by molecular beam epitaxy. The second section describes and discusses the whole growth process of Ge-Sb-Te alloy on GaSb(001) at 200 °C controlled by reflection high energy electron diffraction and X-ray diffraction. The initial structure details are extracted. In the third section the growth process of GST on GaSb(001) at various temperatures is discussed. Section four describes the obtained physical and laser-induced switching properties of the fabricated film. In the section five, the poor temperature stability of the fabricated films in vacuum is discussed. This section summarizes the growth experiments of Ge-Sb-Te alloys on GaSb(001).

The chapter five describes the determined crystal structure of the fabricated films. It is divided on the three sections. First, we describe the film orientation on GaSb(001) substrate. In the second section we determine the detailed structure of the film by analyzing the obtained X-ray structure factors. The emphasis is made on the determination of the averaged electron density in the Ge-Sb sublattice, and the analysis of the possibility to have tetrahedrally coordinated Ge atoms. The third section discusses the observed X-ray peak broadening effects. Broadening due to rhombohedral/tensile strain and size effects are separated.

The last chapter summarizes the results of this work.

1 Phase change materials

In this chapter we focus on the structural and growth-related properties of GeTe-Sb_2Te_3 phase change materials to introduce the background for the interpretation of the results. The more general properties of phase change materials will also be briefly reviewed. For more details, we refer the reader to several excellent review articles on phase change materials [18, 26, 17, 27].

1.1 The discovery of phase change materials

The idea of engineering logical switches for electronics based on phase transition phenomena was born with the discovery of electric current driven phase transitions.

In 1968, Stanford Ovshinsky published a paper describing an unusual voltage-current characteristic of thin films made of chalcogenide glasses [11]. The effect is qualitatively shown on Fig. 1.1. Applying an electric signal to the thin sputtered films sandwiched in between two carbon electrodes he observed few orders of magnitude resistance drop as the voltage reached a certain threshold value u_{th}. At this stage, the resistance of the film was not ohmic and the current could be varied without significant changes in voltage. When the current dropped below a certain threshold value, the material switched back to highly resistive state. Today, this effect is called "threshold switching".

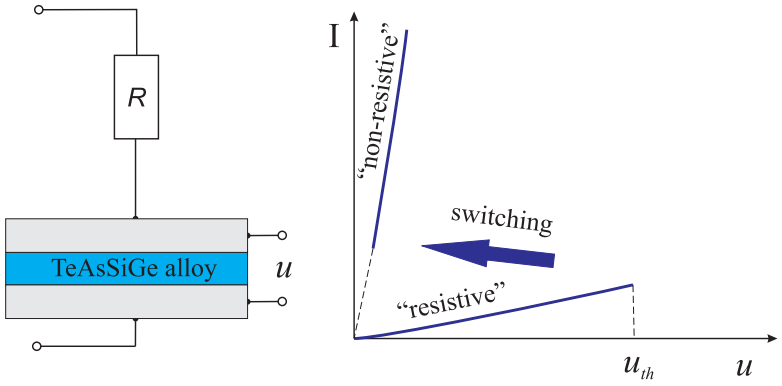

Figure 1.1: Qualitative representation of Ovshinsky threshold switching I-V curve and schematic of experimental setup.

Varying the composition of the film he observed a "memory effect" so that the material, once switched, stayed in a highly conductive state even for zero voltage.

Ovshinsky patented his invention, however the switch was never commercialized due to the extremely high pulse energies required for the switching. Rapidly developing complementary metal-oxide-semiconductor (CMOS) technology at that time produced much less energy consuming switches. This was the first time phase change materials were suggested for electronic memory applications and logical switches.

For some materials it was shown that after the threshold switching the atomic structure changes from an amorphous disordered state to more ordered polycrystalline state causing the strong changes in electrical conductivity to remain.

Two years later, Ovshinsky's colleagues showed that reversible crystallization and amorphization of these materials could be induced optically by a laser pulse. They emphasized that under simple annealing the crystallization can take hours, while the same material crystallizes in microseconds by a laser pulse [28]. This was the start of a discussion whether this phase transition is a purely thermal effect or of electronic nature. To the present day this question still remains [29]. Since there is a wide range of materials with phase change properties, there may be no general answer to this question applicable for all the materials, and one may have to focus on peculiar material system.

1.2 Laser induced phase transitions

In contrast to the electrical switch which has never been commercialized, optical switching found its application in CD-RW, DVD-RAM, DVD-RW (Sb-Te alloys) and rewritable Blue-ray disks [16, 6, 9]. Different optical constants of amorphous and crystalline material allow for the distinction between the crystalline and the amorphous phase in this application.

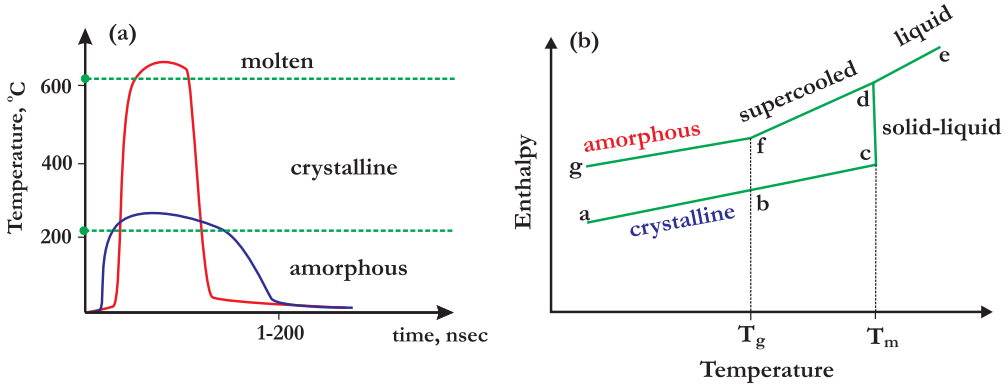

Figure 1.2: Qualitative picture of melt-quench amorphization and recrystallization process: (a) the temperature-time plot, (b) thermodynamical pathways of phase transitions

Figure 1.2(a,b) shows how the majority of phase change optical disks work. In the simplest picture, a small region of initially crystalline film is amorphized by a short laser pulse. Due to the high power of the pulse, the phase change layer locally melts introducing structural disorder. Then, the small mark quenches rapidly. Having no time for recrystallization, the film goes through a supercooled state and freezes in glassy state. To erase the recorded mark, a weaker but longer pulse is applied. The amorphous mark recrystallizes under laser irradiation due to thermal heating. In this case, the power is adjusted to heat the film just above the glass transition temperature and the duration is optimized to allow for crystallization to finish. The limiting factor for the fast and reversible switching in phase change memory has always been the longer crystallization time [30], but not the amorphization.

1.3 GeTe-Sb_2Te_3 pseudobinaries

The commercial success of optical disk memories lead to an optimization of phase change material properties. The best properties in terms of speed and stability were found for materials lying along the GeTe-Sb_2Te_3 pseudobinary line [27] (see Fig. 1.3).

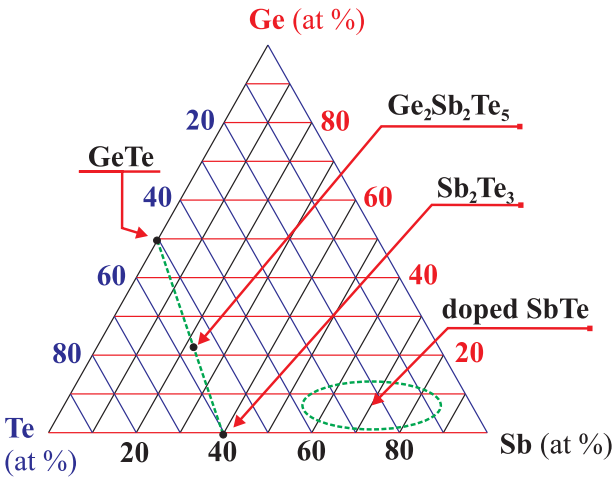

Figure 1.3: Ternary Ge-Sb-Te phase diagram. The GeTe-Sb_2Te_3 pseudobinary line is indicated by a dashed line.

In spite of good success in finding better materials, the reason for the fast crystallization of GeTe-Sb_2Te_3 pseudobinaries still remains unclear. To understand this mechanism, it is absolutely important to reveal the details of the nanometer-scale process of atomic rearrangement during phase transition.

There is an interesting structural detail known about this material, which can serve as the starting point. Figure 1.4 shows the phase diagram of GeTe-Sb_2Te_3 pseudobinary alloys, redrawn from the Abrikosov and Danilova-Dobryakova paper [31]. Mixing the two binary compounds GeTe and Sb_2Te_3, they examined the microstructure of the solidified alloy by optical microscopy. Changing the ratio of GeTe to Sb_2Te_3 they observed a homogeneous microstructure for exactly stoichiometric ratios: $(GeTe)_2$:Sb_2Te_3, GeTe:Sb_2Te_3 and GeTe:$(Sb_2Te_3)_2$. We will call these compositions the stoichiometric ternary alloys.

The crystal structure of pure GeTe is rhombohedral, but is very close to the cubic sodium chloride structure, since the rhombohedral angle is close to 90° [32]. This is schematically shown on Fig. 1.4 by a cubic shape. The crystal structure of pure Sb_2Te_3 is hexagonal [33, 34] with a relatively long stacking along the c axis, which is schematically shown in Fig. 1.4 by a hexagonal shape. The equilibrium crystal structure of all stoichiometric ternary alloys is hexagonal. These hexagonal structures are very similar because in the hexagonal plane the lattice constants are very close (4.22 Å within 0.3%)[35, 36]. The main difference is the stacking of the atoms along the c axis, which can vary from 16 Å to 60 Å[37, 38, 39]. However it was shown, that the fast and reversible phase transition under laser pulse irradiation does not occur between the stable and amorphous phases, but between the amorphous and metastable cubic phase [36]. The crystallization of these alloys occurs in two steps, which is clearly seen in

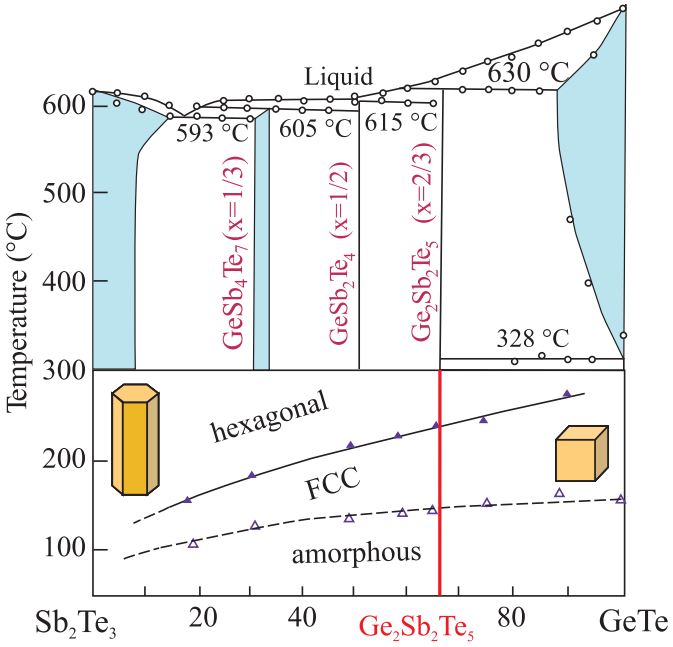

Figure 1.4: Phase diagram of $(GeTe)_x(Sb_2Te_3)_{1-x}$ pseudobinary alloy with three stoichiometric ternary compounds.

temperature dependent resistivity measurements and differential scanning calorimetry experiments [8]. At moderate temperatures (around 200 °C) the alloys crystallize into a metastable cubic phase, while the atomic ordering into the large unit cell equilibrium phase occurs at relatively high temperatures above 300 °C. Therefore, the fast and stable phase transitions are believed to be due to the similarity of the atomic arrangement in the amorphous and metastable crystalline phases.

1.4 Crystal structure of $Ge_2Sb_2Te_5$

The crystal structure of stoichiometric $Ge_2Sb_2Te_5$ (GST) used in DVD-RAM was studied before [35]. Figure 1.5(a) shows the unit cells of thermally stable hexagonal GST and metastable NaCl-like cubic GST. The cubic GST structure is different from the ideal sodium chloride structure in several respects: it has a small rhombohedral distortion towards the (111) direction; all the Te, Sb and Ge atoms are slightly shifted from the ideal distorted sodium chloride lattice points; Te fully occupies one face centered cubic (FCC) sublattice, while Ge and Sb randomly occupy another FCC sublattice; there are 20 % vacant sites in the Ge-Sb FCC sublattice. The reported lattice constant of cubic GST is 6.02 Å.

The hexagonal GST phase has a lattice constant of a=4.22 Å and c=17.24 Å. It possesses a 9-layer stacking along the c-axis: Te-Ge-Te-Sb-Te-Te-Sb-Te-Ge. The similarity of the metastable cubic and the hexagonal phases of GST can be found after careful inspection of a small crystal made of 6×6×2 hexagonal unit cells shown on Fig. 1.5(b). On this picture we can clearly see that the crystal, actually, contains cubic units of the metastable cubic structure. The problem why the whole crystal cannot be imagined

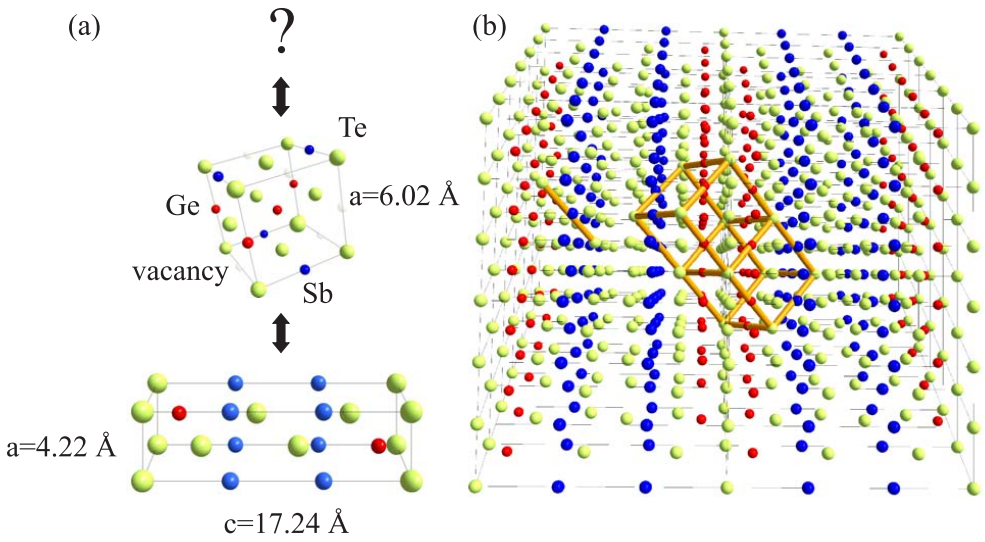

Figure 1.5: Crystal structures of metastable and thermally stable $Ge_2Sb_2Te_5$ compound.

as having a distorted sodium chloride structure is the presence of Te-Te stacking. One cannot just continue this cubic sublattice without introducing misfit dislocations at the Te-Te plane. If we look on a cubic GST phase in hexagonal notation, the stacking along the c-axis (equivalent to the (111)-axis in cubic notation) thus would be the following: Te-(Sb or Ge or vacancy)-Te-(Sb or Ge or vacancy)-Te, thus always alternating with the Te layers. There are no two adjacent Te-Te layers present in the cubic phase. Thus we conclude that the hexagonal phase is also similar to the cubic phase, but it is just more ordered, so that all Ge and Sb atoms have formed layers, including vacancies, which form a "vacancy layer" in between two adjacent Te-Te layers of the stable hexagonal phase [40, 41].

Despite strong efforts directed towards resolving the atomic arrangement of the amorphous GST phase, the structure still remains unclear. The reason is in the word "amorphous" itself. Due to the lack of long-range order, there are only a limited number of methods which allow probing the structure directly. There is also no unified theory of glasses, so that it is even difficult to give a definition for a glass. In the simplest picture, glass is a material without long-range order, easily distinguishable from a crystal using diffraction methods. The chalcogenide glass seems one of the more complicated ones, since it is believed that it keeps various types of ordering even in the glassy state. Various attempts were made to detect and classify the ordering in GST glass [42, 43, 44]. There is an interesting idea that the atomic arrangement in the laser-amorphized GST may be not so different from that in the crystalline GST. Fast and stable switching in this picture is attributed to a local mechanism of phase transition where atoms do not migrate far away during switching.

A particulary interesting model explaining fast phase transitions in stoichiometric $(GeTe)_2Sb_2Te_3$ has been suggested by Kolobov et al. [19], where Ge atoms perform site-to-site jumps locally. They also show experimentally that the amorphization of GST completes in less then one nanosecond [12]. At the same time, theory, using molecular dynamics simulation methods, demonstrates that for GST, the crystallization

completes within a nanosecond even without the requirement for the locality of atom rearrangements [45]. Thus, there is still no direct evidence of a local mechanism of the phase transition. However, the umbrella flip model proposed by Kolobov et. al. at least suggests along which direction we should think if we want to find optimal materials for fast and stable switching. The model is described in more detail below.

1.5 The umbrella flip in the $Ge_2Sb_2Te_5$ compound

One of the methods to probe short-range atomic arrangement in both amorphous and crystalline solids is the analysis of X-ray absorption fine structure (XAFS). The technique is elementally sensitive and allows the determination of several material properties: the number of nearest neighbors for a specific atom type, the distance from a specific atom type to a certain kind of nearest neighbor atom and the degree of disorder at that distance [46]. Kolobov et al. used the method to study the local atomic arrangement in the vicinity of the Ge, Sb and Te atoms in amorphous and polycrystalline GST films. They used real device samples with sputtered GST films being switched by a laser.

By probing the germanium and antimony absorption edges, it was shown that in the crystalline state the Ge and Sb atoms have only Te atoms as nearest neighbors. This means that Ge and Sb do not intermix, and are always separated by the Te face centered cubic sublattice. This also implies that the GST alloy does not phase separate for Te-poor Ge-Sb-Te inclusions which is important for successful epitaxy.

Two types of Ge-Te and Sb-Te bonds were detected. Longer 3.2 Å Ge-Te and Sb-Te bonds and shorter bonds, 2.91 Å and 2.83 Å for Sb-Te and Ge-Te, respectively. The average bond length was 3.01 Å in agreement with X-ray data. Thus, the unusually large mean atomic displacement for the Ge-Sb sublattice detected by X-rays is due to the presence of shorter and longer bonds.

The coordination number determined for each atom is approximately half that of the ideal NaCl structure which has six nearest neighbors for each atom. This supports the X-ray observations where a large number of vacancies were detected in the Ge-Sb sublattice [36, 35, 20].

The observations above suggest that the crystal structure of metastable GST is buckled. The distorted geometry of the GST unit cell is attributed to a complicated bonding configuration. Traditionally, group IV semiconductors share eight valence electrons to create four covalent bonds. A similar situation exists in most of the III-V semiconductors having the zinc blende structure. Ge-Sb-Te in the NaCl structure has an insufficient number of electrons to saturate all three bonds for each atom. It is very interesting that only for the 2:2:5 composition the number of vacancies calculated from electron counting rules yields exactly 20%, which is the number of vacant places in the Ge-Sb sublattice inherited from the NaCl structure of GST. Thus, the high number of vacancies containing no bonding electrons is somewhat natural, and leads to the distortion of the GST unit cell. Therefore, due to the introduced asymmetry, shorter and longer bonds naturally appear in the structure.

When the film is switched into the amorphous state, a drastic change in the structural properties occur. The Ge-Te bond length shrinks significantly down to 2.61 Å while the Sb-Te bonds decreases to 2.85 Å. The Te-Te second nearest neighbor peak weakens. The XAFS spectra in general possess much more pronounced oscillations resulting in

sharp peaks corresponding to nearest neighbor distances. This indicates that locally, the amorphous phase is more ordered then the crystalline phase due to more rigid bonds. It is worth mentioning that the observed Ge-Te and Sb-Te bond lengths in the amorphous state are equal to the sum of the covalent radii of the corresponding elements [47].

Taking into account these experimental observations, Kolobov et al. suggested the following. The cubic phase of GST acts similar to a molecular crystal, in that intramolecular forces are stronger than intermolecular forces. The lattice is constructed out of rigid molecular building blocks. Figure 1.6(c) shows a fragment of cubic GST with such a rigid block having the formula 2:2:5. The block contains a vacancy in the center and has strong intramolecular bonds. If the whole lattice is made out of such blocks, rotated by 90 degrees in arbitrary directions, we get a buckled NaCl structure, where Te fully occupies one FCC sublattice, while Ge, Sb and vacancies occupy another FCC sublattice. During amorphization, the Ge atoms change from octahedral coordination

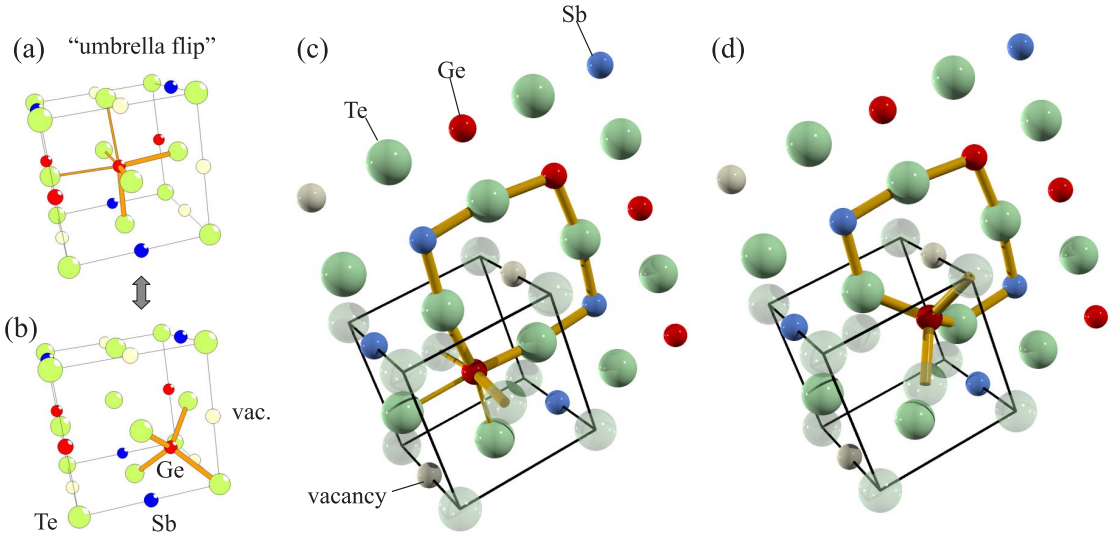

Figure 1.6: The suggested umbrella flip switching mechanism. (a) Octahedral germanium with strong short bonds and weaker long bonds. (b) Switched unit cell with tetrahedral germanium. (c) Rigid building block of GST molecule 225 with vacancy, strong intramolecular bonds and octahedral germanium. (c) Switched state with tetrahedrally coordinated germanium.

to tetrahedral coordination (see Fig. 1.6(d)) without breaking of strong covalent bonds, thus making an umbrella-like flip. During the process, the intermolecular bonds further weaken resulting in higher disorder on the long-range scale, while, at the same time, allowing the molecular blocks to obtain a more rigid form on the short range scale.

While this proposed mechanism is speculative, there are reports based on transmission electron microscopy (TEM) observations of such tetrahedral stacking of Ge atoms in the matrix [48, 49]. This structure is observed at the boundaries of "truly" amorphous and crystalline phases. It should be said that a laser amorphized structure is assumed to be different from that of the as-deposited structure, since it possesses different XAFS spectra and switching properties [50]. The as-deposited amorphous GST contains more "wrong bonds" like Ge-Ge or Sb-Sb than the laser-amorphized GST, which slows down

the recrystallization process. Therefore, there is no doubt that with a strong enough laser pulse the GST film can be really melted forcing the diffusion of atoms. The idea is that the GST material could exhibit more delicate reversible structural changes under a weaker pulse.

2 Development of diffraction methods for epitaxial phase change materials

This chapter is divided in three sections. In the first section, the basic equations of the kinematical scattering theory of X-ray diffraction are derived. The described theory neglects absorption and extinction effects and is applicable for thin epitaxial films. This section focuses on the equations used in X-ray crystallography, which allow the determination of structure factors and atomic scattering factors. The obtained equations were used for the determination of the crystal structure of epitaxial GeTe-Sb_2Te_3 films. The integrated intensity concept for the general case of imperfect crystals is not derived here, but postulated.

The second section describes the basic theoretical principles of molecular beam epitaxy. The main components of the combined six-circle diffractometer and molecular beam epitaxy machine used in the experiment are described. The main beamline components are also described.

The third section is the author‘s original work. Due to the broad X-ray reflections obtained from the epitaxial films produced in this work, an alternative approach had to be developed in order to obtain integrated intensities of the X-ray reflections. The necessary geometrical correction factors to the integrated X-ray reflections are derived to allow designing the experiment for the film structure factor determination.

2.1 Fundamentals of crystal structure determination by X-rays

In this section we present the main formulas of the kinematical theory of X-ray scattering. For a deeper understanding of X-ray kinematical theory we encourage the reader to get acquainted with the corresponding literature [51, 52].

2.1.1 Atomic scattering factors of Te, Sb and Ge

Let us consider a linearly polarized plane electro-magnetic wave scattered from a single atom. According to [51, 52] the amplitude of the elastically scattered wave at the point of observation is determined by the relation:

$$E = E_e f \tag{2.1}$$

where f is the so-called atomic scattering factor, and E_e is called the amplitude of classical scattering by a single electron, which has the form:

$$E_e = E_0 \frac{e^2}{m_e c^2 R} P^{\frac{1}{2}} \tag{2.2}$$

where E_0 is the amplitude of incoming wave, e is the electron charge, m_e is the electron mass, c is the speed of light, R is the distance to the observation point and P is a polarization factor. Here we use cgs units. It is easy to derive that for a linearly polarized wave, the polarization factor P takes the form:

$$P = \sin^2(\angle(\vec{E}_0\vec{R})) \tag{2.3}$$

With a high degree of accuracy, synchrotron radiation is linearly polarized in the horizontal plane [53]. Therefore, for grazing incidence, the polarization factor takes the form:

$$P \approx \cos^2(\gamma) \tag{2.4}$$

where γ is the corresponding detector angle. For the non-grazing case one can find the matching relation in the literature [54]. We see that in the horizontal plane, scattering at 90 degrees is absent.

The atomic scattering factor f accounts for the interference of X-rays scattered from an atomic electron density distribution, and in the general case is given by the complex value:

$$f = f_0 + f_1 + if_2, \tag{2.5}$$

where f_0 is the atomic scattering factor for the case of no absorption while f_1 and f_2 are the real and imaginary parts of the anomalous dispersion correction.

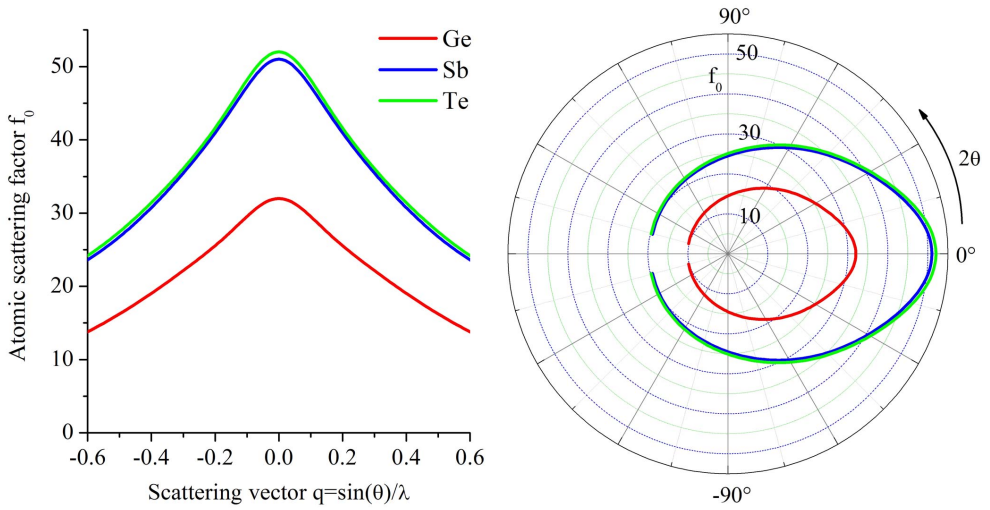

Figure 2.1: (a) Atomic scattering factors $f_0(q)$ for Ge, Sb and Te atoms. (b) Atomic scattering factors for 10 keV (λ=1.24 Å) X-rays as a function of scattering angle 2θ

For X-rays, the atomic scattering factor f_0 is a rapidly decaying function of the scattering vector q=sin(θ)/λ. It can be both measured and calculated, and is tabulated for most atoms in the International Tables for Crystallography. The dispersion corrections f_1 and f_2 for our atoms and X-ray energy are also well known [55, 56, 57, 58]. The values of the dispersion corrections are comparably big only for X-ray energies close to an

atomic absorption edge or for high scattering vectors, and for the current experiments are small.

The functions $f_0(q)$ are plotted in Fig.2.1(a) for Ge, Sb and Te. We see that at zero scattering angle, the atomic scattering factor is close to the atomic number Z, which is the total number of electrons in the atom.

It is worth emphasizing that antimony and tellurium are almost indistinguishable for the whole range of the scattering vector q. This point is significant here as it means that we are not sensitive to Sb-Te atom replacements. To distinguish Sb and Te, tuning the energy used for scattering to the corresponding absorption edges is required. This method is widely used in element-sensitive diffraction experiments.

2.1.2 Scattering from a group of atoms

To derive the scattering amplitude from a group of atoms one just needs to superimpose the scattered wave from all atoms at the point of observation.

The phase factor from the n^{th} atom in the group is:

$$\phi_n = (\vec{k}_s - \vec{k}_i) \cdot \vec{r}_n = 2\pi\vec{q} \cdot \vec{r}_n \tag{2.6}$$

where $\vec{k}_i$ and $\vec{k}_s$ are the impinging and scattered wave vectors, respectively, and r_n is the coordinate of an atom in the group. Therefore, the scattering amplitude from a group of atoms becomes:

$$E = E_e \sum_n f_n e^{i\phi_n} = E_e F \tag{2.7}$$

where the summation is taken over all atoms in the group. The structure factor F plays a fundamental role in the current work, since it is the only parameter in which atomic positions appear.

In crystals, groups of atoms are distributed periodically, and these groups are referred to as the basis of the crystal. The basis, in turn, is distributed on the points of a crystal lattice. The crystallographer's task is to determine both, the crystal lattice structure (symmetry) and the corresponding basis.

2.1.3 Reciprocal lattice concept

The reciprocal lattice concept arises when there is a periodicity in the atomic distribution. It is a very useful method for understanding the geometry of a diffraction experiment.

Let us consider an infinite crystal made by the superposition of an atomic basis on a three-dimensional lattice based on the three vectors $\vec{a}_1$, $\vec{a}_2$, $\vec{a}_3$. The total scattering amplitude is the sum of the scattering amplitudes of each of the unit cells. Calculating the phase shifts as shown in the previous section for the electric field amplitude gives:

$$E = E_e F \sum_m e^{i2\pi\vec{q}\cdot\vec{r}_m} \tag{2.8}$$

where r_m is the coordinate of the m^{th} unit cell and the summation is taken over all unit cells. The sum in Eq. 2.8 is maximal for the condition:

$$e^{i2\pi\vec{q}\cdot\vec{r}_m} = 1 \tag{2.9}$$

which can be rewritten as:

$$\vec{q} \cdot \vec{r}_m = N, \tag{2.10}$$

where N is any integer number.

In our crystal, the unit cells are distributed periodically, where the coordinate r_m is determined by the relation:

$$\vec{r}_m = m_1\vec{a}_1 + m_2\vec{a}_2 + m_3\vec{a}_3, \tag{2.11}$$

and m_1, m_2, m_3 are integer numbers. The solution of Eq. 2.10-2.11 with respect to the vector $\vec{q}$ is known as the reciprocal lattice:

$$\vec{q} = h\vec{b_1} + k\vec{b_2} + l\vec{b_3}, \tag{2.12}$$

where h,k,l are integer numbers, and b_1, b_2 and b_3 are determined by the relations:

$$\vec{b}_1 = \frac{\vec{a}_2 \times \vec{a}_3}{\vec{a}_1 \cdot [\vec{a}_2 \times \vec{a}_3]}, \vec{b}_2 = \frac{\vec{a}_3 \times \vec{a}_1}{\vec{a}_1 \cdot [\vec{a}_2 \times \vec{a}_3]}, \vec{b}_3 = \frac{\vec{a}_1 \times \vec{a}_2}{\vec{a}_1 \cdot [\vec{a}_2 \times \vec{a}_3]}. \tag{2.13}$$

One may check that the vector 2.12 is a solution of 2.10 by substituting it there, and taking into account that:

$$\vec{a}_i \cdot \vec{b}_j = \begin{cases} 1 & i = j, \\ 0 & i \neq j. \end{cases} \tag{2.14}$$

Eq. 2.12 is equivalent to Bragg's law, where the diffracting planes are determined by the Miller indices h,k,l.

Therefore, the reciprocal lattice sites determine the positions of the Bragg reflections (maxima of the function 2.8) for the crystal. This means that for a given crystal, the scattering vectors $\vec{q}$ are determined only by the crystal lattice. Thus, for a given orientation of a crystal, we know where to put the X-ray source and detector to observe a diffraction peak.

2.1.4 Intensity from a small crystal

We start by further developing Eq. 2.8, which for the case of a finite parallelepiped crystal of $N_1 \times N_2 \times N_3$ unit cells takes the form:

$$E = E_e F \sum_{m_3=0}^{N_3-1} \sum_{m_2=0}^{N_2-1} \sum_{m_1=0}^{N_1-1} e^{i2\pi\vec{q}\cdot(m_1\vec{a}_1 + m_2\vec{a}_2 + m_3\vec{a}_3)} \tag{2.15}$$

or, separating the summations:

$$E = E_e F \sum_{m_1=0}^{N_1-1} e^{i2\pi m_1\vec{q}\cdot\vec{a}_1} \sum_{m_2=0}^{N_2-1} e^{i2\pi m_2\vec{q}\cdot\vec{a}_2} \sum_{m_3=0}^{N_3-1} e^{i2\pi m_3\vec{q}\cdot\vec{a}_3} \tag{2.16}$$

Taking into account that the summation of geometric series is straightforward:

$$\sum_{k=0}^{n} r^k = \frac{r^{n+1} - 1}{r - 1} \tag{2.17}$$

for the electric field amplitude E we obtain:

$$E = E_e F \frac{e^{i2\pi N_1 \vec{q}\cdot\vec{a}_1} - 1}{e^{i2\pi \vec{q}\cdot\vec{a}_1} - 1} \frac{e^{i2\pi N_2 \vec{q}\cdot\vec{a}_2} - 1}{e^{i2\pi \vec{q}\cdot\vec{a}_2} - 1} \frac{e^{i2\pi N_3 \vec{q}\cdot\vec{a}_3} - 1}{e^{i2\pi \vec{q}\cdot\vec{a}_3} - 1} \tag{2.18}$$

It is known from electrodynamics that the intensity is $I = E^2 c/8\pi$, where $E^2{=}EE^*$. After performing some simple manipulations one obtains:

$$I = I_e F F^* \frac{\sin^2(\pi N_1 \vec{q}\cdot\vec{a}_1)}{\sin^2(\pi \vec{q}\cdot\vec{a}_1)} \frac{\sin^2(\pi N_2 \vec{q}\cdot\vec{a}_2)}{\sin^2(\pi \vec{q}\cdot\vec{a}_2)} \frac{\sin^2(\pi N_3 \vec{q}\cdot\vec{a}_3)}{\sin^2(\pi \vec{q}\cdot\vec{a}_3)} \tag{2.19}$$

Any scattering vector $\vec{q}$ can be represented using 2.12 if we allow h,k,l to be real numbers. Substituting 2.12 into 2.19 and taking into account 2.14 we obtain:

$$I = I_e F F^* \frac{\sin^2(\pi N_1 h)}{\sin^2(\pi h)} \frac{\sin^2(\pi N_2 k)}{\sin^2(\pi k)} \frac{\sin^2(\pi N_3 l)}{\sin^2(\pi l)} \tag{2.20}$$

This rapidly oscillating function (with increasing number of unit cells) is called the interference function. Figure 2.2 shows a plot of the function $\frac{\sin^2(\pi N_1 h)}{\sin^2(\pi h)}$ over h for the case of $N_1{=}20$ unit cells. It is worth noting that the intensity is largest at the Bragg's

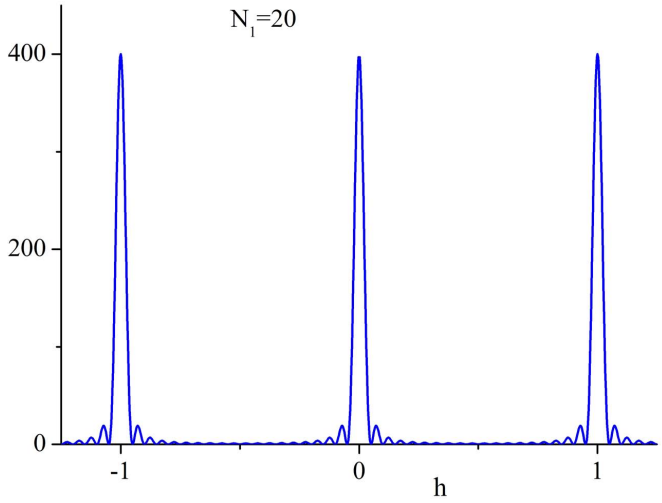

Figure 2.2: Interference function for 1d crystal with 20 periods

points $h{=}0,1,\ldots n$ and equal to N_1^2. The FWHM of the Bragg peaks is on the order of $1/N_1$. The width of the peaks is very often used in X-ray diffraction to determine the crystal grain size.

Another point is that the area of a peak is approximately N_1. This means that the triple integral of the function 2.20 over h, k and l near the Bragg reflection is proportional to $N_1 \times N_2 \times N_3$, what is the volume of the crystal. This fact gives rise to a very important concept – the integrated intensity – which we will describe in the next section.

2.1.5 Intensity integral over reciprocal space

Here we describe a fundamental concept which allows the determination of the structure factor from a diffraction experiment. The concept states that for a single crystal, with quality good enough to have distinguishable Bragg peaks in reciprocal space, the peak intensity integral over reciprocal space is proportional to the average structure factor squared. Or in mathematical form:

$$\iiint_{Bragg} I(h,k,l)\,\mathrm{d}h\,\mathrm{d}k\,\mathrm{d}l \;\propto\; I_e F F^* V \tag{2.21}$$

where V is the volume of the crystal and the integration is taken near a Bragg reflection, where there is still some contribution to the intensity. We are not aware of a general proof for this statement, since it is absent in the common literature on X-ray diffraction [51, 52, 59] and the focus is on specific cases. However the statement is widely used even in protein crystallography, where a crystal can contain many defects, strain, granularity and so forth, thus we assume we can use it for our study.

Warren [51] has shown that Eq. 2.21 is valid for a small "ideally imperfect" crystal with vibrational atomic displacements. The structure factor F can be generalized for this case as:

$$F = \sum_i f_i e^{-B_{iq}q^2} e^{i2\pi\vec{q}\cdot\vec{r}_i} \tag{2.22}$$

where the summation is taken over all atoms within the unit cell. The term $e^{-B_{iq}q^2}$ is called the Debye–Waller factor, which is related to the mean square atomic displacements by the formula:

$$B_{iq} = 8\pi^2\langle u_{iq}^2\rangle q^2 \tag{2.23}$$

and $\langle u_{iq}^2\rangle$ is the mean squared displacement of the i$^{\text{th}}$ atom in the unit cell in the direction of the vector $\vec{q}$. For the case of isotropic materials, the index q is often omitted.

2.2 Molecular beam epitaxy

Epitaxy is the phenomenon of single crystal growth with the orientation inherited from a single crystal template. Molecular beam epitaxy (MBE) is one of the methods to fabricate single crystal epitaxial films on various single crystal substrates. In this method, an ingot of a source material is heated in ultrahigh vacuum to a temperature where there is some sublimation or evaporation of the material. The released material then deposits on the single crystalline wafer, which is usually placed opposite the material sources. The presence of an ultrahigh vacuum is required to ensure both that the directed molecular beams impinge upon the surface and that the surface does not react with residual gas in the chamber on time scales comparable to the growth rate. The substrate crystal temperature is optimized such that the atoms or molecules arriving on the crystal do not desorb immediately but stay on the surface for some time and, at the same time, have enough surface mobility to find the energetically best place to stick.

When several material sources are used, the sample crystal is placed at the focus of the sources as shown on Fig. 2.3. In order to minimize the compositional variation of the flux along the sample surface, the sample is often rotated during growth.

Molecular beam epitaxy is probably the slowest method for the growth of epitaxial

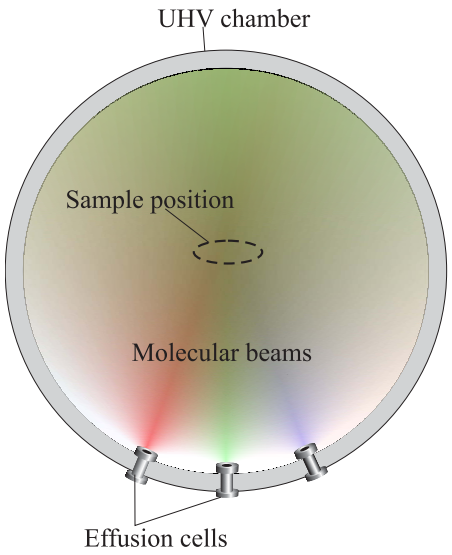

Figure 2.3: The core components of an MBE machine. The red, green and blue colors qualitatively represent the material flux density. The substrate is placed at the intersection of the axes of the three effusion cells.

films, but also the most controllable and pure. Typical growth rates in MBE range from hundreds of nanometers per minute down to a few angstroms per minute. Such a low growth rate requires ultra-high vacuum environment to maintain the clean surface necessary for epitaxial growth. Therefore the samples and source materials are placed into an ultra-high vacuum chamber which is continuously pumped. The best MBE machines have base pressures in the range of 10^{-9} to 10^{-11} mbar which corresponds to a molecular mean free path in the range of 10^2 to 10^4 kilometers! This means that the molecules which create the pressure in the chamber do not collide and can scatter only from the chamber walls. The name "molecular beam" originates from the fact that for typical MBE growth rates, the source molecular flux is very small. Therefore, the molecules or atoms in the flux do not interact until they finally reach the substrate or the chamber walls. The corresponding molecular mean free path in the flux is still on the order of kilometers. This means that the molecules or atoms "fly" almost straight in the manner of a beam, until they reach the substrate (see Fig. 2.3).

When the substrate material in the MBE is the same as the deposited material the process is called *homoepitaxy*. In the case of different substrate and deposited material the process is called *heteroepitaxy*.

Heteroepitaxy is now widely used for the fabrication of low–dimensional structures such as quantum wells, nanowires, quantum dots etc. which have potential for nano- and opto-electronics. Several advanced devices, e.g. quantum cascade lasers and laser diodes based on quantum wells have been fabricated by heteroepitaxy.

Substrate crystals for the MBE in this work are typically 1 mm thick disks. The disks are prepared by cutting and polishing bulk single crystals grown by the Czochralski process.

2.2.1 Classification of growth processes

There are three different thermodynamical growth modes in heteroepitaxy: Frank–van der Merwe, Stranski–Krastanov and Volmer–Weber growth.

Frank–van der Merwe is a layer-by-layer growth process. In this process, adsorbed atoms initially form two-dimensional islands which grow in width until they form a complete layer. Subsequent layers grow two–dimensionally, one at a time, producing a smooth flat surface as shown in Fig. 2.4(a). From the thermodynamical point of view the stability of the system is determined by the difference in chemical potential $\Delta\mu$ before and after the layer has formed. For lattice matched material B grown on material A the chemical potential difference is:

$$\Delta\mu = S_0(\gamma_B + \gamma_{AB} - \gamma_A) \tag{2.24}$$

where γ_A, γ_B and γ_{AB} are the corresponding surface and interface energies. This equation is valid for any layer thickness, if there is no contribution to the chemical potential which depends on the layer thickness. Thermodynamical stability requires a reduction of the chemical potential, thus for layer-by-layer growth the following relationship should be valid:

$$\gamma_A > \gamma_B + \gamma_{AB} \tag{2.25}$$

The surface energies γ_A and γ_B are positive numbers, while the interface energy γ_{AB} can be both, positive and negative. A positive interfacial energy would imply that the two materials phase segregate in the bulk upon mixing, since phase segregation *decreases* the interfacial area. A negative interfacial energy means that the materials intermix well. If material A grows on material B then the requirement for layer-by-layer growth is:

$$\gamma_B > \gamma_A + \gamma_{BA} \tag{2.26}$$

If relations 2.25 or 2.26 are not fulfilled, then **Volmer–Weber** growth occurs. Usually, interfacial energy γ_{AB} is much smaller than the surface energy of each material γ_A and γ_B. Therefore, if material A on material B grows layer-by-layer, then material B on material A usually grows three–dimensionally, which is Volmer–Weber growth.

Volmer–Weber growth starts with the formation of three–dimensional islands from the very beginning (see Fig. 2.4(c)). These islands grow in size until they coalesce and form a complete layer. Once a complete layer has formed, in principle, the surface could become smooth again. It is usually hard to grow a thin and smooth layer in this growth regime, since the layer does not want to wet the surface. In order to fabricate a layer with a smooth surface one need to find the optimal growth rate [24]. If the layer is grown fast enough, the surface has no time to develop strong roughness before it is buried by the subsequent layer. Once the surface is complete, the growth proceeds in layer-by-layer or step flow mode.

The **Stranski–Krastanov** growth mode is characterized by initial two-dimensional layer-by-layer growth of a wetting layer (Fig. 2.4(b)). After this thickness, the film switches to three-dimensional island growth, and roughness develops. This 2D–3D growth is similar to the Asaro–Tiller–Grinfeld instability and very common in (but not limited to) lattice mismatched films [60]. The reason of this instability is that it is energetically favorable to develop roughness to relax the accumulated strain energy at

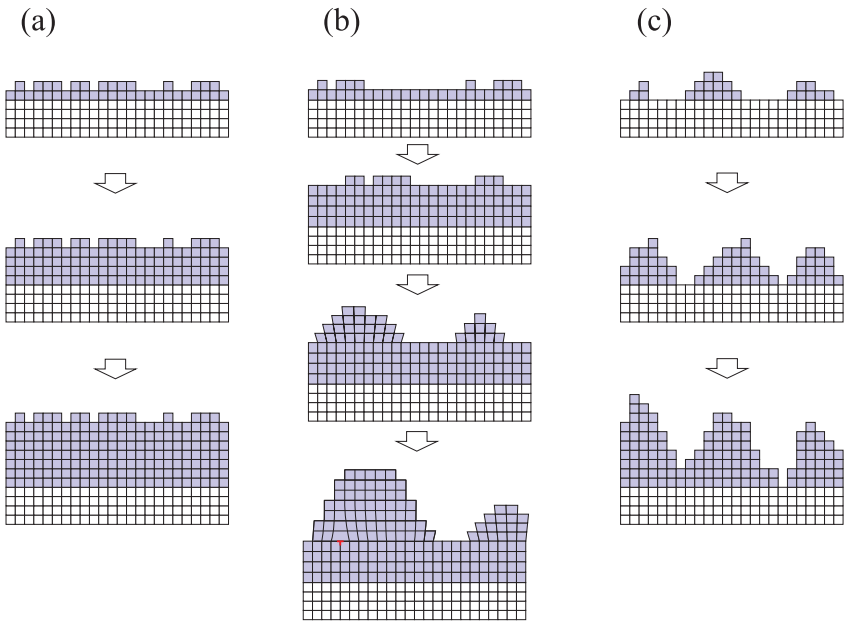

Figure 2.4: Different growth modes in heteroepitaxy: (a) Layer-by-layer or Frank-van der Merve growth. (b) Stranski-Krastanov growth mode with initial layer-by-layer growth. (c) Three dimensional Volmer-Weber growth.

the top of islands. This process is widely used for the growth of strained pseudomorphic quantum dots [61]. As the growth proceeds further, the film starts to fully relax the accumulated strain by introducing misfit dislocations, as marked in Fig. 2.4(b). Interestingly enough, Stranski-Krastanov growth was first observed in an unstrained heterosystem [62], with the same accumulation of energy with layer thickness. In this case, instead of strain energy, it was the electrostatic energy of a capacitor due to the presence of surface and interface charge that initiated Stranski-Krastanov growth.

2.2.2 Diffractometer and MBE chamber

Figure 2.5 schematically shows the combination of a molecular beam epitaxy (MBE) chamber with a six circle diffractometer used in this work [63]. The details of the diffractometer geometry will be discussed in chapter 3 describing the advanced data acquisition techniques used.

The diffractometer section is shaded in red in Fig. 2.5, the unshaded remainder represents the interchangeable MBE chamber. The MBE chamber can also be operated separately.

The sample is mounted on one of the diffractometer circles and separated from the atmosphere by the chamber. A differentially pumped rotation feedthrough is used to interface the diffractometer rotating parts with the MBE chamber.

The MBE system consists of four chambers: the load lock, preparation, transfer and growth chambers. Each chamber can be isolated from the others by in-vacuum valves. The samples are first loaded into the load lock chamber which is equipped with a sample heater to perform initial degassing. Next, the samples are transferred to the preparation

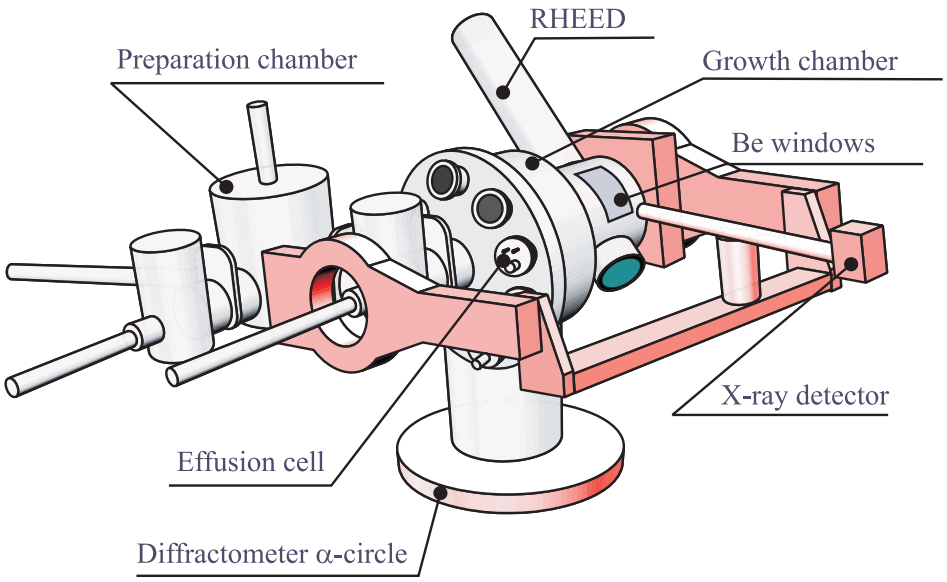

Figure 2.5: Schematic illustration of our combined MBE machine and six circle diffractometer. The parts shaded in red belong to the diffractometer and the remainder corresponds to an interchangeable MBE system

chamber using transfer rods. In the preparation chamber, the samples are heated to higher temperatures to desorb possible contamination. After this procedure, the samples are introduced into the growth chamber.

Because of the horizontal polarization of the synchrotron radiation, the requirement of constant angle of the effusion sources and the need of high diffractometer resolution (long detector arm), the sample is mounted vertically in the growth chamber. The effusion cells are mounted horizontally on the side of the growth chamber. The chamber allows for up to seven sources to be installed. The sample chamber is equipped with a 5–50 keV electron gun and a fluorescence screen to allow grazing incidence electron diffraction measurements. The beryllium windows of the sample chamber allow the X-rays to be transmitted through the chamber.

The growth chamber is pumped by two ion pumps down to a base pressure around 3×10^{-10} mbar. The other chambers are also pumped independently by ion pump, turbomolecular pumps and scroll pumps down do the same pressures. The pressures in the system are measured using Bayard–Alpert ionization pressure gauges. A quadrupole mass spectrometer is also attached to the growth chamber to allow for measurement of contaminants in the mass range 0...100 atomic mass units.

The chamber is equipped with liquid nitrogen cooling shrouds. This system requires a constant flow of nitrogen through it to support the ultra-high vacuum environment during operation of the effusion sources.

The remaining components are standard MBE and UHV components. Their description can be found elsewhere.

2.2.3 Beamline

The Pharao beamline is attached to the BESSY II (Helmholtz Center for Materials and Energy, Berlin) storage ring. The main components of the beamline are schematically shown in Fig. 2.6. A detailed beamline description can be found in the literature [63].

Intense X-rays are generated as the 1.7 GeV ultra–relativistic electrons of the storage ring pass through the periodic magnetic field of a wiggler. The wiggler radiation is polarized in the horizontal plane, has a white spectrum and a typical divergence of $\Delta\phi \approx 2/\gamma \approx 0.07\,^{\circ}$.

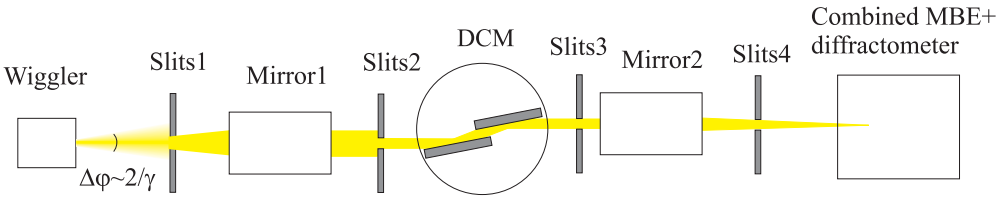

Figure 2.6: Schematic illustration of the PHARAO beamline.

The first slits are used to define a rectangular beam shape. The first collimating mirror focuses the diverging beam into a parallel beam. The second slits are used to suppress stray radiation.

The double crystal monochromator (DCM) contains two nearly perfect Si crystals in a non-dispersive arrangement with parallel (111) surfaces. The first crystal is maintained in the Bragg condition with respect to the incidence beam for a certain energy. Since the impinging beam is parallel, the crystal produces a monochromatic beam which is then diffracted again by the second Bragg crystal. Higher harmonics has negligible intensity in the wiggler energy spectra. A third set of slits act to suppress stray radiation from the previous optical components. The energy spread after the monochromator is $\Delta E \approx 10\,eV$.

The second focusing mirror focuses the beam to $0.5 \times 0.5\,\mathrm{mm}^2$ at the sample. The final divergence of the beam $\Delta\phi$ at the sample is around 10 arcsec. The fourth set of slits serves to further reduce any stray radiation. The total beam flux at the sample is around 10^{10}–10^{11} photons/sec.

2.3 Geometry corrections

In this section we derive the correction factors required to extract the structure factors of a crystal in a real physical experiment. These corrections are always geometry dependent and require a thorough understanding of the diffraction experiment. The correction factors are a very well known component of any X-ray structure analysis experiment, and have been extensively studied [64, 65, 66, 67, 68, 69, 70, 54]. There is no general algorithm, however, able to account for all the necessary corrections in an arbitrary experiment. Each of the known correction factors are valid only for a specific experimental condition (peak width, sample quality, geometry, structure dimension). For example, for the study of so-called crystal truncation rods, the correction factors derived by Vlieg [54] are very useful. In this study, however, we are interested in the integrated intensities of bulk reflections with strong peak broadening due to a high degree

of film imperfection. Thus, the usage of well-developed relations for the correction factors is not possible. Furthermore, due to instrumental limitations, the traditional way of integrating a peak by opening the detector slits larger than the diffracted beam size and then performing ω scans is not possible. We have therefore designed an alternative experimental algorithm. This new algorithm requires new geometric corrections to be developed.

We will show that for our case of very broad peaks, we may use h,k,l scans with appropriate detector slits settings and correction factors, instead of traditional ω scans.

2.3.1 Origin of the corrections

To obtain the structure factor F from an experiment, we have to measure the intensity integral (2.21), which is proportional to FF^*. An appropriate experimental method is needed to obtain this intensity integral. We start by considering a small sample with sharp Bragg reflections.

We assume the sample is so small that there is negligible extinction, absorption and the sample is fully inside the X-ray beam as shown in Fig. 2.7. It is also assumed that the sample is regular enough to have sharp Bragg reflections, so that the detector slits capture all of the intensity. The experimental geometry for this case is shown in Fig. 2.7 in two projections.

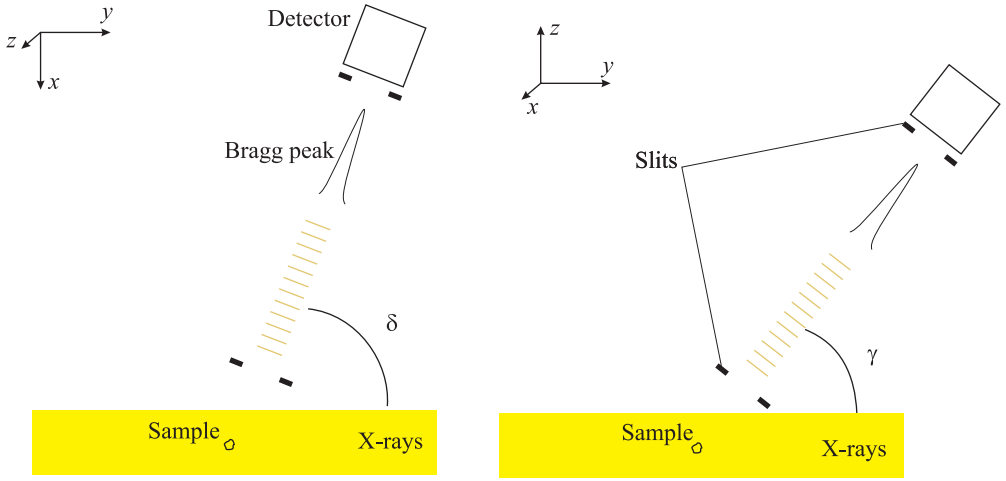

Figure 2.7: Ideal X-ray experiment for the use of kinematical scattering theory . The sample is so small that it is completely in the beam, has no absorption and extinction and the Bragg peaks are sharp enough.

Modern diffractometers with complicated geometries do not support continuous data acquisition, but, instead, perform the measurements in steps. At each (h,k,l) point the detector integrates the impinging photon flux over time and slit area. For a given (h,k,l) vector, the diffractometer software calculates the necessary angles and drives the diffractometer motors to the corresponding positions. The geometry shown in Fig. 2.7 in two projections is realized in our case by a six circle diffractometer operating in z-axis mode. The details of the six circle diffractometer geometry are discussed in chapter 3. In the z-axis geometry [71], the operating angles are the detector angles δ, γ and the

sample rotation angle ω.

Therefore, for the case shown in Fig. 2.7, the detector counter $D(h,k,l)$ will show the value:

$$D(h,k,l) = \Delta t \iint_S I(h,k,l)\,\mathrm{d}S \tag{2.27}$$

where Δt is the detector integration time, S is the area of the detector slits and $I(h,k,l)$ is the X-ray intensity diffracted from our whole sample. Here we omit the complications due to the fact that the radiation is quantized and thus the measurement is the statistical process. As we have said, the $I(h,k,l)$ is an implicit function of ω, δ and γ. The double integral could be replaced by an iterative integral over diffractometer angles:

$$D(h,k,l) = R^2 \Delta t \int_{\gamma_1}^{\gamma_2}\int_{\delta_1}^{\delta_2} I(h,k,l)\,\mathrm{d}\delta\,\mathrm{d}\gamma \tag{2.28}$$

where R is the distance from the sample to the detector slits, and δ and γ are the corresponding diffractometer angles. Our detector slits make rectangular openings aligned with the corresponding detector angles $\Delta\delta$ and $\Delta\gamma$.

The intensity integral concept introduced earlier states that the integral over reciprocal space coordinates is proportional to the structure factor squared (see Eq. 2.21). The disadvantage of this formula is that it is expressed in terms of reciprocal coordinates. We can rearrange the integral to have more natural coordinates by introducing the Jacobian matrix:

$$\iiint_{Bragg} I(h,k,l)\,\mathrm{d}h\,\mathrm{d}k\,\mathrm{d}l \;=\; \iiint_{Bragg} I(h,k,l)\,\frac{\partial(\mathrm{h},\mathrm{k},\mathrm{l})}{\partial(\omega,\delta,\gamma)}\mathrm{d}\omega\,\mathrm{d}\delta\,\mathrm{d}\gamma \tag{2.29}$$

For more details on transformation of variables in triple integrals, see for example [72].

For a sharp Bragg reflection, the integration volume is small. Therefore, it can be assumed that the Jacobian matrix is constant valued over the integration volume and can be moved outside the integral, using the value at the Bragg reflection:

$$\iiint_{Bragg} I(h,k,l)\,\mathrm{d}h\,\mathrm{d}k\,\mathrm{d}l \;=\; \frac{\partial(\mathrm{h},\mathrm{k},\mathrm{l})}{\partial(\omega,\delta,\gamma)}\;\iiint_{Bragg} I(h,k,l)\,\mathrm{d}\omega\,\mathrm{d}\delta\,\mathrm{d}\gamma \tag{2.30}$$

The volume of integration on the left- and the right-hand side of Eq. (2.30) are identical.

We would like to reduce this triple integral on the right side of Eq. (2.30) to iterative integrals over diffractometer angles. To make this possible, we choose an integration volume limited by the corresponding coordinate surfaces of the curvilinear coordinates ω, δ and γ, as shown in Fig. 2.8. The trick is that this arbitrary choice of integration volume does not change the result of the integration, since the main contribution to the intensity function is in the center of the volume. What we gain here, is that we can reduce the triple integral in 2.30 to iterative integrals over diffractometer angles. These iterative integrals have physical meaning and correspond to diffractometer scans, which should be done iteratively in the order the integrals are written.

Considering all the points mentioned above, and replacing the Jacobian matrix by its

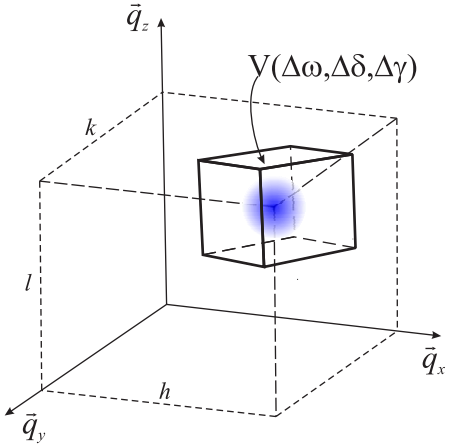

Figure 2.8: Schematic illustration of the integration volume in the vicinity of a Bragg reflection, if (ω, δ, γ) coordinates are varied.

value at the Bragg point, we can write:

$$\iiint_{Bragg} I(h,k,l)\,\mathrm{d}h\,\mathrm{d}k\,\mathrm{d}l \;= L \int \mathrm{d}\omega \int_{\gamma_1}^{\gamma_2}\int_{\delta_1}^{\delta_2} I(h,k,l)\;\mathrm{d}\delta\,\mathrm{d}\gamma \tag{2.31}$$

where L is the value of Jacobian matrix at the (h,k,l) point.

The Jacobian matrix is a geometry dependent function and actually represents a very general form of the Lorentz factor [51]. For the geometry of our six-circle diffractometer it is derived in [54].

Substituting Eq. (2.28) in (2.31), we obtain the relation:

$$\iiint_{Bragg} I(h,k,l)\,\mathrm{d}h\,\mathrm{d}k\,\mathrm{d}l \;=\; L \int_{Bragg} \frac{D(h,k,l)}{R^2\Delta t}\,\mathrm{d}\omega \tag{2.32}$$

The left part of this equation is nothing other than the general form of the intensity integral (2.21), which is proportional to the structure factor squared. Therefore, substituting the right part of the relation (2.21) in Eq. (2.32) we obtain a relation for the structure factor:

$$I_e F F^* V \;\propto\; L \int_{Bragg} \frac{D(h,k,l)}{R^2\Delta t}\,\mathrm{d}\omega \tag{2.33}$$

Since I_e is proportional to $I_0 P/R^2$ (see Eq. (2.7)), this is the same as:

$$I_0\Delta t\frac{P}{L} F F^* V \;\propto\; \int_{Bragg} D(h,k,l)\,\mathrm{d}\omega \tag{2.34}$$

The photon flux I_0 decays significantly in storage rings due to the limited lifetime of the accelerated electrons. The impinging flux I_0 is monitored by an additional detector. Therefore, the integration time Δt is adjusted during the experiment, so that $I_0\Delta t = const$ (constant monitor counts) or the detector counts are normalized to the incident

beam (constant measurement time). Thus, finally we can write:

$$\frac{P}{L}FF^*V \propto \int_{Bragg} D(h,k,l)\,\mathrm{d}\omega \tag{2.35}$$

The integral on the right side of Eq. (2.35) is obtained experimentally from standard ω scans at the Bragg reflections. The term P/L is the general case of the Lorentz–polarization factor [51]. This factor is geometry dependent and represents one of the corrections which should be applied in standard ω scans in order to obtain the structure factor F.

2.3.2 (h,k,l) scans for structure factor determination

Normally we would use the equations derived in the previous paragraph. However, our detector acceptance slit size is limited, and is too small to integrate over the entire Bragg peak. In this case, the integration over δ and γ is not performed automatically by the detector active area, and another method should be developed. Doing iterative δ, γ and ω scans using a point detector is too time consuming.

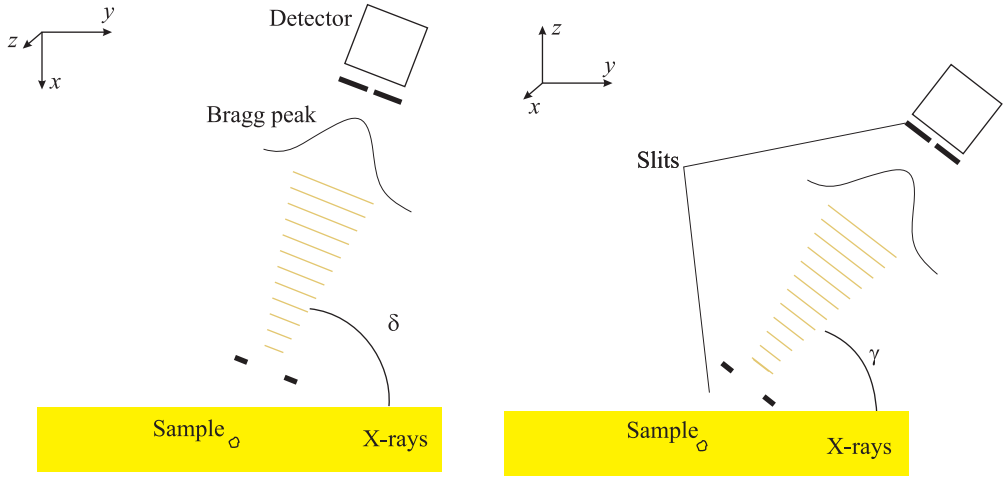

Figure 2.9: The geometry of the experiment for the case of a small sample in the beam, which has no absorption and extinction, but for which the Bragg peaks are very broad

In our case we go to the opposite limit, and close the detector slits so much that we only see the intensity at a "single" point of observation. Thus for the detector counts D we can write:

$$D(h,k,l) = \mathrm{I}(h,k,l)S\Delta t \tag{2.36}$$

where S is the detector slit area and Δt is integration time. Integrating this equation over (h,k,l) near a Bragg peak we obtain:

$$\iiint_{Bragg} \mathrm{D}(h,k,l)\,\mathrm{d}h\,\mathrm{d}k\,\mathrm{d}l \propto S\Delta t \iiint_{Bragg} I(h,k,l)\,\mathrm{d}h\,\mathrm{d}k\,\mathrm{d}l \tag{2.37}$$

At a synchrotron, the incident beam intensity I_0 decays over time, therefore the inte-

gration time Δt is automatically normalized to the incident flux I_0 (constant monitor counts) or the detector counts are normalized to the incident beam intensity (constant measurement time). Taking this into account and substituting Eq. (2.21) in (2.37) we obtain an equation for the structure factor F:

$$\iiint_{Bragg} \mathrm{D}(h,k,l)\,\mathrm{d}h\,\mathrm{d}k\,\mathrm{d}l \;\propto\; \frac{P}{R^2} F F^* V \tag{2.38}$$

where V is the volume of our small crystal.

The detector counts integral (2.38) can be obtained experimentally. For the case of a good Gaussian peak shape in reciprocal space, the volume integral is proportional to the product of the three peak widths and the count rate at the Bragg peak. We can therefore write

$$w_h w_k w_l \mathrm{D}_0 \;\propto\; \frac{P}{R^2} F F^* V, \tag{2.39}$$

where w_h, w_k and w_l are the width of the Gaussian peaks from h,k and l scans, respectively. Analogously, we could use (ω, δ, γ) scans in this case, after introducing the Lorentz correction factor.

It is important to emphasize that the major difference between broad and sharp Bragg reflections is the additional correction $1/R^2$ appearing in Eq. (2.39). The reason is that for sharp reflections, the distance to the detector does not play a role, since the slits are always wider than the peak, while for broad reflections the detector slits acceptance angle decreases as the distance to the detector increase. It acts as one would close the detector slits. This correction is called the "linear gamma table" - a geometric correction for diffractometers where the distance to the detector changes. This correction is only used when the peak width is larger than the detector slit acceptance.

2.3.3 Area correction

Finally, the last step is to consider actual experimental conditions, namely that the sample size is significantly larger than the beam cross section. We will consider here the case of a thin sample with the surface parallel to the beam (0.7 degrees off) as schematically shown in Fig. 2.10 in two projections. We assume a thin film on the sample which is "imperfect" enough for the use of kinematical theory and thin enough to neglect extinction and absorption.

The slits near the sample are necessary to cut down on undesired radiation scattered from the chamber walls, beam-shaping slits and so forth. One option is to leave the slits open as large as possible. Unfortunately, in this case, additional peak broadening effects appear due to the large spatial size of the sample which are difficult to account for. Furthermore, different sample regions will have different Bragg conditions, since the angular sample size is comparable to the peak widths. To avoid this complexity, it is necessary to reduce the slit widths to simulate a small sample size. One could think that this were the solution, we just need to calculate the parallel projection of the slits on the sample surface and intersect this with the beam fingerprint. However, this is true only for the case where the front slits are very close to the sample, and the detector slits are very far away. Otherwise we have to take into account that, in addition to the parallel projected region, there are contributions from a smooth half shadowed region as shown in Fig. (2.11) as case 2. The contributions to the detector counts for the cases

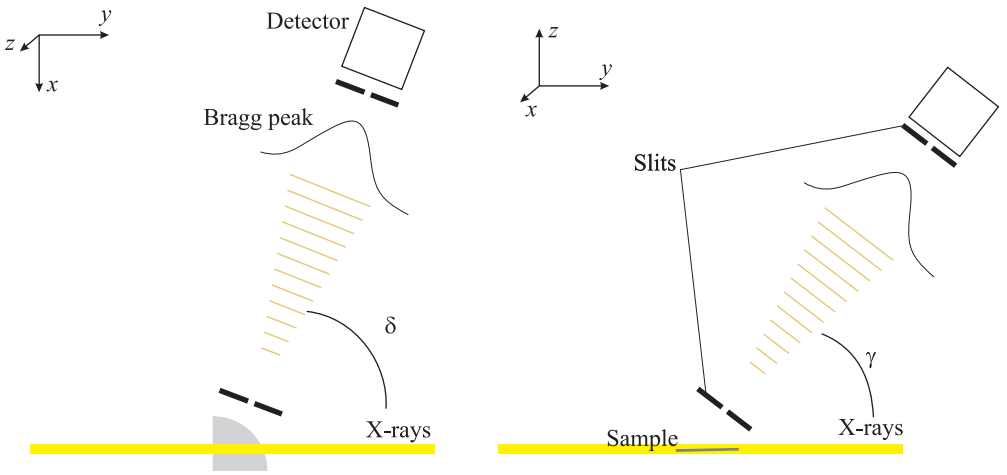

Figure 2.10: The real experimental case. The sample is larger then the beam. The X-rays are at grazing incidence. The Bragg peaks are much broader than the detector slits.

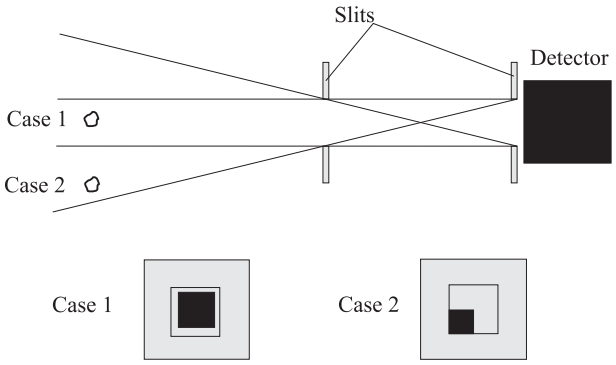

Figure 2.11: Two cases contributing to the detector counts with different weights for a situation where the peaks widths are broader than the angular resolution of the slits.

1 and 2 are obviously different. For the second case, a significant part of the detector area is hidden behind the front slits.

However, if the front slits are very close to the sample, this half-shadow area decreases. The half-shadow area also decreases if the front slits are significantly wider than the slits at the detector. Therefore, we conclude that we have the following requirements for the slits settings:

- The front slits should be as close to the sample as possible.
- The slits at the detector preferably should be smaller than the front slits at the sample, ideally a single point.
- The front slits should still be small enough so that the angular resolution due to the slits remains much higher than the angular width of the Bragg reflections.

We used $4\times4\,\mathrm{mm}^2$ slits at the front of our evacuated flight tube. The area correction is a coefficient proportional to the intersection of the X-ray beam fingerprint with the part of the sample visible by the detector. An example of the sample surface visible by the detector is shown in Fig. 2.12. We use $4\times4\,\mathrm{mm}^2$ slits in the calculations. The figure shows calculations for the (1,5,3) Bragg reflection. The incident X-ray intensity

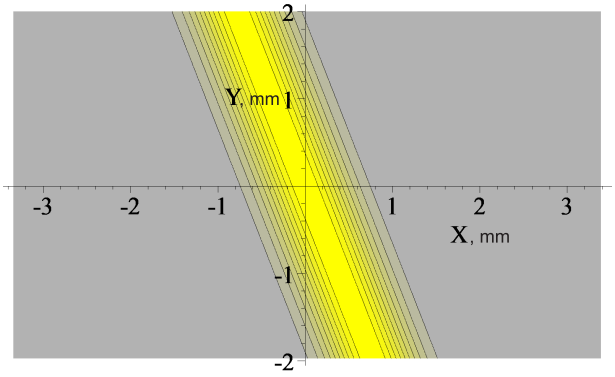

Figure 2.12: The grey rectangular region shows an example of a sample region visible to the detector. The angles are set for the (1,5,3)-reflection. The yellow region is the X-ray beam fingerprint. The coordinate system is rotated.

distribution on the sample surface is also simulated. The beam shape is fitted by double Gaussian functions after recording the direct beam on a fluorescent screen.

2.3.4 Linear gamma table and polarization corrections

The linear gamma table correction $1/R^2$ is unique to the specific construction of our diffractometer. The diffractometer's γ-angle movement is composed of a translational and a rotational component, as shown in Fig. (2.13). The translation of the detector is proportional to $\cot\gamma$, and becomes significant for large out-of-plane scattering vectors. The distance to the detector, therefore, changes significantly for different Bragg reflections. It is worth to emphasize again that this correction is applied only for reflections which are much broader than the detector acceptance angle.

For a linearly polarized wave, the polarization factor takes the form (2.3). The polarization vector is parallel to the z axis of our diffractometer. Therefore, the polarization factor is $P = \cos^2\gamma$.

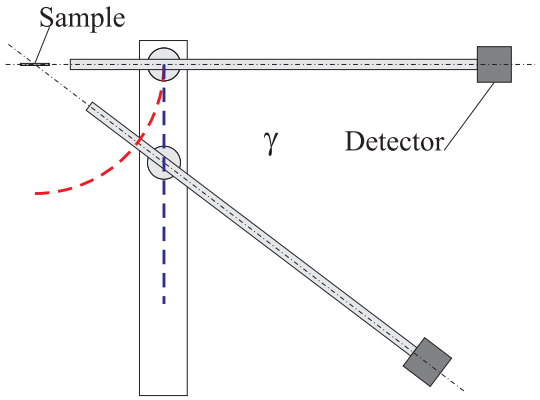

Figure 2.13: View from above onto the detector evacuated flight tube in two positions. The red dashed line shows the ideal movement, while the blue dashed line shows the actual detector movement

3 Data acquisition during diffractometer movement

This chapter has the strong methodological emphasis and is not related to the growth of phase change materials. However, the advanced data acquisition technique is the author's original work, which results were implemented and used at the beamline. Since these developments were significant part of the author's work, they are included in the manuscript. This chapter also describes the details of the six circle diffractometer and the way the modern diffractometers are automated.

3.1 Motivation

Modern diffractometers are controlled via computer programs that automatically carry out the coordinated movement of several diffractometer degrees of freedom [71]. This allows the straightforward navigation from reflection to reflection, as well as the acquisition of linear, planar and volumetric data samples using reciprocal space coordinates. Software control therefore has become a standard feature of a diffractometer, and the individual motor movements along the mechanical degrees of freedom of the diffractometer can be conveniently hidden from the operator. Stepper motors or servo motors allow the linear movement from one position to another with constant speed and feedback of their absolute position. In the most commonly used measurement mode, data acquisition (photon counting) is performed at regularly spaced positions, when no motor is moving. The result of a scan is either a 1D, 2D or 3D histogram with the bins containing the photon count rate. Counting is inhibited while the diffractometer moves to the next measurement point, until all the motors stop again, to avoid uncertainties in the location where data are acquired.

Motor movement can constitute a significant part of the total measurement time in stepped scans. A reciprocal space map is a typical example for such a measurement. An HK-plane map scan with 120×120 points, a scan area of about 2 in H and K with 4 s integration time per point takes 22 hours. With about 1.2 to 1.3 s of motor movement time per data point, about 5–6 hours of this time is not used for counting. At higher signal levels, the motor movement time may even dominate the total measurement time.

It therefore makes sense to use the motor movement time for counting. In the simplest case, the only change to the data acquisition procedure is to leave the detector open during the motor movements. During such a scan, the motor positions are not synchronized, leading to positioning errors. The motors may move simultaneously at different speeds, or, the case which produces the largest possible error, one by one in sequential order. If the deviation in reciprocal space is smaller than the step length, the data point acquired during movements is "good" and goes to the nearest bin.

In this chapter, we determine the positioning error in terms of the deviation from the ideal trajectory for uncoordinated motor movements. We then develop an algorithm to

coordinate the motor speeds for continuous scans with three motors. Such an algorithm may be included into the diffractometer software to allow stepped measurements with counting during the motor movement, either in stepped or continuous mode.

3.2 Synchronization of motor movements

3.2.1 Geometry of a diffraction experiment

Let us align the y axis of our laboratory coordinate system with the incident X-ray beam, the x axis perpendicular to y, and z perpendicular to x and y so that we obtain a left-handed coordinate system. We define our detector position by the angles δ and γ as shown in Fig. 3.1. For a given wavelength, this determines the scattering vector $\delta\vec{K} = \delta\vec{K}(\delta, \gamma)$, where $\vec{K}_i$ is the incident and $\vec{K}_s$ is the scattered vector in reciprocal space. A chosen pair of detector angles δ and γ (Fig. 3.1) defines the sampling point on the Ewald sphere in reciprocal space. By rotating the crystal, we orient the reciprocal lattice with respect to the incident vector $\vec{K}_i$ or, equivalently, orient the incident vector $\vec{K}_i$ with respect to the reciprocal lattice. We denote the sample rotation angle as ω. Therefore, navigation in the three dimensions of reciprocal space can be achieved using only three independent angles in real space, two for detector positioning on the Ewald sphere and one for sample rotation.

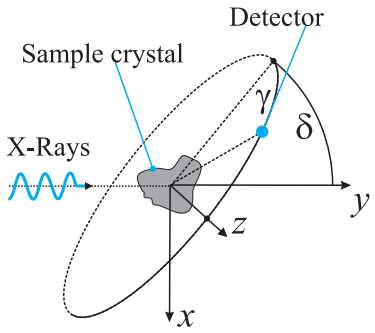

Figure 3.1: Laboratory coordinate system and detector angles δ and γ.

3.2.2 Synchronization algorithm

By motor synchronization here we mean the setting of speeds for all the motors such that the sampling position in reciprocal space moves along a specified direction. In general, and in practice for different types of diffractometers, both the sample and the detector can have numerous and different degrees of freedom. Three degrees of freedom, however, are sufficient for any diffraction experiment. Considering the case of a fixed primary beam, three linearly independent degrees of freedom define a measurement position in reciprocal space since reciprocal space, just as real space, has three dimensions. The other degrees of freedom of the diffractometer are used to align the sample or to provide a geometry in which the measurement can be performed with the least possible number of motors. The Euler rotation theorem states that any sequence of rotations in which one point of the object (in our case the one in the center of the diffractometer) remains

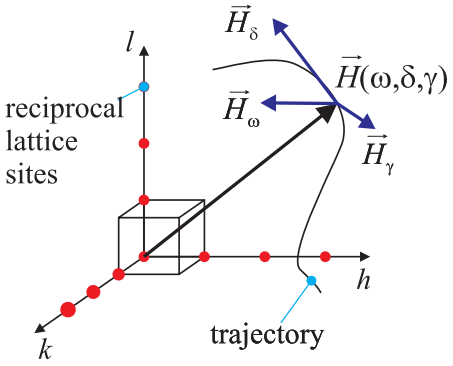

Figure 3.2: Arbitrary trajectory, the reciprocal lattice, the sampling coordinate vector $\vec{H}(\omega, \delta, \gamma)$ and the local basis $\vec{H}_\gamma$, $\vec{H}_\delta$ and $\vec{H}_\omega$.

fixed can be replaced by one single rotation around a fixed axis. To obtain the necessary unique correspondence between the three degrees of freedom each in real and reciprocal space, we can reduce either the sample or detector rotations to a single angle, with two additional angles for the other. In practice, this is performed, independent of the diffractometer geometry, by freezing all but three angles for a measurement. For the sake of a compact and transparent discussion, we therefore limit the discussion here to three angles, one sample and two detector angles. This corresponds to the choice of a certain diffractometer type, a surface diffractometer in our case. The treatment for any other type would be analogous and is not expected to yield fundamentally different results.

The angles δ and γ denote the azimuthal and polar detector angles, respectively, and ω specifies the sample rotation, which, as discussed above, can be around an arbitrary axis.

To obtain single-valued functions, we restrict δ, γ and ω to the ranges $\omega \in [0, 2\pi], \delta \in [0, \pi], \gamma \in [0, \pi/2]$ (see Fig. 3.1). These intervals, together with the x-ray wavelength, determine the accessible volume of reciprocal space. In reality, the ranges are usually smaller and depend on the physical construction of the diffractometer.

A reciprocal lattice vector $\vec{H} = h\vec{b}_1 + k\vec{b}_2 + l\vec{b}_3$ becomes a function of the three angles $\vec{H} = \vec{H}(\omega, \delta, \gamma)$ or a function of the three motor positions. This function incorporates the lattice parameters of the crystal. Similarly, the three angles ω, δ, γ can be expressed as functions of the reciprocal space coordinates (h, k, l) within the accessible volume. To move from one point to another in reciprocal space, the three vectors

$$\vec{H}_\omega = \frac{\partial \vec{H}}{\partial \omega}, \quad \vec{H}_\delta = \frac{\partial \vec{H}}{\partial \delta}, \quad \vec{H}_\gamma = \frac{\partial \vec{H}}{\partial \gamma}, \tag{3.1}$$

determine a local basis in reciprocal space in terms of γ, δ and ω (see Fig. 3.2). Each vector of this triple determines the current direction of the sampling point movement in reciprocal space when moving the corresponding motor. The three vectors therefore can be expressed as a function of the reciprocal vector coordinates (h, k, l):

$$\vec{H}_\omega = \vec{H}_\omega(h, k, l), \quad \vec{H}_\delta = \vec{H}_\delta(h, k, l), \quad \vec{H}_\gamma = \vec{H}_\gamma(h, k, l). \tag{3.2}$$

The angular positions are functions of the corresponding motor positions, which in turn are functions of time. The full differentials of the reciprocal vector coordinates (h,k,l) therefore become:

$$\begin{aligned} dh &= (\frac{\partial h}{\partial \omega}\omega_t + \frac{\partial h}{\partial \delta}\delta_t + \frac{\partial h}{\partial \gamma}\gamma_t)dt = (h_\omega\omega_t + h_\delta\delta_t + h_\gamma\gamma_t)dt \\ dk &= (\frac{\partial k}{\partial \omega}\omega_t + \frac{\partial k}{\partial \delta}\delta_t + \frac{\partial k}{\partial \gamma}\gamma_t)dt = (k_\omega\omega_t + k_\delta\delta_t + k_\gamma\gamma_t)dt \\ dl &= (\frac{\partial l}{\partial \omega}\omega_t + \frac{\partial l}{\partial \delta}\delta_t + \frac{\partial l}{\partial \gamma}\gamma_t)dt = (l_\omega\omega_t + l_\delta\delta_t + l_\gamma\gamma_t)dt, \end{aligned}$$

or, in matrix form,

$$d\vec{H} = \begin{bmatrix} h_\omega & h_\delta & h_\gamma \\ k_\omega & k_\delta & k_\gamma \\ l_\omega & l_\delta & l_\gamma \end{bmatrix} \begin{bmatrix} \omega_t \\ \delta_t \\ \gamma_t \end{bmatrix} dt. \tag{3.3}$$

The full differential $d\vec{H}$ of the reciprocal vector is now defined within the whole accessible volume of reciprocal space. It determines the direction and speed of the sampling point movement for a given set of motor speeds.

For sufficiently small steps $\Delta\vec{H} = \vec{H}_2 - \vec{H}_1$, we can approximate the integral to obtain

$$\begin{bmatrix} \omega_t \\ \delta_t \\ \gamma_t \end{bmatrix} \Delta T = \begin{bmatrix} h_\omega & h_\delta & h_\gamma \\ k_\omega & k_\delta & k_\gamma \\ l_\omega & l_\delta & l_\gamma \end{bmatrix}^{-1} \Delta\vec{H} \tag{3.4}$$

where ΔT is the motor motion time. This motion is a straight line connecting the measurement points with the right hand side of (3.4) representing the rotation angles for the motors to reach the endpoint.

In general, we are free to use any real number in (3.4) for the step motion time ΔT. For the case of a stepped measurement with additional data acquisition during the movements it is advantageous to minimize the movement time. The shortest possible motion time ΔT is then limited by the maximum speed of the slowest motor.

$$\begin{bmatrix} \omega_{t,max} \\ \delta_{t,max} \\ \gamma_{t,max} \end{bmatrix} \cdot \begin{bmatrix} \Delta T_1 \\ \Delta T_2 \\ \Delta T_3 \end{bmatrix} = \begin{bmatrix} h_\omega & h_\delta & h_\gamma \\ k_\omega & k_\delta & k_\gamma \\ l_\omega & l_\delta & l_\gamma \end{bmatrix}^{-1} \Delta\vec{H} \tag{3.5}$$

The slowest motor is the one which has longest movement time $max(\Delta T_1, \Delta T_2, \Delta T_3)$ for a given step ΔH.

The right hand sides of (3.4) and (3.5) are equal and for a given step $\delta\vec{H}$ represent the corresponding angular vector $(\Delta\omega, \Delta\delta, \Delta\gamma)$. Thus we can write for the left hand sides

$$\begin{bmatrix} \omega_t \\ \delta_t \\ \gamma_t \end{bmatrix} \Delta T = \begin{bmatrix} \omega_{t,max} \\ \delta_{t,max} \\ \gamma_{t,max} \end{bmatrix} \cdot \begin{bmatrix} \Delta T_1 \\ \Delta T_2 \\ \Delta T_3 \end{bmatrix} \tag{3.6}$$

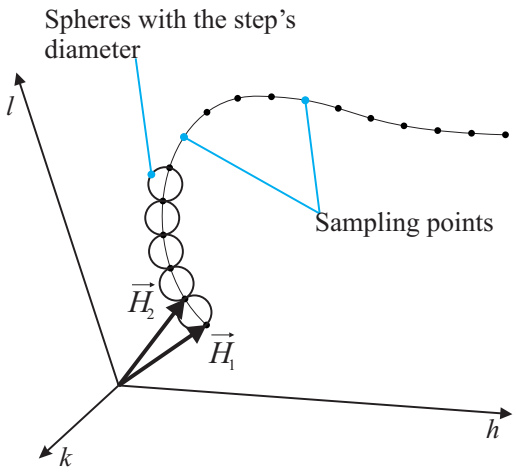

Figure 3.3: An arbitrary scan in reciprocal space connecting the measured points $\vec{H}_1..\vec{H}_n$ and the deviation spheres with diameters equal to each step.

and, finally, the motor speed vector

$$\begin{bmatrix} \omega_t \\ \delta_t \\ \gamma_t \end{bmatrix} = 1/\Delta T \begin{bmatrix} \omega_{t,max} \\ \delta_{t,max} \\ \gamma_{t,max} \end{bmatrix} \cdot \begin{bmatrix} \Delta T_1 \\ \Delta T_2 \\ \Delta T_3 \end{bmatrix} \tag{3.7}$$

where the motor motion time ΔT is the maximum of $(\Delta T_1, \Delta T_2, \Delta T_3)$. One of the motors always moves at maximum speed, as expected.

The acceleration and deceleration times should be equal for all motors in order to keep the instantaneous velocities of the motors synchronized.

The calculations presented in this chapter need to be performed by the diffractometer control software to perform a quasi-continuous scan for arbitrary scan directions using several motors. In many cases, however, the motors can be moved independently between measurement points without introducing a significant error. This version of a continuous acquisition during stepping scan is easier to implement.

3.3 Positioning errors in a stepped scan

3.3.1 Error determination for arbitrary scans

Let us now consider a stepped scan along a curved line in reciprocal space as shown in Fig. 3.3. The diffractometer measures at the discrete points $\vec{H}_1...\vec{H}_n$. We shall now calculate what error is introduced if data acquisition occurs during the non-synchronized motor movements in between the measurement points. As a deviation criterion, we construct the smallest sphere containing the endpoints of $\vec{H}_n$ and $\vec{H}_{n+1}$. The diameter of this sphere is equal to the corresponding step length, and its center is located at the midpoint of step n. As in the previous section, we construct a local basis (3.1) at each measurement point.

Let us consider the movement from H_1 to H_2 as shown in Fig. 3.4. Even for completely uncorrelated motor movements, the sampled point will never go outside the prism con-

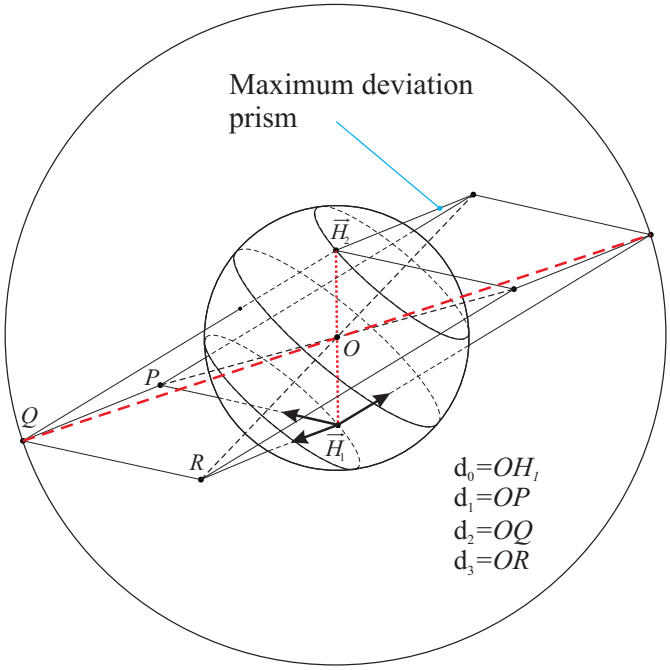

Figure 3.4: The case of a non-orthogonal basis at the origin of the step $\vec{H}_2 - \vec{H}_1$. The sphere having the longest prism body diagonal as its diameter defines the maximum error.

structed using the local basis and having the current step as a body diagonal. The trajectory of the sampled point during asynchronous motor motions always stays within the volume of this prism, since by moving the motors one by one, we move along its edges. We now define the ratio between the longest prism diagonal and the step length as the deviation. For right angles between the three vectors, all corners of the prism lie on the sphere that has the prism body diagonals as its diameter, and the deviation is equal to one. In practice, it is easier to work with the origin at the midpoint of the step. According to our definitions, the midpoint of each diagonal can be derived using equations (3.3 -3.5) as follows (see Fig. 3.4):

$$
\begin{aligned}
d_0 &= \frac{1}{2}|\vec{H}_\omega\Delta\omega + \vec{H}_\delta\Delta\delta + \vec{H}_\gamma\Delta\gamma| \\
d_1 &= \frac{1}{2}|-\vec{H}_\omega\Delta\omega + \vec{H}_\delta\Delta\delta + \vec{H}_\gamma\Delta\gamma| \\
d_2 &= \frac{1}{2}|\vec{H}_\omega\Delta\omega - \vec{H}_\delta\Delta\delta + \vec{H}_\gamma\Delta\gamma| \\
d_3 &= \frac{1}{2}|-\vec{H}_\omega\Delta\omega - \vec{H}_\delta\Delta\delta + \vec{H}_\gamma\Delta\gamma|.
\end{aligned}
$$

Here, d_0 is the half length of our step diagonal and $d_1 \ldots d_3$ are the half lengths of the remaining three diagonals in reciprocal space. Thus, formally for the deviation value we have defined the value x as:

$$
x = \frac{\max(d_1, d_2, d_3)}{d_0}. \tag{3.8}
$$

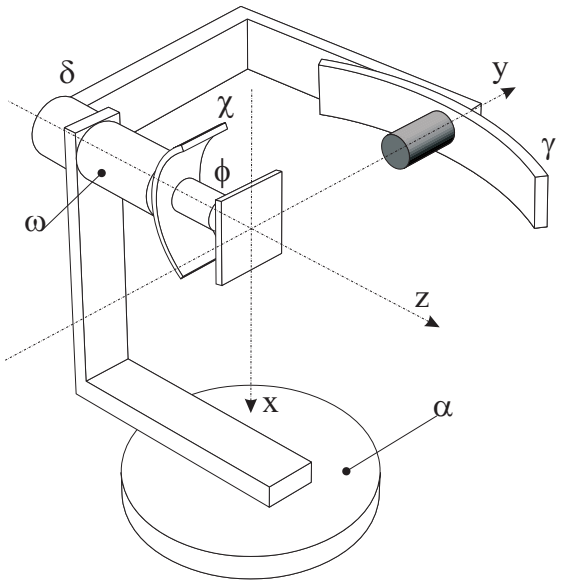

Figure 3.5: The six rotation axes of the six circle diffractometer. All angles are set to zero.

This defines the maximum deviation during a step movement relative to the step size. Defining it this way, x becomes independent of the step length and therefore can be plotted as a general measure to characterize the local quality of a scan. In the following section we calculate these deviations for the example of a two-dimensional reciprocal space map using a six circle diffractometer operating in grazing incidence geometry.

3.3.2 Positioning errors for a six circle diffractometer

The geometry of the six circle diffractometer is shown in Fig. 3.5. The α circle serves to define the incidence angle, the χ and the ϕ circles are used for sample alignment, the ω circle rotates the sample azimuthally and γ and δ are the detector angles. In the current case, the diffractometer is operating in grazing incidence mode with α fixed at an angle close to 0.3°.

The relationship

$$\delta\vec{K} = h\vec{b}_1 + k\vec{b}_2 + l\vec{b}_3 \tag{3.9}$$

for the vector coordinates (h,k,l) has been derived for this geometry by Lohmeier and Vlieg [73]:

$$\Omega X \Phi M U B H = (\Delta\Gamma - A^{-1}) \cdot K_{i,\mathrm{lab}}, \tag{3.10}$$

where K is the incidence vector $(0, k, 0)$, H is the reciprocal lattice vector (h, k, l), and

Ω, X, Φ, Δ, Γ, A are the following rotation matrices:

$$A = \begin{bmatrix} 1 & 0 & 0 \\ 0 & \cos\alpha & -\sin\alpha \\ 0 & \sin\alpha & \cos\alpha \end{bmatrix} \Delta = \begin{bmatrix} \cos\delta & \sin\delta & 0 \\ -\sin\delta & \cos\delta & 0 \\ 0 & 0 & 1 \end{bmatrix}$$

$$\Gamma = \begin{bmatrix} 1 & 0 & 0 \\ 0 & \cos\gamma & -\sin\gamma \\ 0 & \sin\gamma & \cos\gamma \end{bmatrix} \Omega = \begin{bmatrix} \cos\omega & \sin\omega & 0 \\ -\sin\omega & \cos\omega & 0 \\ 0 & 0 & 1 \end{bmatrix}$$

$$X = \begin{bmatrix} \cos\chi & 0 & \sin\chi \\ 0 & 1 & 0 \\ -\sin\chi & 0 & \cos\chi \end{bmatrix} \Phi = \begin{bmatrix} \cos\phi & \sin\phi & 0 \\ -\sin\phi & \cos\phi & 0 \\ 0 & 0 & 1 \end{bmatrix}$$

Matrix B is the transformation matrix from the sample crystal coordinate system into the sample Cartesian reciprocal coordinate system derived in [74], and for the cubic crystal is:

$$B = \frac{2\pi}{a}\mathrm{E},$$

where E is the identity matrix,

$$E = \begin{bmatrix} 1 & 0 & 0 \\ 0 & 1 & 0 \\ 0 & 0 & 1 \end{bmatrix},$$

and a is the lattice constant of the crystal.

In the current work a mirrored geometry of the diffractometer is used [[73]], therefore the mirror matrix M is introduced to the equation. The orientation matrix U accounts for the sample orientation, and for a (001) wafer with the surface plane oriented perpendicular the z axis of the diffractometer being equal to the identity matrix. Without loss of generality we can set the rotation matrices Φ and X to identity matrices. Equation (3.10) can then be rewritten as

$$\vec{H} = \frac{a}{2\pi} M^{-1}\Omega^{-1}(\Delta\Gamma - A^{-1})\vec{K}_{i,\mathrm{lab}}, \tag{3.11}$$

where $\vec{H}$ is a function of the three diffractometer angles (ω, δ, γ) and the equations of the previous section can be used to calculate the deviation values.

Next we plot the surface $\vec{H}(\omega, \delta, \gamma)$ in reciprocal space coordinates for a fixed sample position, thus $\omega = 0$, $\alpha = 0.3°$ and δ and γ within the intervals $[0 \dots \pi]$ and $[0 \dots \pi/2]$, respectively. This surface represents the accessible Ewald sphere in reciprocal space. The plot is shown in Fig. 3.6 for the (001) orientation. For a cubic crystal the radius of the sphere is a/λ, where λ is the x-ray wavelength. The sample rotation angle ω corresponds to the rotation of this half hemisphere around the l axis. The whole accessible reciprocal space volume thus lies inside the half torus shown in Fig. 3.7. The half torus is a plot of the function $\vec{H}(\omega, \delta, \gamma)$ where for each $\delta = \{0, \pi\}$, ω and γ run within the intervals $[0 \dots 2\pi]$ and $[0 \dots \pi/2]$, respectively. The local basis (3.1) is defined anywhere within the accessible reciprocal space volume. We can therefore calculate the exact deviation

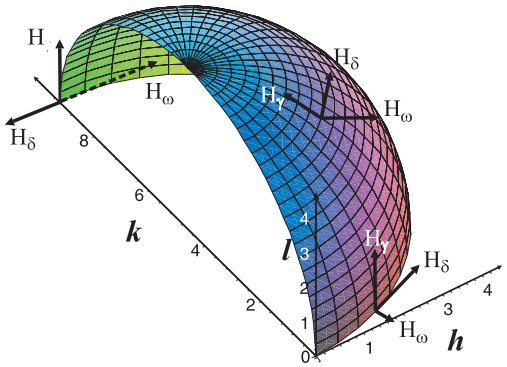

Figure 3.6: The function $\vec{H}(\omega, \delta, \gamma)$ in reciprocal space for a fixed sample position, a cubic (GaAs) lattice with $a = 5.65\,\text{Å}$ and an x-ray energy of 10 keV.

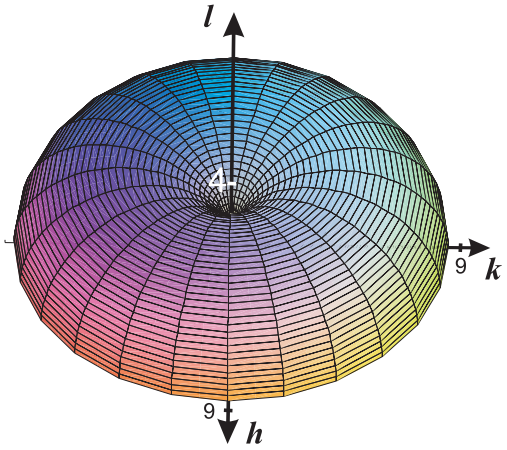

Figure 3.7: The accessible reciprocal space volume calculated for an incidence angle of 0.3°, the (GaAs) lattice constant of 5.65 Å and an x-ray energy of 10 keV.

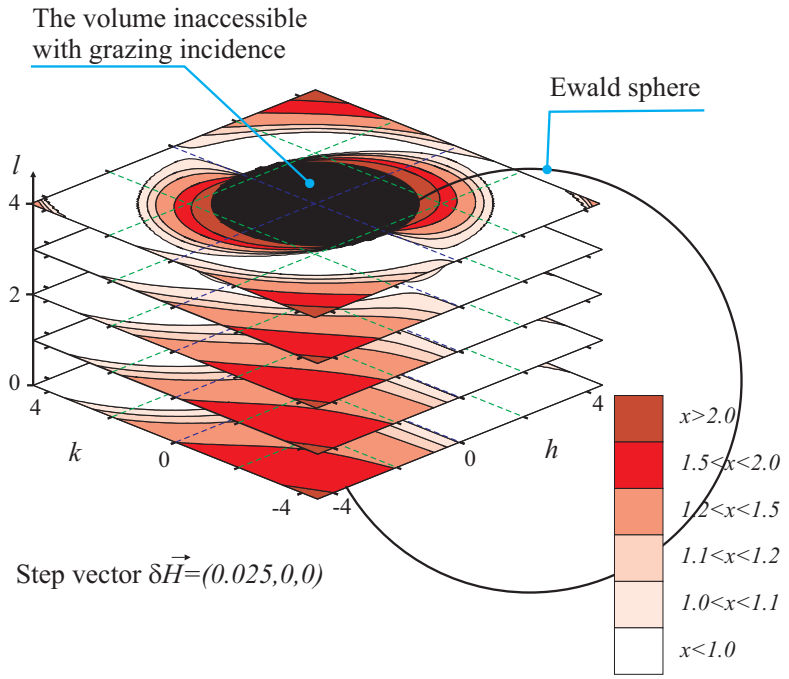

Figure 3.8: Five reciprocal space planes in 3D for surface diffraction from a (001) surface, with the maximum deviation relative to the step size x (see text) presented in various shades of red. The calculations are made for linear mesh scans. The step vector is $\delta\vec{H} = (0.025, 0, 0)$. The white regions represent sub-threshold deviation values (< 1), darker red regions represent increasingly larger deviations.

value x (3.8) for any scan direction and (small) step size. The local basis (3.1) is plotted in Fig. 3.6 at three different locations. The basis is almost orthogonal near the origin where we expect only small deviations for any direction of movement.

We have performed calculations of the deviation x (3.8) for scans along the h axis with a step vector $\delta\vec{H} = (0.025, 0, 0)$, a typical value for our experiments. The plane maps are acquired line by line, the jump from one line to the next is not considered. All calculations are made for a fixed incidence angle $\alpha = 0.3\,^\circ$, a photon energy of 10 keV, and a cubic crystal with a lattice constant of 5.65 Å.

Figures 3.8–3.10 collect the results as color-coded contour maps of the error (3.8) for various planes in reciprocal space. Figure (3.8) shows the location of the $l = const$ planes in 3D that are plotted in Fig. 3.9 in two dimensions. Since we frequently measure in-plane maps, we are most interested in the calculations for in-plane maps, $(H, K, l = const.)$. The white areas in Figs. 3.9 and 3.10 correspond to deviations (3.8) less than unity. In these regions, precise continuous data acquisition can be performed without motor synchronization. For a $90\,^\circ$ rotated step vector such as $\delta\vec{H} = (0, 0.025, 0)$, the distributions are rotated by $90\,^\circ$ around the l axis, see Fig. 3.10.

We conclude that if one measures in the second or fourth quadrant (where h and k have opposite signs, see Fig. 3.9), one should choose the primary scan direction along h and if one measures in the first or third quadrant (h and k both positive or negative),

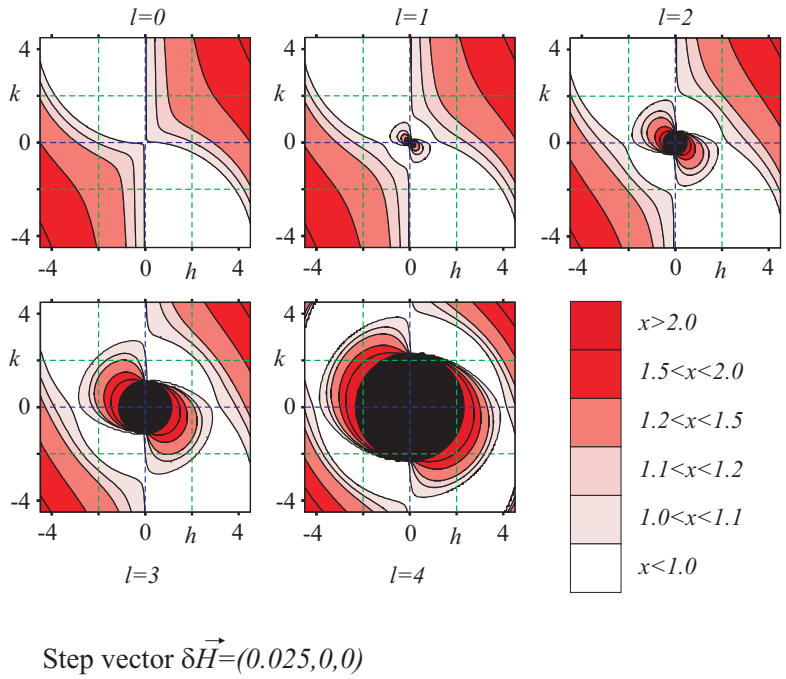

Figure 3.9: Calculated deviation maps of HK-planes for $l = \{0, 1, 2, 3, 4\}$ and step vector $\delta\vec{H} = (0.025, 0, 0)$. The sample geometry is the same as in Fig. 3.8.

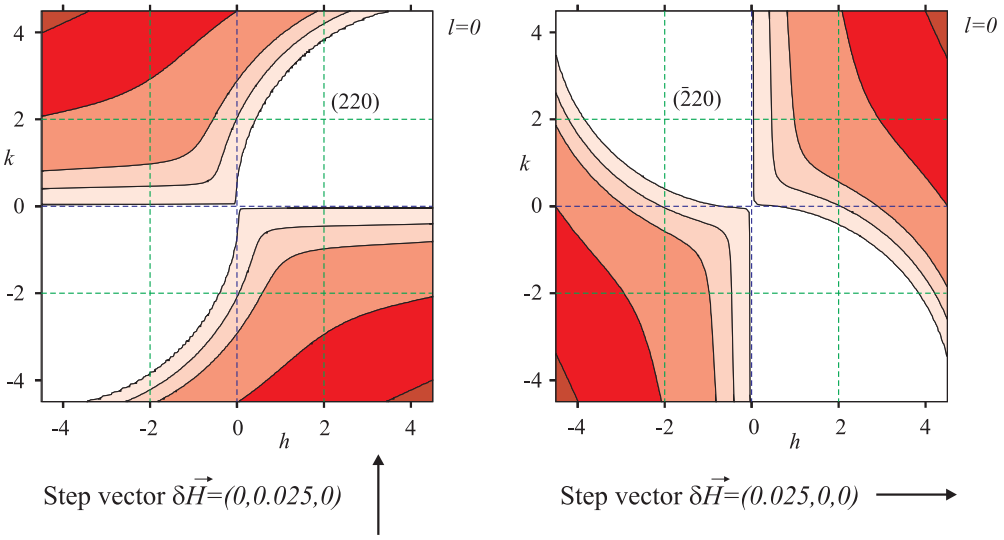

Figure 3.10: Calculated deviations in various HK planes, for $l = 0$ and two orthogonal step vectors $\delta\vec{H} = (0.025, 0, 0)$ and $\delta\vec{H} = (0, 0.025, 0)$

one should choose the primary scan direction along k. Then, no motor synchronization is necessary in a wide area adjacent to the origin.

3.3.3 Additional deviations due to motor backlash corrections

The purpose of the mechanical backlash correction is the elimination of the play in the gears linking the motor with the stage. This is accomplished by introducing reverse motor movements for one of the scan directions in order to always approach a given position from the same direction. For a single motor scan, we can therefore always avoid backlash corrections by choosing the appropriate scan direction. For a general reciprocal space scan, this is not always possible, and we need to consider the movement direction of each motor. We therefore investigate any other possible deviations due to backlash overshoot. The enlargement of the deviation spheres (see Fig. 3.3) due to backlash motions is defined by the following expression:

$$\Delta H < \|\vec{H}_\omega \Delta\omega + \vec{H}_\delta \Delta\delta + \vec{H}_\gamma \Delta\gamma\|, \tag{3.12}$$

in reciprocal space units. Thus, using equations (3.1),(3.11) and (3.12), ΔH can be determined for any point in reciprocal space. For example, for a $\Delta\omega$ value of $0.01\,^\circ$, the deviation is less than 0.00056 reciprocal lattice units near the (2 2 0) reflection. So we may consider it small for all accessible reciprocal space volume only if our step size is significantly larger than 0.001.

3.3.4 Verification experiments

Figure 3.11 shows a 25×25 point reciprocal space map of a small region around the (2 2 0) reflection. The data have been normalized to the monitor detector and separated into two data sets during acquisition. The data set shown on the left was measured using the standard data acquisition mode counting only at the sampled points, whereas the plot on the right represents the data acquired *only* during asynchronous motor motions between steps. The counting time was 3 s for the left panel, and around 1.2 s (the average motor motion time) in the right panel. The calculations for the step vector $\Delta\vec{H} = (0, 0.025, 0)$ show that the deviation value (3.8) is less then one and thus the deviation remains within each pixel of the 25×25 grid. To be precise, the right panel should be shifted by half a pixel in the scan direction compared to the left one. The deviation due to backlash movements (3.12) is also negligible for this step size. The images therefore look very similar, except for different noise levels due to the different counting times. In a standard measurement, the data shown in the right panel of Fig. 3.11 is discarded.

Figure 3.12 shows a ten times magnified area of the same (2 2 0) reflection measured by the traditional method. Interestingly, the reflection is strongly elongated. The direction AB of this streak is exactly parallel to the calculated $\vec{H}_\delta$ vector at the (2 2 0) position. This is due to the widely open slits along the angle δ of the diffractometer. The flight tube of our detector has two slits. During the measurement, the front slit was 10 mm wide and the back slit was 2 mm wide in the direction along the sample surface, so that the acceptance angle $\Delta\delta$ of the flight tube was about 20 mrad. With our incidence angle of $0.3\,^\circ$ and a primary beam cross section of about 1 mm, the full length of the sample along the beam is illuminated. The diffracted beam cross section is therefore strongly elongated in the sample plane, depending on the detector angle δ (see Fig. 3.12). From

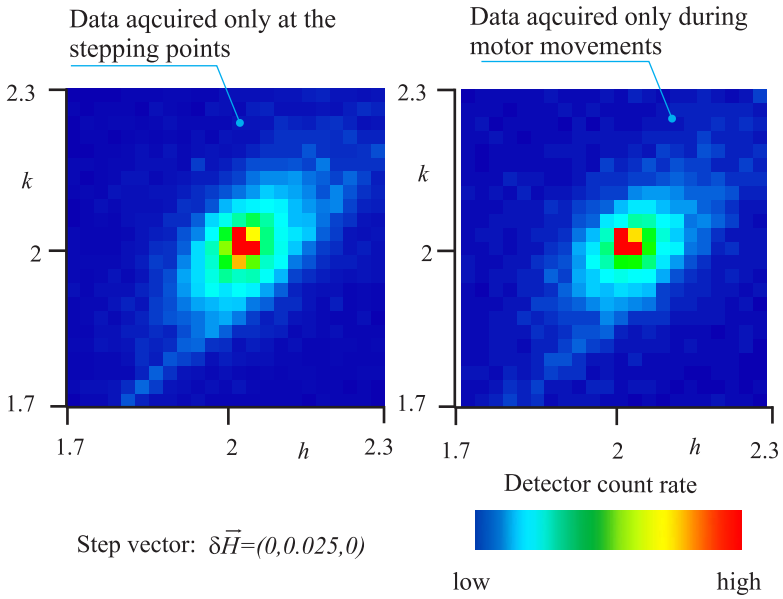

Figure 3.11: Reciprocal space maps parallel to the surface near the (2 2 0) reflection of a $Fe_3Si/GaAs$ sample. The counting time was 3 s for the mesh on the left, and about 1.2 s for the one on the right.

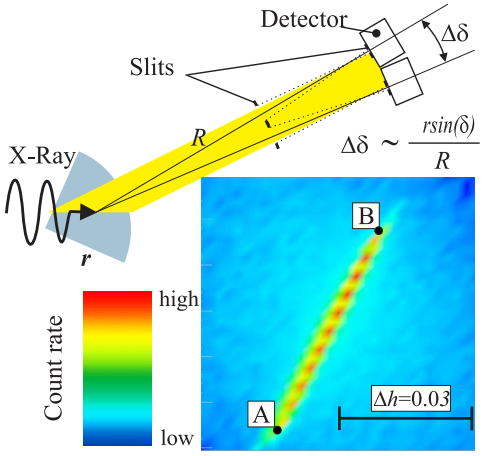

Figure 3.12: Streaky (2 2 0) reflection in grazing incidence geometry. The modulation along the streak AB is due to the 30×30 map grid.

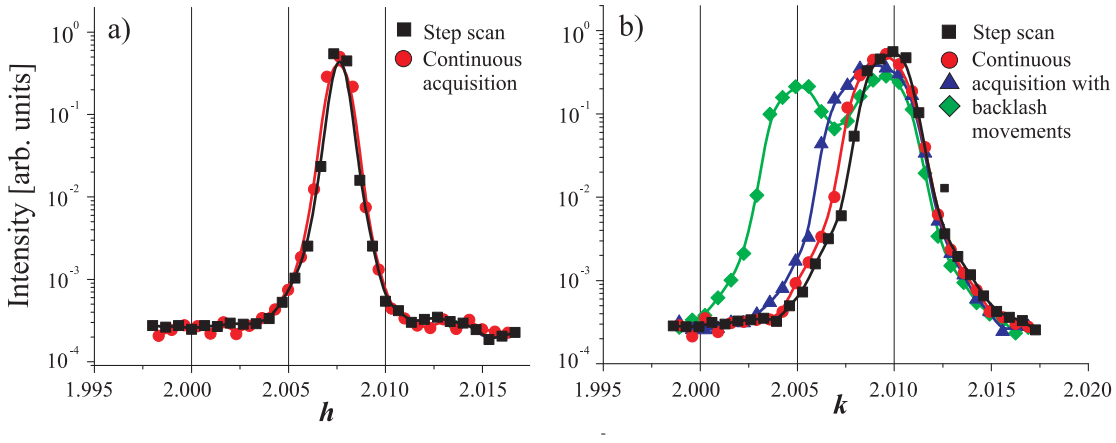

Figure 3.13: The h and k scans of the bulk (2 2 0) reflection acquired traditionally in steps (black rectangles), and continuously during motor movements.

the sample size of $d = 25\,\text{mm}$ and the sample-detector distance of $R = 105\,\text{mm}$, we calculate the range of angles of the diffracted beams that reach the detector to be

$$\Delta\delta = (r/R)\sin(\delta), \tag{3.13}$$

where r is the sample size, R is the distance between the sample and the detector, and δ is the detector angle. The resulting value of 13.8 mrad exactly matches the measured $\Delta\delta$ along the streak AB. We can therefore attribute the apparent elongation of the reflection to the diffracted beam extension due to the grazing incidence of the primary beam.

Figure 3.13 shows two high-resolution h and k scans of the (2 2 0) reflection. The steps used were very small, $\Delta\vec{H} = (0.0007, 0, 0)$ for the h scan in Fig. 3.13(a), and $\Delta\vec{H} = (0, 0.0007, 0)$ for the k scan in Fig. 3.13(b), so that the peak shape is well resolved. The backlash correction values for all motors involved in the scan was set to 0.01 °, 0.02 ° and 0.05 ° for the three measurements denoted by circular, triangular and rhombic data points, respectively. In the actual k scan, only the ω motor performed the backlash motions, and for the h scan, no motor performed backlash motions (the optimum direction for fast data acquisition).

In the figure one can see that the peak shapes for h scans performed in steps are indistinguishable from scans taken using continuous motor movements. A severely distorted peak shapes are for the orthogonal k scans where the distortion increases with increasing backlash correction. We can deduce that (a) the deviation due to asynchronous motor motion is negligibly small, and (b) the backlash motions are responsible for all observed errors. This becomes clear when we calculate the deviations due to the backlash motions according to (3.12). The value $\Delta H = 0.0021$ for the ω backlash correction of 0.05 ° is three times bigger then our chosen step length.

Figure 3.14 shows how the broadening and splitting of the peak in Fig. 3.13(a) occurs. In this scan, the ω motor performs a backlash correction three times as big as the step size, and leads to the integration of the intensity earlier, as indicated schematically by the black trace. For the k scan, the ω motor rotates in the opposite direction, no

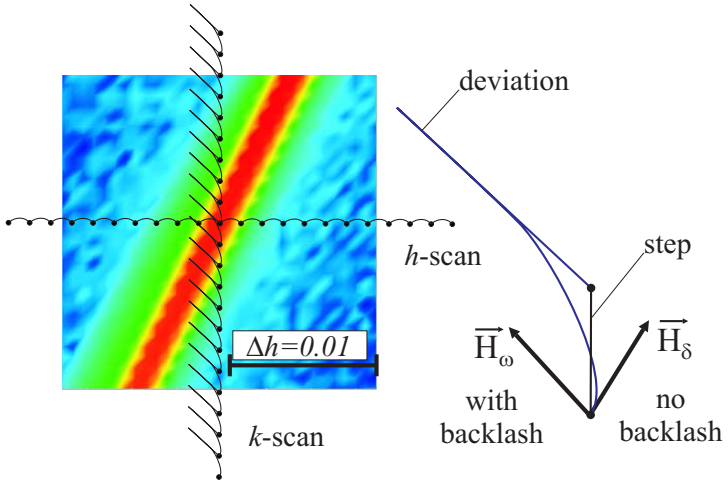

Figure 3.14: Deviations due to backlash correction may cause apparent broadening and splitting of a peak in certain scan directions.

backlash correction is performed, and the peak shape is correctly resolved for both the traditional stepped scan and continuous data acquisition during motor movement.

Highly precise diffractometers have backlash corrections below the instrumental resolution and therefore distortions like the ones due to the artificially large backlash corrections in this example are not observed.

4 Epitaxy of GeTe-Sb_2Te_3 (GST) phase change materials on GaSb(001)

In this chapter, we describe the epitaxial growth process of GST phase change materials on GaSb(001).

We use highest purity Ge, Sb and Te ingots as source materials to produce stable Ge, Sb and Te fluxes. The effusion cell temperatures were kept at 1092 °C, 536 °C and 348 °C during growth for the Ge, Sb and Te cells, respectively. In order to avoid material condensation at the source openings, we use double filament effusion cells with hot lip temperatures 1112 °C, 656 °C and 448 °C for Ge, Sb and Te, respectively.

The GaSb samples were prepared for growth using established III/V epitaxy techniques. A GaSb buffer of 50 nm is always grown before depositing GST to improve the surface quality. W-Re thermocouples were used to control the sample temperature during the experiment. The reported oxide desorption temperature of 530 °C served as a reference point [75]. The growth process was monitored in situ using reflection of high-energy electron diffraction (RHEED) at 20 keV and grazing incidence X-ray diffraction with 10 keV photons (sect. 4.2).

In addition to GaSb(001), we also deposited GST on Si(001)/SiO_2 wafers with 20 nm thermally oxidized silicon for composition control. We determined the composition of the layers grown on these wafers from fluorescence spectra produced by X-ray excitation of the grown films. Due to the element sensitivity of fluorescence, the substrate material needs to be different from the layer to avoid an overlap with the substrate signal. The GaSb and Si(001)/SiO_2 samples were used in an alternating sequence to control possible flux changes from sample to sample. In addition, Si(001)/SiO_2 samples were used for conductivity measurements.

4.1 GaSb(001) homoepitaxy

Successful heteroepitaxy strongly depends on the surface quality of the substrate. In order to reduce surface roughness, we grew buffer layers on each GaSb sample before depositing GST material. We established an experimental algorithm which allows us to prepare exceptionally smooth (1 μm wide terraces) GaSb(001) surfaces. We do not fully understand the atomistic mechanism of the smoothing process. Nevertheless, the method is reproducible and fast for preparing atomically smooth surfaces.

We use 1 mm thick non-intentionally doped p-type GaSb(001) wafers with miscut angles below 0.1°. After introducing the samples into vacuum they are baked in two stages: first up to 150 °C in the load lock and then up to 350 °C in the preparation chamber to remove water and other possible contaminants. The samples are then introduced into the growth chamber.

4.1.1 Oxide desorption

In order to desorb the oxidized surface layer, the sample is heated to 20 °C above the point where desorption initiates. The heating rate is, usually, 0.2 °C/sec. The cell temperatures are kept at 610 °C for the Sb and 860 °C for the Ga source, respectively. The antimony shutter is opened when the substrate temperature reaches 300 °C. At this temperature, antimony no longer adsorbs on the surface.

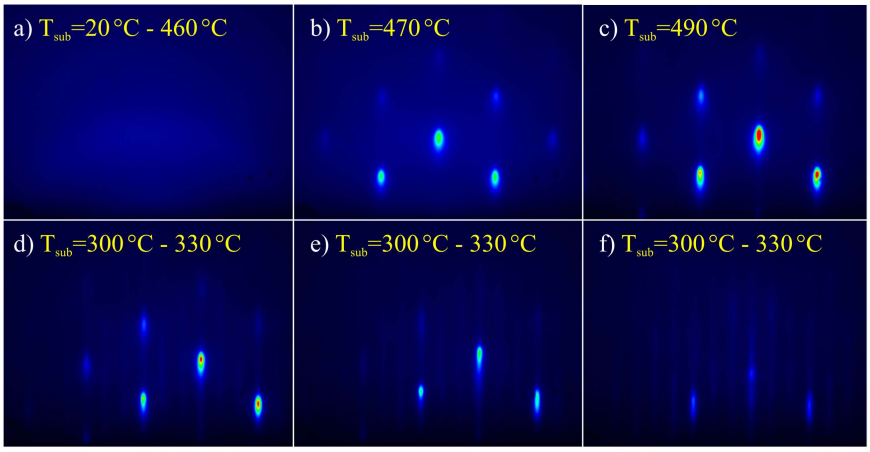

Figure 4.1: Six RHEED screen shots during the oxide desorption and buffer growth procedure

Figure 4.1(a) shows RHEED patterns from an as-loaded GaSb(001) sample. The typical halo diffraction pattern is due to the amorphous structure of the surface oxide layer. At 470 °C, we see transmission diffraction spots appear on the RHEED screen (see Fig. 4.1(b)) while the background intensity is still high. This indicates that the oxide layer has just started to desorb, exposing the rough (producing transmission diffraction) GaSb(001) surface. The given temperatures are relative to the published oxide desorption temperature 530 °C [75, 76]. Our thermocouple shows a temperature of 480 °C at oxide desorption. Usually, we heat the sample 20 ° further to desorb the oxide from the periphery of the sample and obtain the bright spotty RHEED pattern shown on Fig. 4.1(c).

The next step is to cool the sample to 300 °C quickly to avoid surface faceting. The additional weak vertical streaks in Fig. 4.1(d) are a good sign of reconstruction which sets in on flat regions of the surface. The 3× reconstruction is seen along the [110] azimuth.

Once the sample temperature reaches 300 °C, we open the Ga shutter and monitor the intensity of bulk transmission reflections. We manipulate source fluxes and sample temperature slightly to achieve gradual decrease of the bulk spot intensities. Usually, if the intensities do not decrease, it is sufficient to increase antimony pressure. The antimony flux should be significantly higher at the surface than the Ga flux. We should end up at the RHEED pattern shown in Fig. 4.1(f) corresponding to a flat surface. The (11) and (-1-1) surface diffraction rods intersect the Ewald sphere at grazing incidence, thus appear elongated. This length contains information about terraces size and reconstruction domain size on the surface [77]. For the state of the surface shown in 4.1(f)

we obtain an average terrace size of 30 nm. A detailed study of the GaSb(001) surface with RHEED azimuthal scans can be found in a separate publications [78].

4.1.2 Surface smoothing

Once we have a flat surface, it is safe to start heating the sample during Ga and Sb deposition to increase the surface atom mobility. The heating rates are as small as 0.05 °C/s. The RHEED intensity distribution during heating concentrates near the Laue circle (see Fig. 4.2(a)-(d)) for both the fundamental and the reconstruction reflections. This indicates that both the average terrace size and the average reconstruction domain size grow.

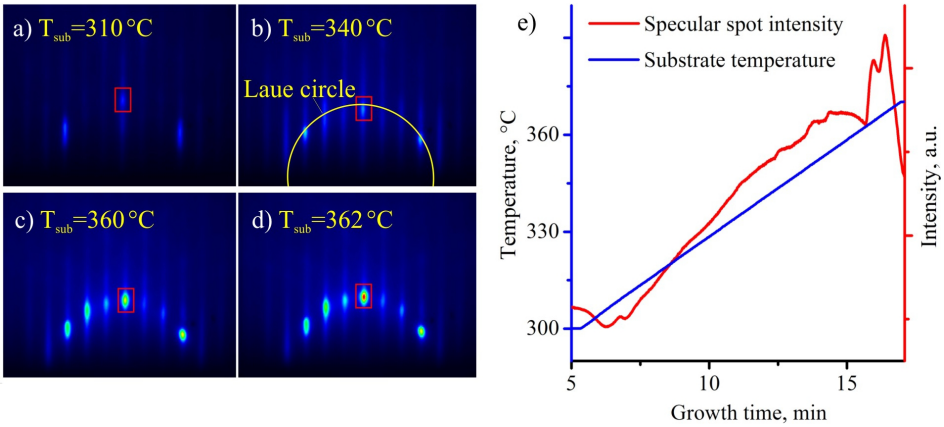

Figure 4.2: (a)-(d) RHEED patterns during GaSb growth and anneal. Intensity concentrates near the Laue circle. (e) Specular spot intensity and sample temperature during growth. The sharp peak at 362 °C seems to correspond to equal Ga and Sb adatom concentration on the surface.

In addition to the thermocouple reading, we have an independent indicator of surface temperature. This is the surface reconstruction, which demonstrates highest sensitivity to the actual temperature at the GaSb(3x1) to GaSb(5x1) reconstruction phase transition.

It is interesting that the reconstruction phase transition temperature depends on heating or cooling rate settings, which seems not physical. However, this means that the sample heats or cools quicker than the thermocouple, but not the other way round.

We observe an interesting RHEED specular spot intensity evolution during sample heating. Initially, the spot intensity increases gradually with temperature, indicating usual surface smoothing due to increasing mobility of the adatoms. Then suddenly, we see a strong intensity boost at around 363 °C, which is visible on Fig. 4.2(e) as a double peak. This peak can be reproduced as many times as required by approaching this substrate temperature from below. We do not see any correlation with any other machine parameters, so we attribute it to a real physical surface effect. The sources are kept at constant temperatures.

It seems that heating the sample during growth beyond the intensity peak leads to unstable growth. The film often becomes very rough for samples grown at temperatures beyond the peak. Thus, the peak should be related to surface processes. The‘peak

may correspond to the optimum temperature, when Sb:Ga adatom concentration ratio is ideal for the formation of stoichiometric GaSb.

We know that many binary materials produce smooth surfaces during MBE growth only if one of the elements has a significantly higher flux at the surface then the other. This element typically has a many orders of magnitude higher saturated vapour pressure. Reversing the situation often leads to surface roughening due to droplet formation. A high volatility of an element reduces its adatom concentration on the surface, thus this is the parameter which changes with temperature even for a constant flux ratio. Probably, varying the Sb:Ga flux ratio could affect the peak, although we have not investigated this in detail.

4.1.3 RHEED growth oscillations

Growth oscillations are a reliable indication of layer-by-layer growth and a locally atomically smooth surface [77]. Their analysis allows us to calibrate the Sb and Ga cells with rather good precision. Figure 4.3(a) shows RHEED specular spot intensity oscillations during GaSb growth. One oscillation period corresponds to the growth of a layer of GaSb half a unit cell thick. The Ga cell temperature is increased in steps of 10 °C starting from 860 °C, while the Sb flux is kept constant. Initially, the Sb flux is supplied in rather big excess compared to the Ga one, so that Ga is the growth rate limiting element. The surplus of antimony sublimates easily due to its high volatility at this temperature. We assume that under these conditions we incorporate all arriving Ga atoms into the surface. Therefore, from the period of the oscillations we determine the absolute Ga flux, while the Sb flux remains unknown. We see that the oscillation

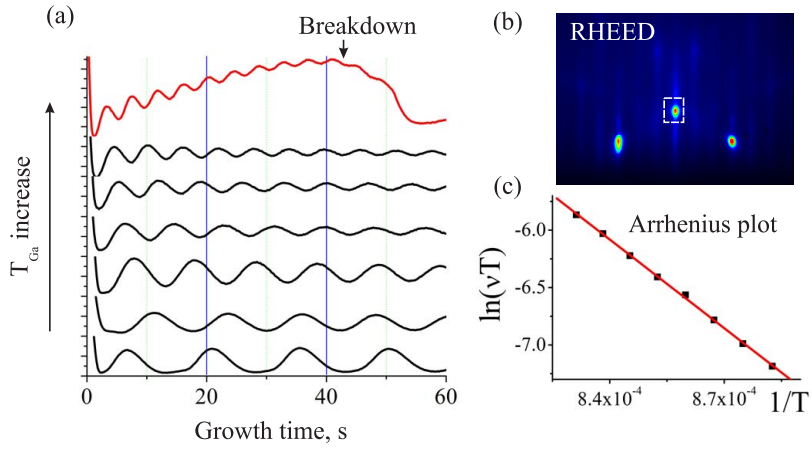

Figure 4.3: (a) Specular spot intensity oscillations at different Ga source temperatures. (b) RHEED pattern before growth with sensor position at the specular spot indicated. (c) Arrhenius plot of oscillation frequency versus reciprocal temperature.

frequency ν increases exponentially with the effusion cell temperature, which becomes obvious in the Arrhenius plot shown in Fig. 4.3(c). The linear fit to the experimental points yields a slope of $2{,}5 \cdot 10^4$ °C, corresponding to an activation energy of 2.2 eV. This value is somewhat smaller then the sublimation energy of pure Ga (2.8 eV), probably

because the proportion of Ga atoms reflected from the surface increase with arriving atoms speed.

We cannot increase the Ga flux indefinitely, because at some point there are not enough adsorbed Sb atoms available on the surface to form stoichiometric GaSb. This point is detectable experimentally by observing the breakdown of the growth oscillations (see red curve on Fig. 4.3(a)). Under these conditions, we have more Ga atoms on the surface than Sb atoms, which due to low vapor pressure of gallium at this temperature form liquid droplets on the surface [79]. The droplets destroy the smooth surface, leading to the breakdown of the growth oscillations. However, this oscillatory curve is very useful, since it represents the deposition rate of both gallium and antimony in equal amounts. Repeating the whole procedure for different Sb source temperatures, we obtain a calibration curve for the Sb cell as well.

Despite nice growth oscillations, we have occasionally observed pits forming on the GaSb surface, with sizes varying from 10 to 100 nm. Figure (4.4) shows an SEM image of such a sample with pits, and two AFM images with different scale. From the AFMs it is clear that the pits themselves are localized on mounds made out of monoatomic steps, with a surrounding surface which is also atomically flat. The density of the pits varies from 0 to $0.1 \mu m^{-1}$. The depth of the pits equals the estimated buffer layer thickness. The depth was determined from other SEM images where the cleaved edge goes exactly through one of the pits. Since the depth of the pits is close to the thickness of the GaSb

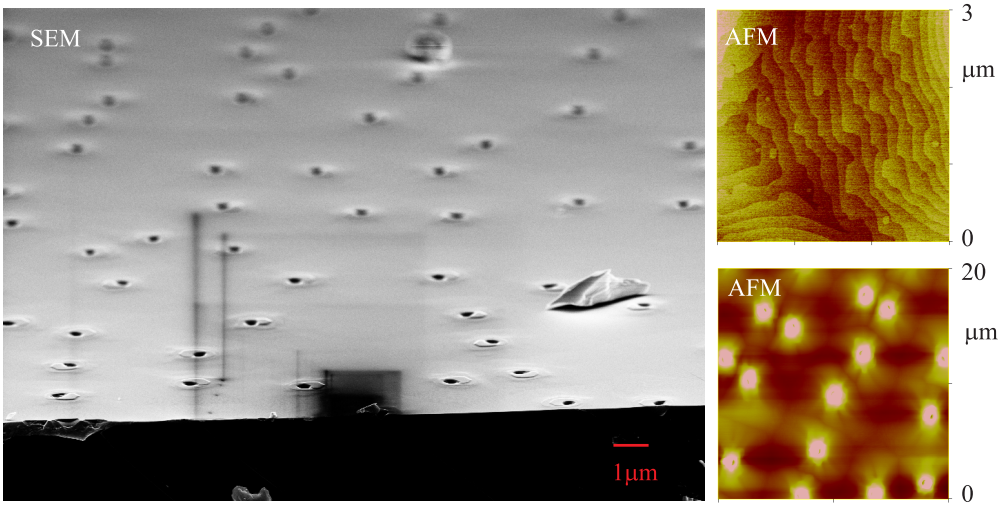

Figure 4.4: Scanning electron microscopy and atomic force microscopy images of a GaSb(001) surface with pits

buffer, we speculate that the pit formation starts from the beginning of growth. In the literature, colleagues fabricate similar pits, but much smaller in size, since they become interesting as "quantum ring" objects as their size shrinks [79]. Unfortunately, our pits are just an undesirable surface defect.

The pit does not look like a typical screw dislocation, since the lateral pit size is large. However, we cannot rule out that this pit size develops during growth, starting from a screw dislocation.

To avoid the pit formation, we have to desorb the oxide with high enough Sb pressure.

Secondly, during buffer growth we heat the GaSb substrate only up to the point where we still see sharp reconstruction streaks in RHEED. Satisfying these rules, we statistically grow better surfaces, although the detailed mechanism of the pits formation remains unknown.

4.2 Epitaxy of GST on GaSb(001) at 200 °C

This section describes the growth experiments of GST on GaSb(001) at 200 °C. This growth temperature was found to be the optimal for the growth of GST on GaSb(001). At this temperature the growing film contains minimum of a polycrystalline inclusions, while still has a high growth rate, which guaranties the film stoichiometry as in the flux. The crystal structure determination, described in the chapter 5, was made on the films grown at this growth conditions.

4.2.1 Ge, Sb and Te source calibration

The epitaxy of Ge-Sb-Te alloys is a challenging and new topic. The first step is the calibration of the elemental sources. The Sb source is calibrated during GaSb homoepitaxy as described in the previous section.

Using a similar procedure, the Ge source were calibrated during Ge/GaAs(001) heteroepitaxy. For the Ge source calibration we have to take into account that the growth oscillation period corresponds not to half a unit cell, but to a quarter of the unit cell. This is because Ge is an elemental semiconductor with diamond instead of zinc blende structure. This was verified by analyzing interference fringes in X-ray crystal truncation rod (CTR) scans. The number of interference fringe periods in between the reflections like (111) and (113) is twice the number of Ge unit cells grown.

We were not able to use RHEED oscillations for the precise calibration of the Te source, since there is no lattice-matched material where Te is the rate limiting element. For a starting value, we grew Te on a smooth GaSb(001) surface at room temperature. The resulting RHEED pattern showed diffuse intensity. To obtain the growth rate, we measured the layer thickness and density by X-ray reflectivity. The thickness of the layer was also determined by scanning electron microscopy. The temperature dependence of the growth rate was approximated by the vapor pressure of Te.

After the initial calibration, the first Ge-Sb-Te layers were deposited at room temperature on SiO_2/Si(001) substrates with the aim to obtain a 2:2:5 ratio for Ge, Sb and Te, respectively. The compositional analysis carried out by our partner group in Japan gave a 26:37:38 ratio for Ge, Sb and Te, respectively. They induce X-ray fluorescence of the sample surface using high energy electrons. The fluorescence spectra yields intense X-ray peaks at the core-shell energy levels of each element. From the peak positions and their intensities the composition is determined. The composition for each following sample was then adjusted by further fluorescent measurements. Therefore, for the first experiments we decided to use stoichiometric fluxes of Ge, Sb and Te respectively.

4.2.2 In-situ growth observations of GST

Figure 4.5 shows nine RHEED images taken at different moments after the joint deposition of Ge, Sb and Te was started. In the first frame we see the typical streaks

corresponding to the 5× GaSb surface reconstruction with peak intensities on the Laue circle implying a relatively smooth GaSb(001) surface. The initial stage of growth is characterized by a continuous intensity decay leading to an entirely diffuse pattern 100 seconds into the growth.

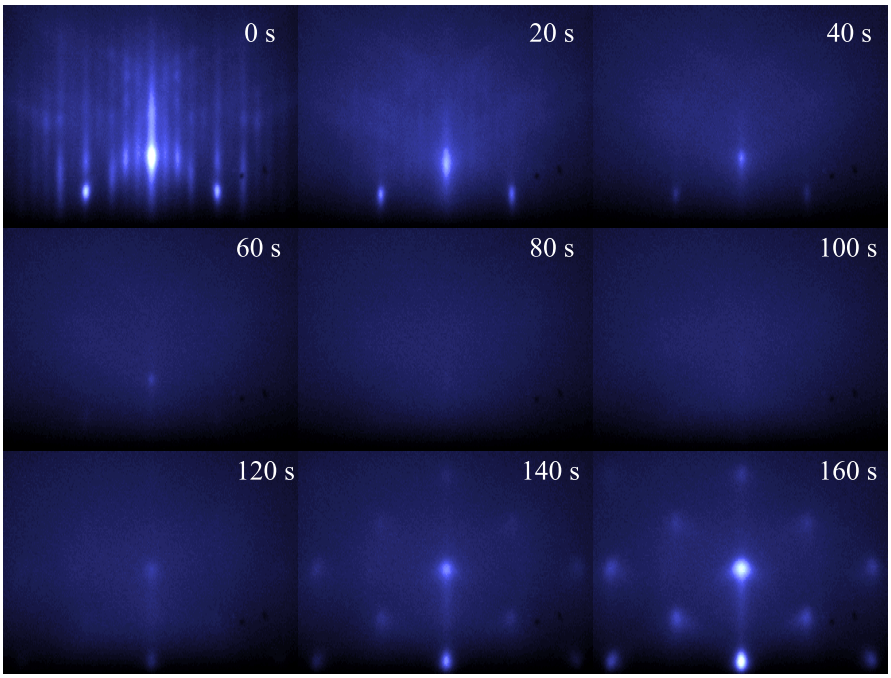

Figure 4.5: Reflection high energy electron diffraction patterns during the growth of GST/GaSb(001)

The layer thickness at this moment is around 0.6 nm, which corresponds to the size of one cubic $Ge_2Sb_2Te_5$ unit cell. A totally diffuse RHEED pattern indicates two things: we have fully covered the surface and we have a completely amorphous layer at this stage.

At 120 seconds, the situation changes drastically. We see the development of a bright spotty pattern typical for bulk diffraction from a single crystal. Bulk diffraction in grazing incidence geometry occurs when the surface roughness is high enough to allow electron transmission. The coherence length of the electrons is small compared to the illuminated area, thus we obtain an incoherently averaged diffraction pattern. We see a single crystal diffraction pattern, thus we conclude that the film is fully epitaxial. The in-plane lattice constant coincides with that of GaSb or the cubic phase of GST within the experimental resolution.

Further growth proceeds without significant changes in the RHEED pattern, despite the development of weak inclined streaks along the <111> directions. The origin of the streaks we attribute to <111> facets developing on the surface.

To determine the in-plane symmetry, we perform azimuthal RHEED scans as described in [80]. Figure 4.6 shows the reciprocal space pattern obtained from such an azimuthal scan. This demonstrates that we have body centered cubic symmetry in reciprocal space, which implies a face centered cubic real space lattice of the film.

Surprisingly enough, despite the amorphous layer forming at the beginning of growth,

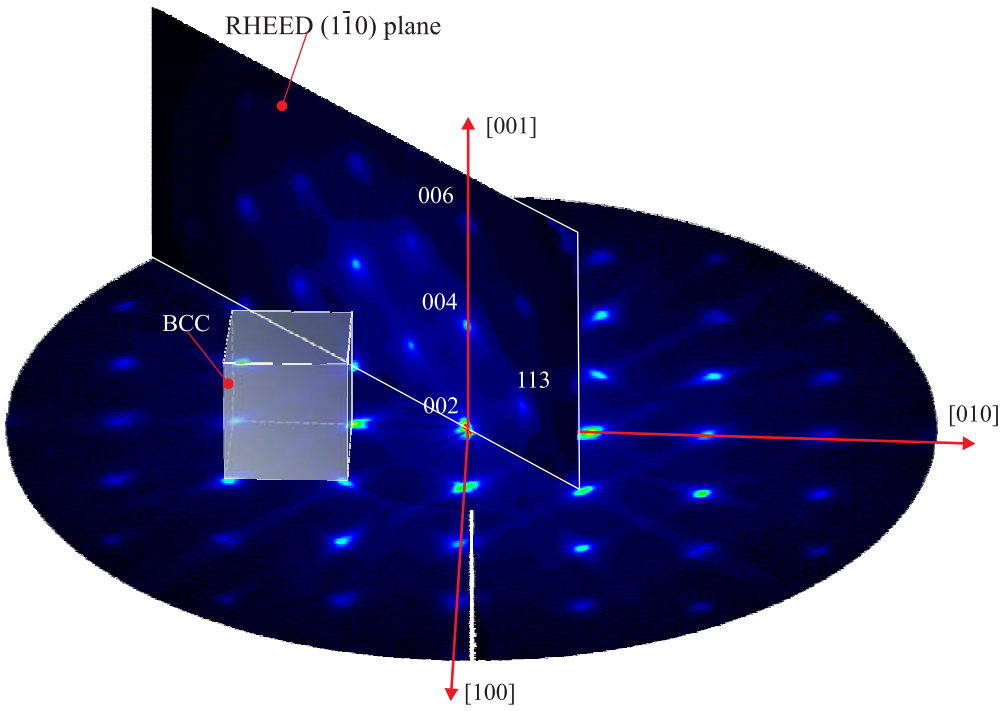

Figure 4.6: Intensity distribution in 3d reciprocal space revealed by a RHEED azimuthal scan after one hour of growth. The body centered lattice is clearly visible

the film has the same orientation as the substrate. We therefore speculate that, after a certain incubation time or critical film thickness, crystallization either has started from the substrate and then grows reproducing the substrate symmetry, or crystallization takes place somewhere in the amorphous film, but only the grains that experience an energy gain due to their accidental correct epitaxial orientation finally dominate. As crystalline GST has a large number of voids, the formation of these voids at the surface may be difficult and have a large energy barrier, therefore promoting nucleation in an amorphous bulk layer.

4.2.3 The growth process observed by X-ray diffraction

Due to their strong interaction with matter, diffracting electrons are sensitive to the surface or a rather thin surface layer. Because of multiple (dynamical) scattering, it is difficult to analyze RHEED quantitatively. X-rays at 10keV have low absorption and a small scattering cross-section [51]. One can calculate that for GST, X-rays at 10 keV easily penetrate 15 μm deep, what for grazing incidence of 0.7° gives a thickness of 150 nm. Typical thicknesses of our films are below 60 nm, thus we may neglect absorption. This means that X-rays pass through the whole film and penetrate deep into the substrate, thus becoming sensitive to the entire volume of the film.

Figure 4.7 shows X-ray measurements performed near GaSb(220) during growth. The scan direction is along the surface in the radial direction. The narrow peak originates from the GaSb substrate, while the broad shoulder is due to the growing layer. We see that at a certain thickness, the layer peak becomes easily distinguishable from the

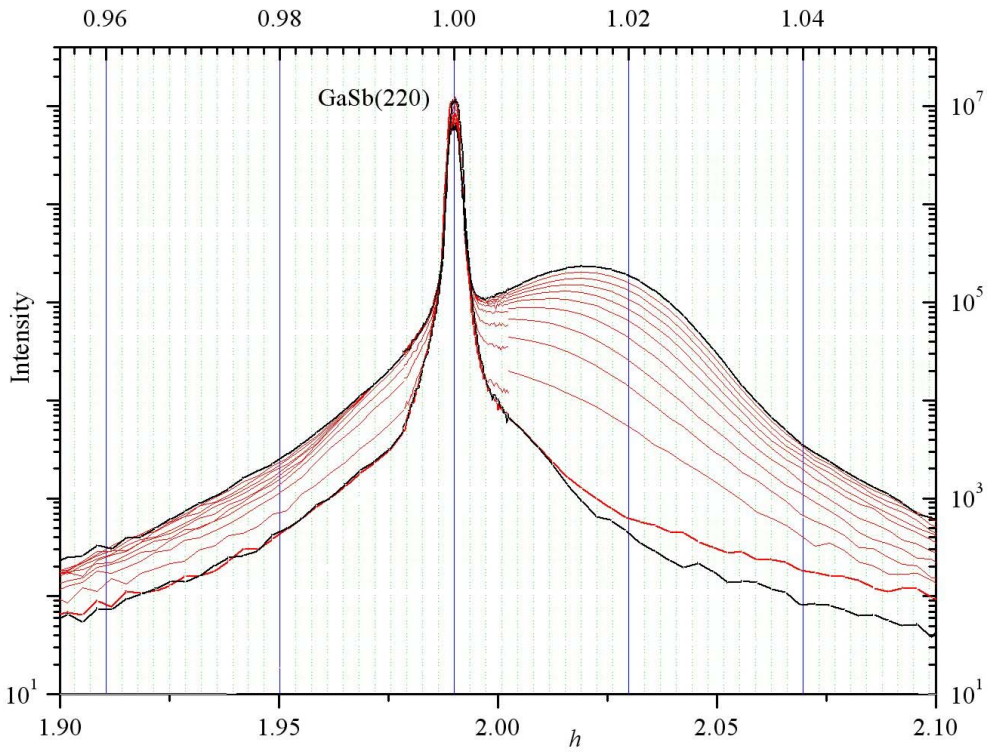

Figure 4.7: In-plane X-ray intensity around the GaSb(220) reflection during growth, indicating continuous relaxation of the film.

substrate peak, and can be fitted by a Gaussian function. From the Gaussian fits, the peak parameters like intensity, area, width and position can be extracted. The results are shown in Fig. 4.8. From the asymptotic behavior, we expect that the peak width and lattice constant saturate at constant values for long growth times.

We see that the lattice constant increases as we extrapolate back to the onset of growth and approaches that of GaSb. Normally, for the growth of mismatched heterostructures the film should relax abruptly at a certain critical thickness, or grow relaxed from the very beginning. It is unlikely that this lattice constant deviation is a fitting artifact due to the presence of the substrate peak, since we excluded the points in the substrate peak range. We also fit the experimental points obtained after 20 min of growth, when the layer peak became well separated from the substrate peak. This could mean that we have both strained coherently matched and relaxed domains initially, but only the relaxed ones grow, or we have multiple strained domains which relax during growth. This is an indication that we do not have a single solid film, but multiple crystal grains weakly constrained by each other, but, nevertheless oriented by the substrate. Further measurements are required to clarify this issue.

The peak width decreases slightly during growth. We analyze the origin of the peak broadening in the next chapter. The area of the peak as a function of time is approximated well by a line, and the line extrapolates to zero at the onset of growth (see Fig. 4.8(d)). This means that the epitaxial cubic phase is homogenously distributed along

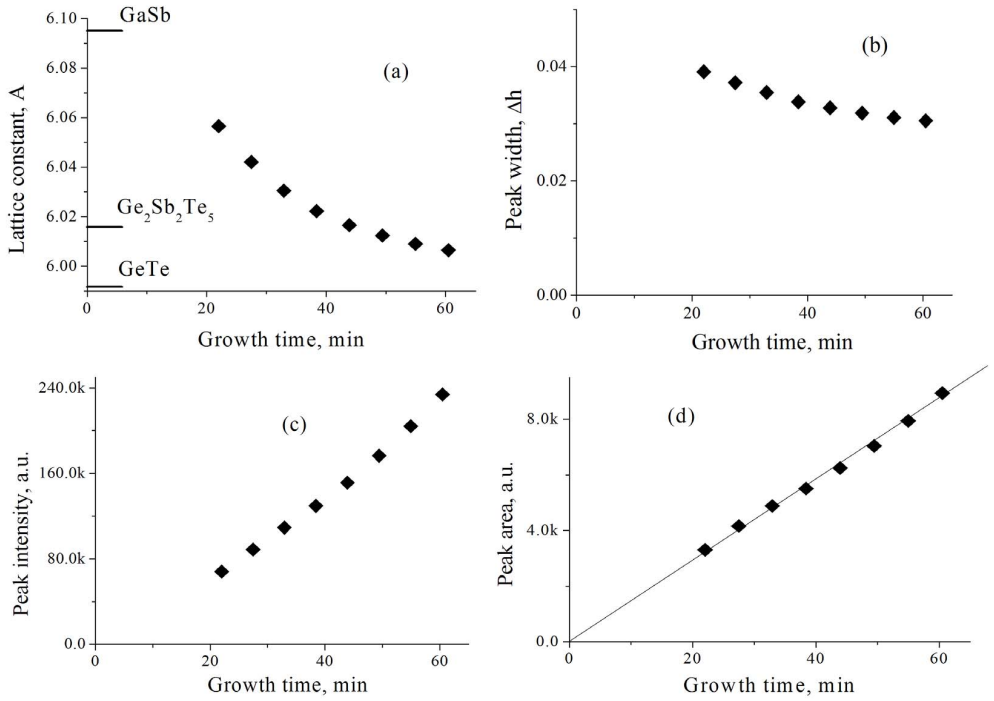

Figure 4.8: Lattice constant, layer peak width and intensity evolution during growth. The results were obtained from Gaussian fits to the GST(220) layer peaks shown in Fig. 4.7. The fit was made for film thicknesses for which the peaks were bright enough to separate them from the GaSb(220) reflection

the growth direction and grows at a constant rate. Since the peak width changes only slightly, the peak intensity is approximated by a straight line as well. Probably for scans in orthogonal directions the situation is similar. Therefore, the intensity integral 2.39 is proportional to the peak intensity. This means that our peak intensity is proportional to the amount of the epitaxial film grown.

4.2.4 In-plane film crystal structure revealed by X-rays

Figure 4.9 shows a typical X-ray reciprocal space map for $l = 0.005$ and a layer thickness of 30 nm. The intensity is shown by color in logarithmic scale. We see the combined diffraction pattern from all possible crystalline structures present in the film. To save time, actual measurements were performed for h and k in the range $(0 \ldots 4.2)$ and then mirrored into the other three quarters. Therefore, in principle, some artificial symmetry could arise. Nevertheless, the presence of all intense reflections was confirmed by additional scans. The result demonstrates that the epitaxial cube-on-cube phase dominates, however some amounts of other orientations are also present. In addition to the cubic, we also observe a hexagonal symmetry, which was not observed by RHEED in the azimuthal scans. This is due to the poor sensitivity of RHEED to the bulk of the film. Therefore, the corresponding structure may be localized close to the interface. The interplanar distance for the closest hexagonal peaks is 4.24 A, very close to the lattice constants of all thermally stable hexagonal phases of GeTe-Sb_2Te_3 along the

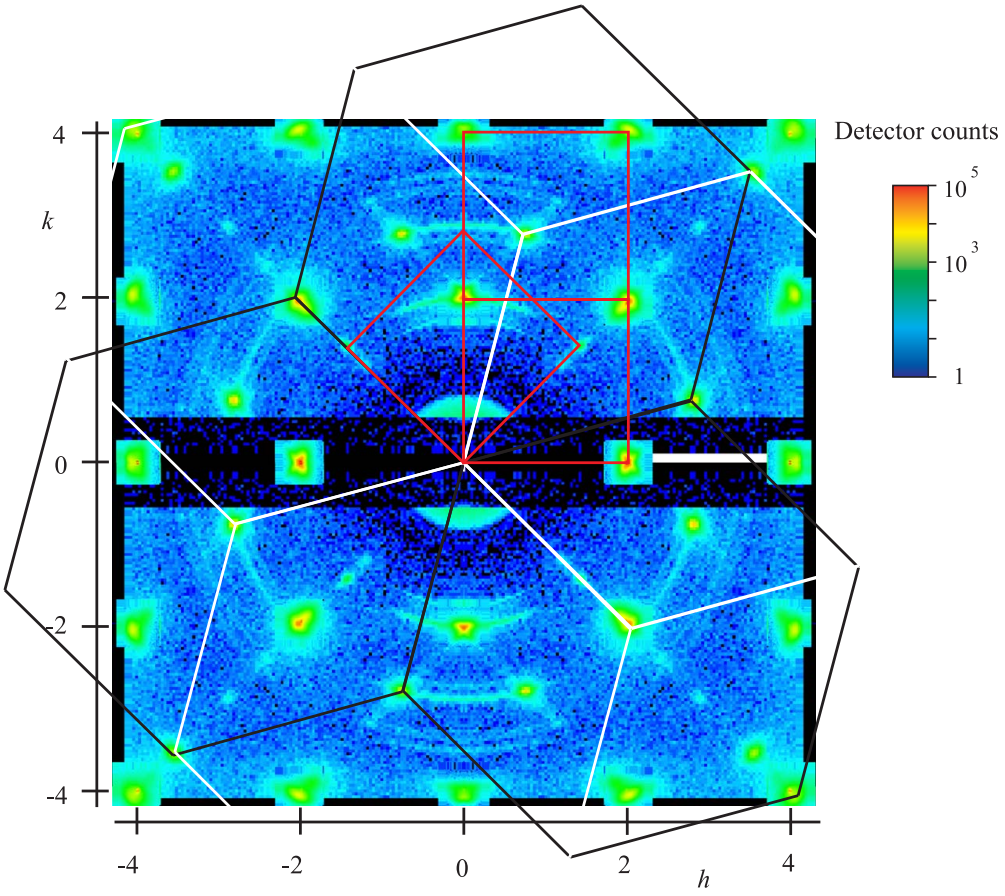

Figure 4.9: An X-ray reciprocal space map of the grown film reveals the same cubic symmetry as in RHEED plus additional hexagonal symmetry

pseudobinary line [35, 36, 37, 38, 39]. Therefore, from this reciprocal map we can conclude, that our film consists entirely of epitaxially oriented crystals from the GeTe-Sb_2Te_3 group.

It is worth to say that we do not detect any peaks corresponding to pure Ge, Sb or Te crystalline phases, indicating that we do not have significant phase separation onto pure Ge, Sb and Te crystals. We can not exclude, however, that we do not have these pure elements in the amorphous state.

In order to attribute the hexagonal symmetry to a certain structural phase, the complete out-of-plane reciprocal lattice structure is required. Since we do not have an area detector for this purpose, we performed linear and planar out-of-plane scans at the expected positions. We found a correspondence of the hexagonal peaks to the simple volume centered cubic structure with <111> orientation, which probably is the most likely explanation.

Summarizing this paragraph, we have seen that the film predominantly has cube-on-cube epitaxial domains with FCC lattice (Fig. 4.10(a)), probably two orientations of cube<111>-on-cube domains (Fig. 4.10(b,c)) with FCC lattice and a small fraction of 45 °-rotated domains (Fig. 4.10(d)).

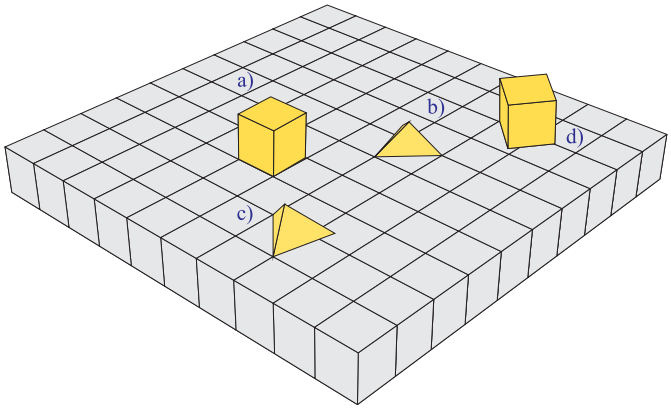

Figure 4.10: Schematic representation of epitaxial film orientations: (a) cube-on-cube, (b),(c) two domains of cubic(111)-on-cube, (d) 45°-rotated domains.

4.2.5 Discussion of the growth mechanism

Typical sample cross sections obtained from scanning electron microscopy (SEM) are shown in figure 4.11(a,b) for two different samples. We clearly see that the layer contrast is not homogeneous, indicating either crystalline grains present in the film, inhomogeneous composition or even voids. Different from the polycrystalline case, as we have seen, is the identical orientation of all the crystallites. It is not trivial to explain the significant difference in surface roughness, since the samples were grown at the same nominal growth temperature. The only parameter which might be different is the Ge:Sb:Te stoichiometry. We may guess that as soon as we approach the "right" stoichiometry, which may be 2:2:5 (GST), we get smoother layers.

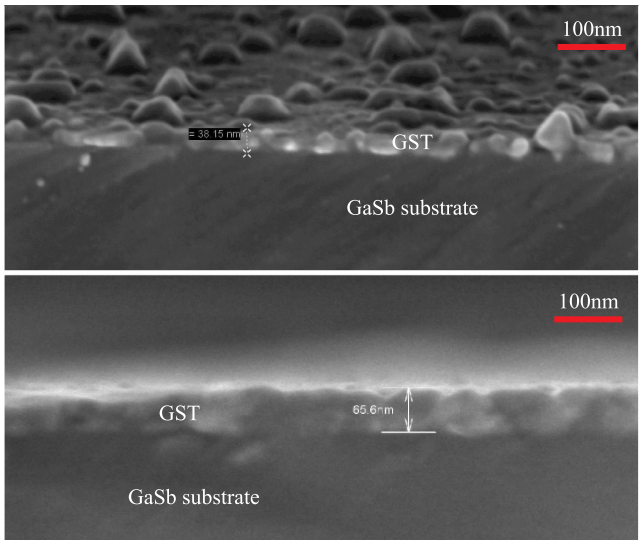

Figure 4.11: Scanning electron microscope images of two different samples grown at the same growth temperatures

We are now facing an important question: do we have a single or a multi-phase

system?

As we have already discussed in the introduction, GeTe has a distorted NaCl structure, while Sb_2Te_3 has a layered hexagonal structure. Their alloy, GST, forms several phases with integer stoichiometries of the pseudobinary constituents GeTe and Sb_2Te_3. For what we know so far all these phases possess layered hexagonal structures with different stackings along the c direction. According to the phase diagram (see Fig. 1.4) they all possess the distorted rock salt structure in the metastable phase.

We would like to emphasize here that all these phases have not only similar structures, but close lattice constants (only the c axis of the hexagonal phase varies).

Therefore, all diffraction data we have discussed up to now fit well to different phases from the GeTe-Sb_2Te_3 pseudobinary line. To find out which one it is or whether it is a mixture, a more detailed film structure analysis is required. For example, the in-plane cubic symmetry in figure 4.9 could correspond to both cube-on-cube GeTe/GaSb and GST/GaSb phases, while hexagonal could originate from Sb_2Te_3 with the c axis orthogonal to the surface.

In the next chapter, we will show that the metastable cubic GST we grow has a rhombohedral distortion, similar to that in GeTe [32]. This could mean that the rhombohedral distortion is typical for all "cubic" phases of Ge-Sb-Te alloys. Therefore, let us assume that initially we form a lot of differently inclined nuclei, each having slightly inclined growth directions. The crystalline domains, thus, grow in an inclined direction and meet, creating unremovable grain boundaries and even voids. Surface roughness and SEM contrast inhomogeneity could be due to such a growth mechanism. We think that trying (111) oriented wafers could help to compensate for the distortion by allowing it to relax in the growth direction.

4.3 Growth of GST at various temperatures

We now show that the epitaxy of GST at temperatures above 210 °C should be interpreted with additional care. In this and the next section we will show that significant material desorption takes place at these temperatures. We will show that small amounts of adsorbed material which change the reconstruction are not necessarily followed by subsequent growth.

We find that tellurium is likely responsible for the high volatility of our films at high temperatures.

4.3.1 Etching at high temperatures

In this section we discuss the growth process for substrate temperatures in the range 270–370 °C. A typical RHEED pattern during growth is shown in Fig. 4.12(a). As soon as the Ge, Sb and Te shutters are opened the RHEED intensity immediately rises by a factor of three. The pattern indicates a flat surface. The higher intensity may be due to higher surface scattering as heavy Te atoms are attached to the surface. Further growth proceeds without significant changes in the diffraction pattern, apart from a slow intensity decay.

Normally, this behavior would be associated with good 2D epitaxy. Unfortunately, X-ray reflectivity data obtained during growth indicates the absence of any film on

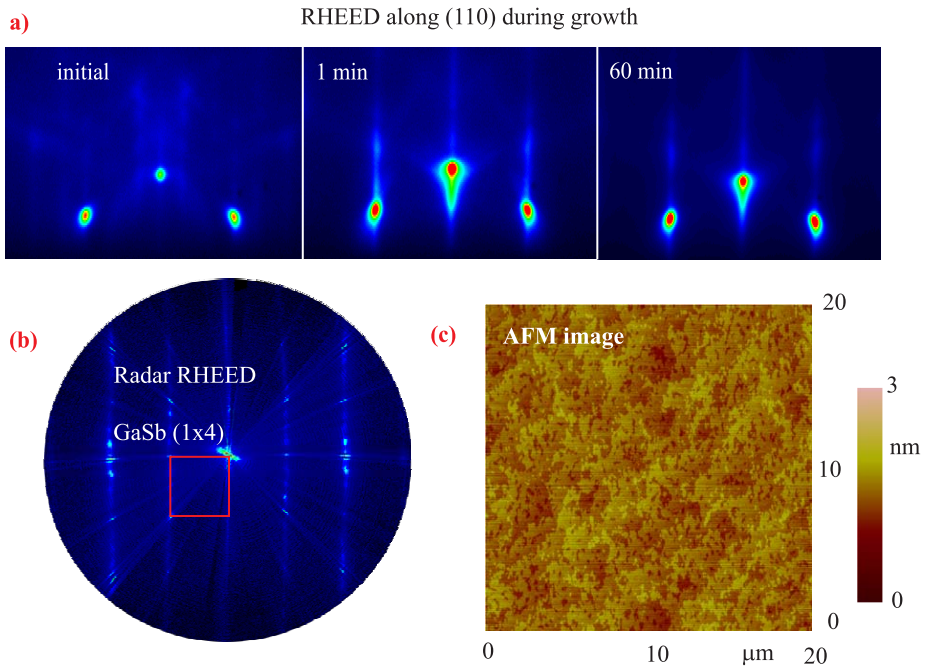

Figure 4.12: (a) RHEED pattern during GST deposition at high temperatures. (b) An azimuthal scan performed after one hour of deposition reveals a flat surface showing the new (1×4) reconstruction. (c) Atomic force microscopy images confirm an extremely flat surface with 3 μm wide monolayer high terraces.

the surface, which means that material is reflected from the surface at this temperature. The azimuthal scan 4.12(b) shows a (1×4) reconstruction, different from the GaSb(3×1), therefore some material must have incorporated to the surface at the beginning of growth. Atomic force microscopy (AFM) of the film shows an atomically flat surface with 3μm wide terraces (see Fig. 4.12(c))

In contrast to our expectations, Ge does not stick to the surface at 270°C. Additional experiments show that it sticks quite well in the absence of a Te flux. A combination of Sb and Ge fluxes impinging on the surface at elevated temperatures do not form a phase on the surface, but germanium islands. As soon as the Te flux is added, however, we can etch even a few nanometer thick GST layer down to the substrate at temperatures above 250 °.

To demonstrate the etching effect of Te, we performed the following experiment: We supplied Sb, GeSb, GST and SbTe fluxes alternatively and monitored the behavior of RHEED pattern. We assumed that an intensity decay of the GaSb(001) RHEED pattern is associated with a corresponding surface coverage by amorphous material.

Figure 4.13(a) shows RHEED intensity plotted versus growth time. The intensity is integrated within the red rectangle shown in Fig. 4.13(b). Initially, when only the Sb flux is supplied, the GaSb surface is stable and RHEED intensity is constant. When we open Ge and Te in addition to Sb, we see the intensity boost corresponding to the smooth and stable GaSb(1x4) surface. Now, if we close the Te shutter, material (presumably germanium) grows on the surface, and the RHEED intensity decays rapidly. Growth under these conditions leads to Ge cluster formation. We close the Ge shutter

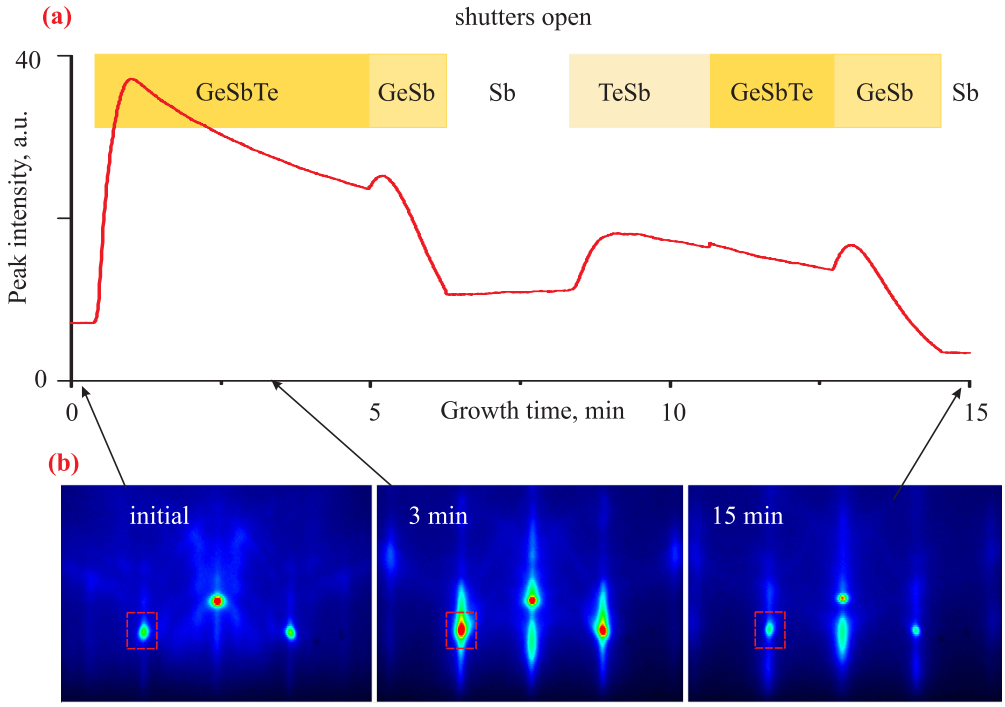

Figure 4.13: (a) RHEED intensity variation with various molecular beams directed to the surface. (b) RHEED pattern at three different moments of the growth.

stabilizing the surface again. Opening the Te shutter recovers the surface since the RHEED intensity grows. Now, if we open the Ge shutter again, it causes no effect on the RHEED pattern! Thus, we conclude that Ge does not stick to the surface under a Te flux. Furthermore, we are able to etch the fully covered surface by tellurium. Pure antimony and tellurium can not grow at these temperatures, since we are not in the supersaturation regime for them.

4.3.2 Volatile materials for non-volatile memory

It seems that somehow the presence of a Te flux prevents the growth of Ge (or GeSb). Therefore, Sb and Ge adsorbed atoms (molecules) likely react with the Te atoms (molecules) on the surface. Performing site-to-site jumps on the surface, elements meet together and nucleate a GST-related phase. This phase sublimates from the surface because of its higher vapor pressure compared to pure Ge. Thus, less than one monolayer remains on the GaSb surface which only changes its surface reconstruction. This monolayer does not necessarily have to desorb, since its desorption is not determined only by the GST vapor pressure any more, but depends on its interface energy.

To investigate the volatility of our layers, we varied the substrate temperature during GST deposition and monitored the RHEED pattern. In addition we monitored the sample chamber pressure by ion gauges facing the sample surface. Since atom (molecule) trajectories at 10^{-9} mbar are ballistic, we are sensitive to reflected material from the surface. Elemental fluxes can be imagined as a "beams" of certain "color" which partially reflect from the sample surface. A molecule arriving at the chamber walls is considered

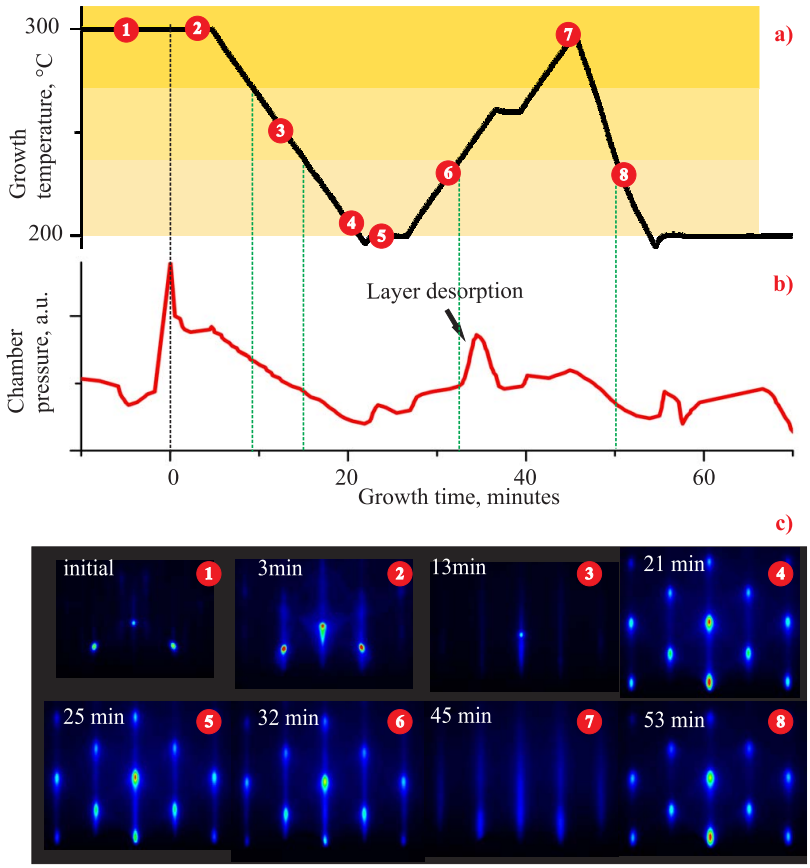

Figure 4.14: (a) Temperature variation during growth. The three regions separated by color distinguish three growth regimes: no sticking, incomplete sticking and full sticking (b) The sample chamber pressure reading is sensitive to material leaving the sample surface. (c) RHEED patterns at different moments of GST deposition indicating crystal nucleation, growth and desorption. The numbers indicate selected moments in the growth sequence.

to stick there permanently.

Figure 4.14(a) shows a substrate temperature plot during the growth of GST, and 4.14(b) is the corresponding ion gauge signal. Numbers in figure 4.14(a) indicate the corresponding RHEED patterns in figure 4.14(c).

From the starting point at 300 °C, the temperature was decreased gradually during GST deposition. In the range 300–270 °C, we see the bright RHEED pattern corresponding to a flat surface. From 260 to 230 °C, we see a dimming of the RHEED pattern due to the coverage by amorphous material and at around 230 °C, the transmission diffraction pattern of the epitaxial structure appears. With this deposition sequence, we have avoided the initial amorphous layer formation, but still have a 3D growth mode. Now we gradually increase the substrate temperature. The transmission diffraction switches to a surface diffraction pattern. This is associated with surface smoothing, but unfortunately due to the desorption of the nucleated structure. We clearly see the pressure peak in the ion gauge signal (see Fig. 4.14(b)) coinciding with the moment when the

RHEED pattern changes. This indicates that surface loses the deposited material, which is confirmed by in-situ X-ray reflectivity.

We can therefore distinguish the growth regimes below the transition temperature and above. The X-ray reflectivity data shows that the growth rate decreases rapidly at temperatures above 210 °C. This may strongly affect the layer stoichiometry, which is kept at 2:2:5 for Ge, Sb and Te, respectively. Furthermore, we speculate that the vapor pressure of the GST-related phases is in between that for Sb and Te, since antimony desorbs from the surface at around 280 °C and tellurium at around 200 °C.

4.3.3 Amorphous growth and crystallization

For low enough growth temperatures, the GST film forms an amorphous phase on both GaSb(001) and SiO_2/Si surfaces. A typical RHEED pattern for GST grown at room temperature shows a completely diffuse intensity distribution (see Fig. 4.15). Annealing of the film to 210 °C leads to the formation of a weak ring pattern indicating polycrystalline crystallization of the film. Typical crystallization temperatures were around 200 °C for a heating rate 0.1 °C/sec.

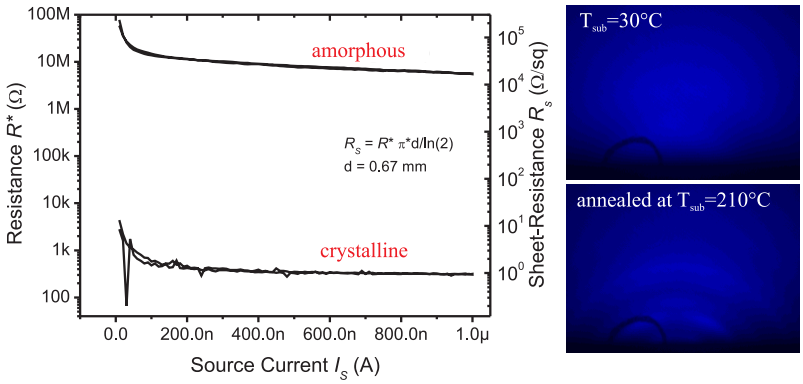

Figure 4.15: The resistance of a GST film deposited on SiO_2/Si drops by four orders of magnitude after annealing. The RHEED patterns on the right correspond to fully amorphous and annealed crystalline layers

Amorphous and annealed polycrystalline samples exhibit a resistance contrast of up to five orders of magnitude as seen from Fig. 4.15. The conductivity measurements were made using a four probe method on our as-grown and crystallized GST/SiO_2/Si samples by F. Merget and M. Foerst, Institute of Semiconductor Electronics, RWTH Aachen.

We see that the resistance contrast is even higher than the one reported for GST phase change materials fabricated by sputtering [81, 82]. This may be due to the higher purity of the films grown by MBE. Therefore, we identify our crystallization with the typical phase transition of GST with the typical high resistance contrast. Furthermore, this result indicates that epitaxially grown GST phase change materials may have superior properties compared to GST produced by sputtering.

4.4 Physical properties of epitaxial GST/GaSb(001) films

As already mentioned, the compositions of the epitaxial GST/GaSb(001) samples were not determined. The only information related to the composition of epitaxial films are the absolute fluxes of the Ge, Sb and Te sources. In order to determine the fluxes of these elements, we deposited Ge, Sb and Te simultaneously on Si wafers with 20 nm thermally oxidized silicon. The composition of the GST/SiO_2/Si films were determined from X-ray fluorescence spectra of the film excited by electrons. This was done by our collaboration group led by Paul Fons at AIST(Japan). Since the fluorescence is an element-sensitive method, the material of the substrate has to differ from the layer material. The thickness and the density of the GST film obtained from X-ray reflectivity together with the composition, gives absolute fluxes for the Ge, Sb and Te sources. The sticking coefficient is assumed to be unity. This fact was proven by the deposition of the GST on Si/SiO_2 at different temperatures monitoring the actual film growth rate ex situ by X-ray reflectivity. We found that the growth rate becomes constant for substrate temperature below 150 °C for both GaSb and Si wafers. Therefore, growing the composition reference samples at room temperature, we can be sure that the surface captures all the elements arriving at the surface.

We were able to amorphize and recrystallize intentionally large (0.25 mm^2) regions of epitaxially grown GST/GaSb films by a laser pulse. For this purpose, a Continuum Leopard SS-20-SV 60 ps Nd:YAG pulsed laser was used operating at 524 nm wavelength. The reflectance contrast was as high as 30% between the amorphized and recrystallized state. Electron backscattering diffraction (EBSD) from switched regions confirmed both, the switched amorphous and the recrystallized states of the film. These laser switching experiments were made by our colleagues Timur Flissikowski and Manfred Ramsteiner at the PDI.

4.4.1 Density and composition of GST films

Figure 4.16 shows a composition diagram of the samples grown on Si/SiO_2 wafers at room temperature. The points represent flux ratios of the Ge, Sb and Te sources. We see that flux ratios were close to GeTe-Sb_2Te_3 pseudobinary line to begin with and then rapidly approached the 2:2:5 stoichiometry. The growth behavior on GaSb(001) samples was basically the same for all these fluxes. In-plane map similar to Fig. 4.9 reveal the same dominance of the cubic and hexagonal in-plane symmetries for all stoichiometries, while weak additional reflections appear for samples strongly deviating from 2:2:5 stoichiometry. Due to their low intensity and disorder, so far we have not been able to identify additional phases, however all the observed reflections on in-plane and out-of-plane scans fit to the powder diffraction data of GST.

Figure 4.17 shows three ω-2θ X-ray reflectivity scans for GST samples grown on GaSb(001) at different temperatures. The curves which are shown represent typical reflectivity curves obtained from samples grown at these temperatures. The fitting curves, shown in red, were simulated using the PANalytical X'Pert Reflectivity software. The sample model which we used to fit the data were sandwich structures with the following sequence: a thick GaSb substrate, thin interfacial layer, main GST layer and finally a top surface layer with lower density and higher roughness. The interfacial and top layer thicknesses always were within of 1-3 nm, while the main GST layer

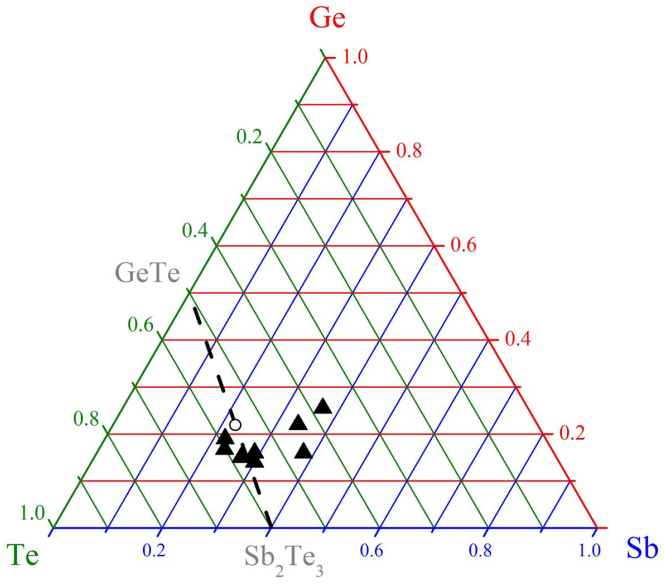

Figure 4.16: The composition of as-grown Ge:Sb:Te samples approaches 2:2:5 from sample to a sample.

thickness varied from 10 to 150 nm. The density, thickness and roughness values were the parameters acquired from the fits.

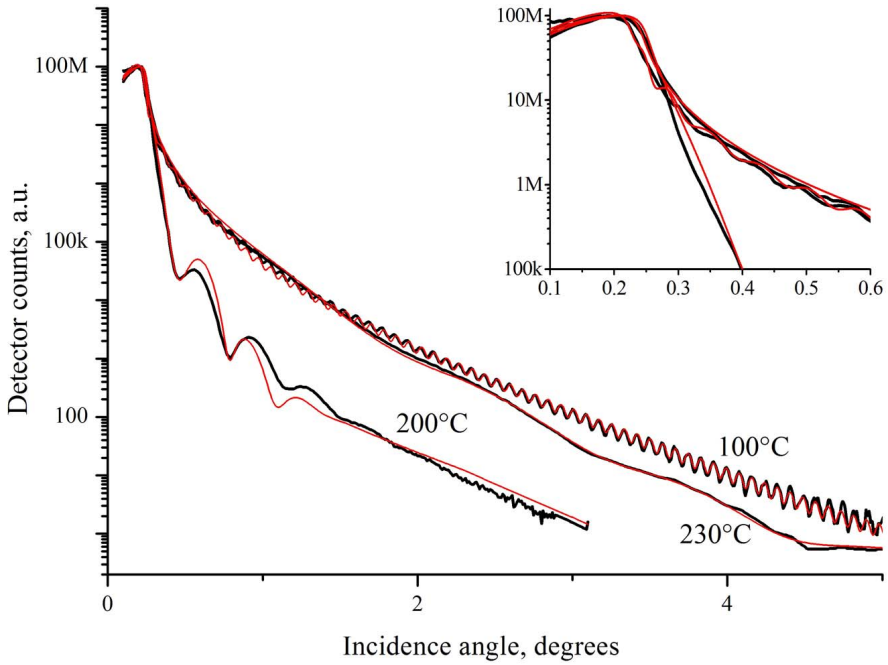

Figure 4.17: X-ray reflectivity plots for samples grown at different temperatures. The insert shows a closeup of the curves close to the critical angle. The red curves are simulated reflectivity curves.

For growth temperatures up to 100 °C we obtain an amorphous RHEED pattern and our layers are smooth (roughness less then 2 nm) but with a lower than average density. The density mostly affects the critical angle (total external reflection), shifting it to higher values for higher densities. The sticking coefficient for this temperature range is unity.

At temperatures in the range 180–210 °C where we have epitaxial growth, the roughness is always high, leading to the fastest decay of the reflectivity curve. This is due to the 3D growth we observe at these temperatures. The densities of the layers grown at 180–210 °C are much higher than average, but still lower than the ones expected for pure GeTe or GST with 20% vacancies (see Fig. 4.18). At these temperatures the material desorption is very noticeable and increases rapidly with temperature.

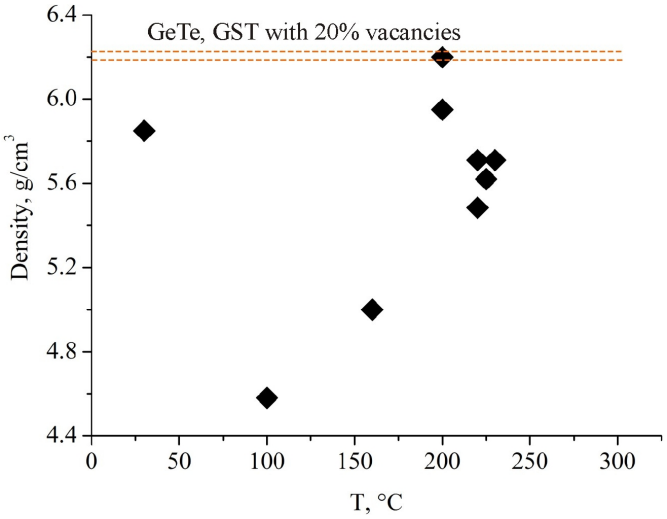

Figure 4.18: Sample density for films grown at various temperatures. The values were obtained from fits of X-ray reflectivity.

For samples grown at temperatures above 220 °C, the density of the layer reduces again, although the roughness goes down. The RHEED pattern for the samples grown at these temperatures looks more 2D, but the reflections are broader than for lower growth temperatures, indicating higher disorder in the film. The growth rates at these temperatures are only a few percent of the supplied material flux, thus we can not even guess the composition of these films. For this purpose, one needs to try epitaxy on wafers with different elemental composition than the layer and close enough lattice constants such as InAs. The composition then could be determined directly from epitaxial samples using X-ray fluorescence.

Looking on Fig. 4.18 we can conclude that the density of the GST films grown in the epitaxial region (T≈ 200 °C) is highest, but still lower than the one of GST with vacancies [82]. This means that all our films probably contain various amounts of voids, which make the material porous.

4.4.2 Laser induced switching

To induce amorphization of our epitaxial layers, we used a Continuum Leopard SS-20-SV 60 ps Nd:YAG pulsed laser system operating at a wavelength of 532 nm and with a repetition rate of 20 Hz. The single pulse duration was 60 ps with an energy varying around 60 mJ per pulse. We used epitaxially grown GST/GaSb(001) samples with 65 nm thick active layer thickness for the switching experiments. A scanning electron microscopy (SEM) image of a typical switched sample is shown at the bottom of Fig. 4.11. The samples were transported through atmosphere without any protection layer on the top.

The switching was monitored by measuring the reflectance of the switched region. For the reflectance measurement, a continuous Kr^+ laser with a triple Raman spectrometer was used in specular geometry. The switching region was intentionally large (around 0.2 mm) to simplify the switching study. The phases of the film were identified by electron backscattered diffraction (EBSD) measurements taken with spatial resolution at different regions.

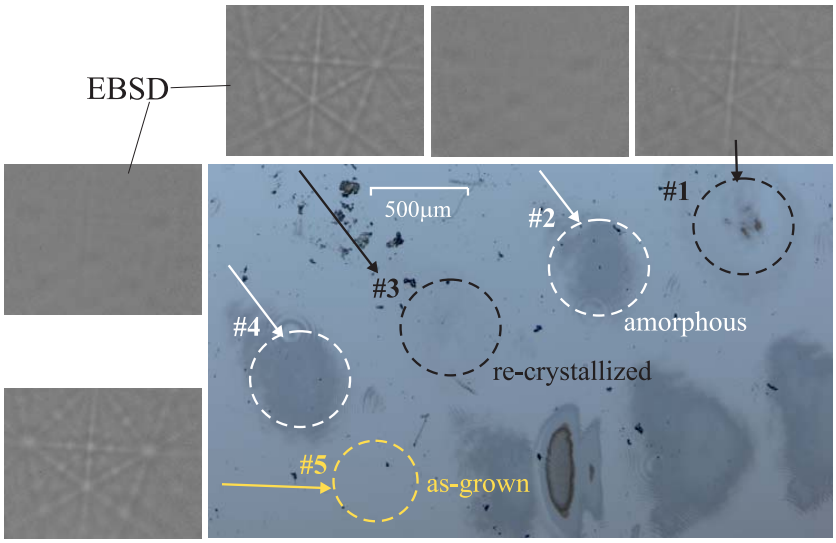

Figure 4.19: Optical microscope image of an epitaxial layer amorphized and recrystallized by laser pulses. Electron backscattering Kikuchi line patterns indicate the crystalline phase of the material. Recrystallization reproduces the initial orientation.

Figure 4.19 shows an optical microscope image of the regions where the laser pulses were applied. The circles indicate the amorphous and the recrystallized regions of the film. The corresponding EBSD patterns confirm the amorphous and recrystallized states of the film, featuring diffuse patterns for the amorphous regions and Kikuchi line patterns for the recrystallized regions. We also see that the recrystallized film restores the orientation it had before the amorphization.

Figure 4.20 shows the reflectance evolution depending on the number of pulses with different power density. We see that with a power density of 80 mJ/cm^2 per pulse, we can reach the minimum reflectance by a single pulse. Further pulses do not change the reflectance any more. Pulses at higher power density induce film degradation. Re-

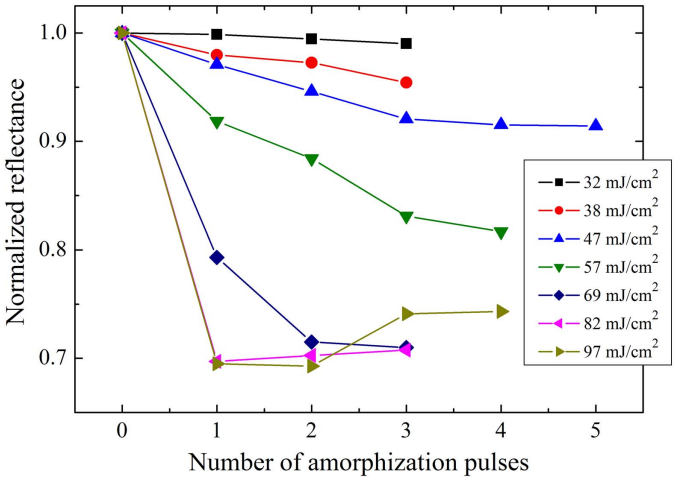

Figure 4.20: Film reflectance changes for different pulse energies. Data taken by Timur Flissikowski, PDI

crystallization of the film was achieved by multiple pulses with a power density below $30\,\mathrm{mJ/cm^2}$ per pulse. In this case, the laser acts as a heater annealing the region and inducing recrystallization.

These laser switching experiments, as well as resistivity measurements on as-grown and annealed samples verify that our epitaxial films show the expected phase change properties.

4.5 Growth rate and phase diagram

In this section, we investigate GST growth in detail and analyze the entire range of substrate temperatures for the growth of Ge-Sb-Te phase change alloys on GaSb(001) wafers. The experimentally determined growth rate curve has several important consequences which will be discussed. We start with general considerations. These are quite well known from thermodynamics and statistical physics [83], we just apply them to our specific case.

4.5.1 Sublimation rate of a solid or liquid in vacuum

Let us estimate the sublimation rate of a solid surface in vacuum. For simplicity we consider a single component system. We consider the equilibrium between the solid and the gas in a closed chamber. The volume density of molecules in the gas phase can be derived from the Mendeleev-Clapeyron relation:

$$n_s(T) = \frac{P_s(T)}{kT}, \tag{4.1}$$

where P_s is the experimentally determined saturated vapour pressure, k is the Boltzmann constant, and T is the temperature.

We consider a flat region S close to the surface (see Fig. 4.21). In equilibrium, the

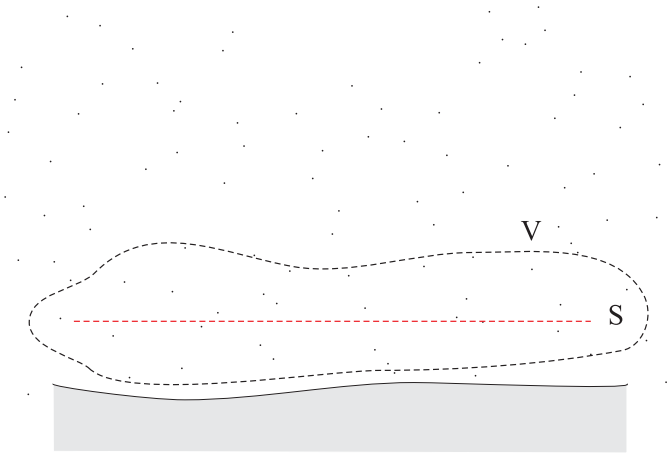

Figure 4.21: Schematic illustration of the surface in equilibrium with its vapor.

average number of molecules which cross the region S in both directions is equal by definition. In other words:

$$n_{out}\langle V_{out}\rangle = n_{in}\langle V_{in}\rangle, \tag{4.2}$$

where n_{in},$\langle V_{in}\rangle$ and n_{out},$\langle V_{out}\rangle$ are the volume densities and average normal velocities of incoming and leaving molecules, respectively. If the "temperature" of the incoming molecules is the same as the one of the outgoing molecules, the average speed of incoming and outgoing molecules is the same, and $n_{out} = n_{in}$. This is not the case if the incoming molecules are not from the vapor, but, for example, from a different source like an effusion cell. We consider this case later, however it will not affect the results significantly.

Molecules hitting the surface are either reflected or absorbed by it. This is quantified by the sticking coefficient α [84]:

$$n_{ref} = (1 - \alpha)n_{in} \tag{4.3}$$

where n_{ref} and n_{in} and are the volume densities of the reflected and incoming molecules, respectively. The outgoing flux, besides molecules which are reflected from the surface, contains molecules, which have sublimated (evaporated) from the surface,

$$n_{out} = n_{ref} + n_{sub}. \tag{4.4}$$

Therefore, the total volume density of molecules is the sum of the incoming, reflected and sublimated (evaporated) molecules:

$$n_s(T) = n_{in} + n_{ref} + n_{sub} \tag{4.5}$$

Combining the relations 4.1-4.5 for the volume density of sublimating molecules, we obtain:

$$n_{sub}(T) = \alpha(T)\frac{P_s(T)}{2kT} \tag{4.6}$$

where $\alpha(T)$ is the sticking coefficient depending on temperature. This is the equilibrium

case.

As soon as we remove the chamber walls (or start pumping), we remove the impinging and reflected fluxes. The desorbing flux remains and the surface starts to sublimate (evaporate) into vacuum. In the case of a large molecular mean free path compared to the sample size, the desorbed molecules will almost never scatter back. This implies the absence of convection on the lengthscales of the chamber size. It is easy to show that this conditions is typical for MBE. Now, for the desorption rate we can write:

$$\frac{\Delta N_{sub}}{\Delta t} = n_{sub} \cdot \langle v_{sub} \rangle, \tag{4.7}$$

where $\Delta N_{sub}/\Delta t$ is the desorption rate per unit area and n_{sub} and $\langle v_{sub} \rangle$ are the concentration and mean velocity of the sublimating molecules, respectively.

According to [83], the average speed of the sublimating molecules can be estimated from the average squared speed as

$$\langle v_{sub} \rangle \approx \sqrt{\frac{\langle v^2 \rangle}{3}}. \tag{4.8}$$

The average of the molecular squared speed $\langle v^2 \rangle$ is directly related to the temperature:

$$\langle v^2 \rangle = \frac{3kT}{m}, \tag{4.9}$$

where m is the molecular mass. The relations (4.14)-(4.9) together give the desorption rate:

$$\frac{\Delta N}{\Delta t} = \alpha(T) \frac{P_s(T)}{2\sqrt{mkT}}. \tag{4.10}$$

Therefore, the *saturated* vapour pressure of a material is a direct measure of its sublimation or evaporation rate. This vapour pressure is the one which is obtained from the experiment. For many materials, the values are tabulated [85]. For moderate temperatures, the sticking coefficient is of the order of one. The desorption rate of a solid (or liquid) follows the same Arrhenius law as the saturated vapor pressure.

We can calculate that, for example, a monolayer of silicon at 900 °C desorbs in a few hours, while a monolayer of germanium desorbs in a few minutes and monolayer of antimony requires only a few microseconds.

4.5.2 Thermodynamical conditions for growth and growth dynamics

It is well known that during the epitaxy of III-V materials the growth rate is determined only by the flux of one of the elements. The second element is always supplied in excess. Reversing the situation usually leads to droplet formation of the liquid or solid phase of the group III element [86]. The reason is that for group V elements the flux is low like if the material were in contact with unsaturated vapor. For the group III element, the flux is similar to the situation with a highly supersaturated vapour.

In the thermodynamics of vapour, the saturation S is defined as the ratio of the actual vapour pressure to the saturated vapour pressure. Analogously, we define saturation as the adsorbing-desorbing flux ratio. Let us evaluate this "effective" element saturation for pure elements under common MBE conditions.

Typical molecular fluxes at the surface can be obtained experimentally from RHEED or X-ray growth oscillations. Once we have determined the oscillation frequency ν, the molecular flux per unit area is of the order of

$$\frac{\Delta N_{in}}{\Delta t} \approx \nu / a^2, \tag{4.11}$$

where a is the in-plane lattice constant and N_{in} is the number of arriving molecules per area unit.

A droplet desorbs at a rate given by (4.10). Considering the incoming flux (4.11), for the saturation S we obtain:

$$S = \frac{2\nu\sqrt{mkT}}{P_s(T)a^2} \tag{4.12}$$

If the saturation $S > 1$, we have the supersaturated case and the solid (liquid) phase grows, if $S < 1$, then we have the non-saturated case and the solid (liquid) phase evaporates.

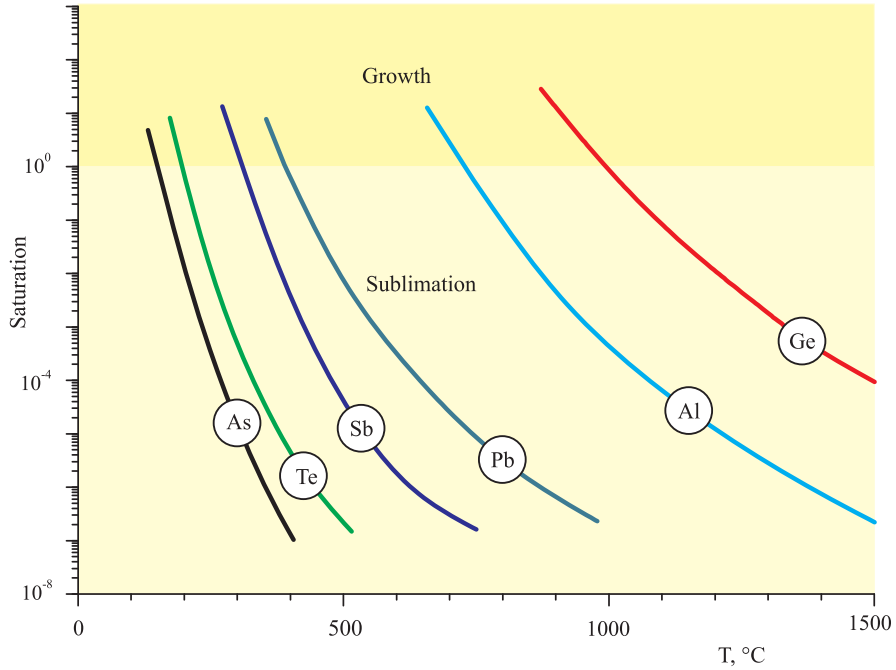

Figure 4.22: Effective saturation of various pure elements under typical MBE conditions

Figure (4.22) shows the saturation S versus temperature plotted for several typical III-V and IV-VI constituents. For a typical GaSb growth temperature of 450 °C and growth rate frequency $f = 0.1\,\mathrm{s}^{-1}$ we obtain $S = 10^6$ for Ga, and $S = 10^{-4}$ for Sb. Thus, pure Sb can not grow under these conditions, while for Ga it is possible. The situation is very similar for GaAs, PbTe, AlSb, AlAs and other binaries. It is always safe to supply one of the elements in excess at high enough temperature. The horizontal dashed line on Fig. (4.22) corresponding to $S = 1$ determines typical element desorption temperatures, which are 150 °C for As, 190 °C for Te, 310 °C for Sb, 390 °C for lead, 680 °C for Ga and 730 °C for Al. Of course, the values are not very precise due to several

rough approximations, nevertheless the sequence of the elements along the temperature axis should be correct.

4.5.3 Growth rate curve

Using the results of the previous two sections, we can estimate a growth rate curve versus temperature for the case of several elements impinging on the surface. We consider both limiting cases, when the elements fully phase separate on the surface and when they form a new chemical compound. This should help us to better understand our GST growth results.

First, we consider the real fluxes of the elements of interest, Ge, Sb_4 and Te_2. Let us derive the growth rate curve for the case of full phase separation on pure Ge, Sb and Te. In this model, grains or droplets of Ge, Sb and Te are forming and then interact with their fluxes. We want to find out at which temperatures these grains are growing, and at which they are sublimating for a given flux. We will show that for germanium, the desorption rate at moderate temperatures is insufficient to desorb the material. This is in conflict with the observed zero growth rate of GST at 300 °C. This indicates that germanium reacts with Te and/or Sb on the surface and forms a volatile compound.

During our derivation we want to produce relations containing only experimentally observable quantities and apply the results to our system.

We define the absolute growth rate as the growth rate normalized to the density:

$$u_{abs} = \frac{\rho}{\rho_{exp}} v, \tag{4.13}$$

where ρ is the actual layer density, ρ_{exp} is the expected layer density and v is the measured growth velocity normal to the surface. In general, the expected layer density does not need to be close to the actual layer density. On the other hand, for the actual density ρ we can expand its definition as:

$$\rho = \frac{M}{V} = \frac{\Delta N_{Ge} \cdot m_{Ge} + \Delta N_{Sb_4} \cdot m_{Sb_4} + \Delta N_{Te_2} \cdot m_{Te_2}}{Sv\Delta t}, \tag{4.14}$$

where M is the mass grown per time unit Δt, V is the newly grown volume and ΔN_{Ge}, ΔN_{Sb_4}, ΔN_{Te_2}, m_{Ge}, m_{Sb_4}, m_{Te_2} are the amounts of incorporated Ge, Sb_4 and Te_2 molecules, respectively, with corresponding masses, and S is the surface area. Combining 4.14 and 4.13 we obtain:

$$u_{abs} = \frac{\Delta N_{Ge}}{S\rho_{exp}\Delta t} \cdot m_{Ge} + \frac{\Delta N_{Sb_4}}{S\rho_{exp}\Delta t} \cdot m_{Sb_4} + \frac{\Delta N_{Te_2}}{S\rho_{exp}\Delta t} \cdot m_{Te_2} \tag{4.15}$$

The rate of incorporating material is the difference between incoming and desorbing fluxes:

$$\frac{\Delta N_i}{\Delta t} = \frac{\Delta N_i^{in}}{\Delta t} + \frac{\Delta N_i^{out}}{\Delta t}, i \in \{Ge, Sb_4, Te_2\} \tag{4.16}$$

The desorbing flux $\frac{\Delta N_i^{out}}{\Delta t}$ is determined by relation 4.10 for each element. The incoming flux $\frac{\Delta N_i^{in}}{\Delta t}$ can be determined experimentally from composition, density and thickness analysis of the films grown at low temperatures, when desorption is negligible.

Figure 4.23 shows a growth rate vs. growth temperature plot for constant Ge, Sb and

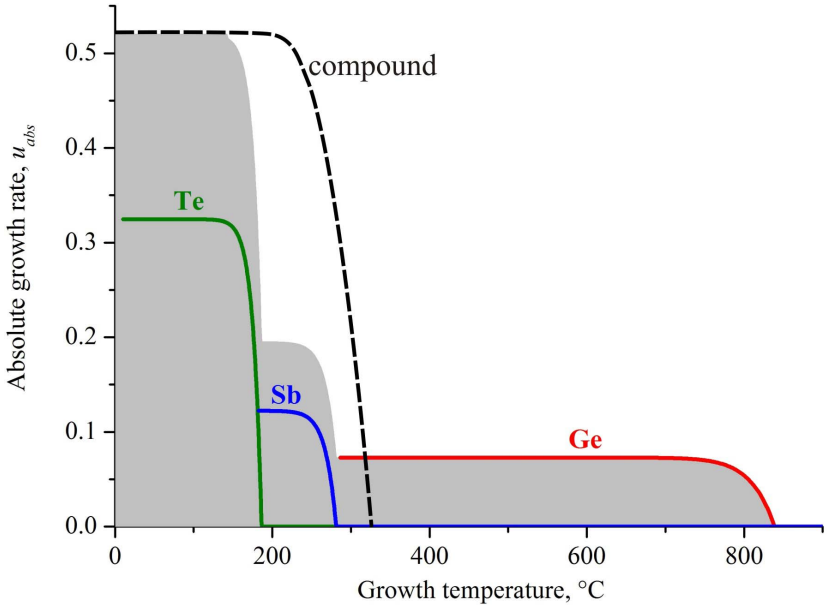

Figure 4.23: Calculation of the growth rate curves for Ge, Sb and Te in the case of no interaction between them. The fluxes were set to the 2:2:5 ratio and the absolute mass flux was normalized to the experimentally observed values

Te fluxes as red, blue and green curves, respectively. The fluxes are calibrated to the really observed growth rates and 2:2:5 stoichiometry.

In the simplest case when the elements do not form any compound and fully phase separate, a good approximation for the total growth rate is the sum of all three functions shown as the gray background. Thus, if we supply all three fluxes, we may loose all the tellurium molecules already at 190 °C, antimony at 290 °C and above 300 °C we can expect only germanium on the surface. This case is realized experimentally for GeSb growth.

The other limiting case is realized when the elements form a new chemical compound on the surface. Under chemical compound we understand a molecular crystal in which intramolecular bonds are strong and intermolecular bonds are weak. This is just a classification, where physical parameters which distinguish one class from another are the binding energy E and potential shape $1/r^n$. Breaking weak intermolecular bonds correspond to sublimation or evaporation of the material and is achieved by heating. Decomposition of the material may require much higher temperatures. Therefore, evaporation or sublimation of a compound material produces a gas of molecules, not of elements. Hydrocarbons are a typical example. Therefore, such a compound has its own vapour pressure curve, different from the curves of its constituent elements. Thus, for a compound we can use the same derivations we made for a single element. The result will look like the dashed curve shown on Fig. 4.23 in black. The precise shape of the curve is determined by material characteristics, like sublimation energy and pre-exponential factor.

4.5.4 Experimentally determined growth rate and the phase diagram

From our X-ray reflectivity data we have determined the absolute growth rate of our films at different temperatures. The plot is shown on figure 4.24. The growth rate is in nanometers per minute normalized to a density of 5 g/cm^3.

In addition, from our growth results we construct a phase diagram separating different growth regimes of Ge-Sb-Te phase change materials on GaSb(001) substrates (see Fig. 4.24). For growth temperatures below 130 °C, GST on GaSb(001) grows fully amorphous. In the temperature range 130–170 °C the film grows polycrystalline with randomly oriented crystal grains. The film becomes epitaxial for growth temperatures in the range 180–210 °C with initial amorphous layer formation. At substrate temperatures from 210 to 240 °C the initial layer orders only in the (1-10) direction. At these growth temperatures, significant desorption takes place, presumably leading to a loss of stoichiometry.

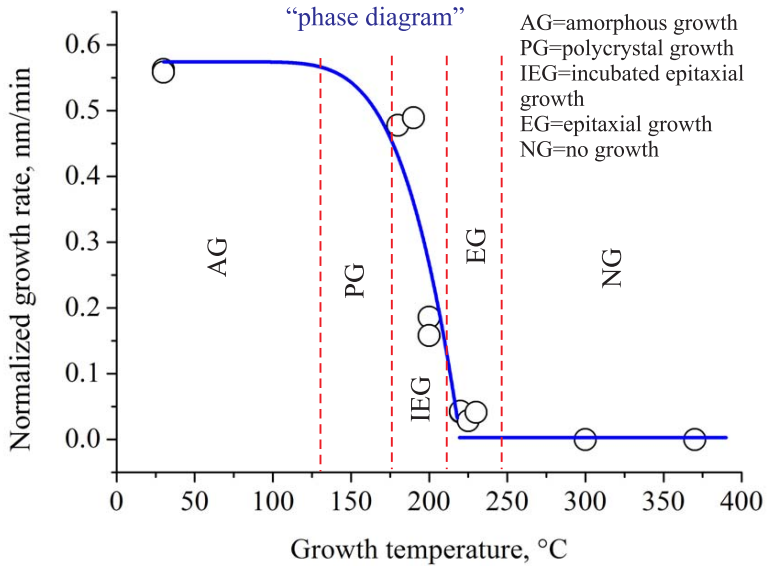

Figure 4.24: Phase diagram of the growth superimposed with the growth rate normalized to density. The diagram indicates several regimes: amorphous, polycrystalline, incubated epitaxial and direct epitaxial growth.

Astonishingly, for temperatures above 250 °C no growth is detected. Our empirical knowledge indicates that germanium should grow well at such low substrate temperatures. For example, for the growth of Ge/Si heterostructures, typical growth temperature are in the range 300-400 °C.

In order to elucidate the problem, we consider the thermodynamical aspects of the growth developed in the previous sections. The conclusion was that for our typical growth rates (fluxes) the desorption rate of an element becomes comparable with the impinging elemental flux at 190 °C for pure Te, at 280 °C for pure Sb and at 840 °C for pure germanium. To obtain these values, we took our absolute growth rate values and a 2:2:5 stoichiometry for the Sb, Ge and Te atoms, respectively. The growth rate functions (4.16) fore pure elements are plotted on Fig. 4.25. The gray background shows the sum

of the Ge, Sb and Te growth rate functions.

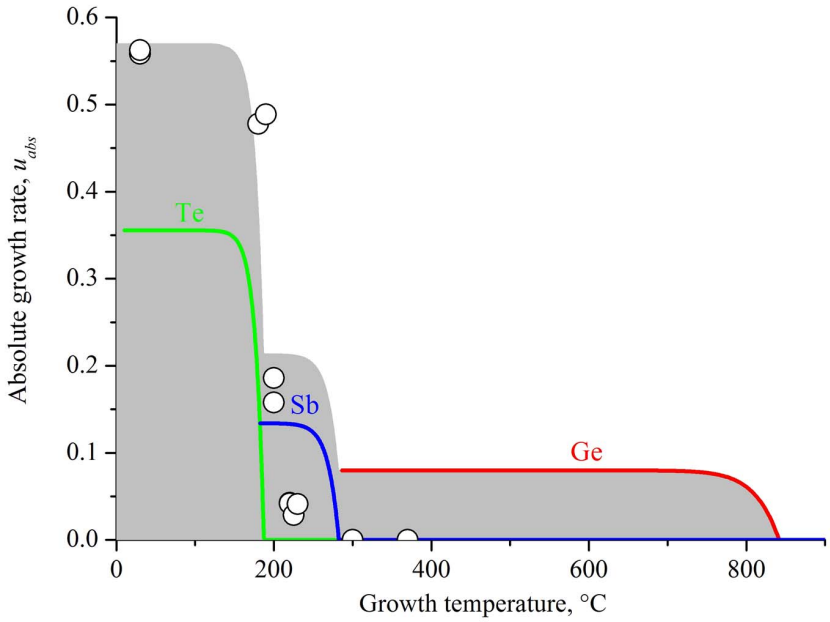

Figure 4.25: Experimentally observed growth rates compared to theoretical curves for pure Ge, Sb and Te. The results imply molecular evaporation of deposited material. The GST volatility is in between the ones for Te and Sb

The gray plot represents the case of Ge, Sb and Te atoms not reacting on the surface and fully phase separating. The actually observed experimental values are shown in Fig. 4.25 as white circles. We do not detect crystalline germanium on the surface even after hours of growth at temperatures above 250 °C, although we stay in the supersaturation regime for this element. As we mentioned in the previous sections, the pure Ge phase nucleates well in the absence of a Te flux. This means that Ge probably evaporates from the surface in molecular form together with Te. The phase which is responsible for the desorption of the Ge atoms has a vapor pressure comparable of that for Sb and Te as seen from Fig. 4.25.

5 X-ray diffraction studies of epitaxial Ge-Sb-Te alloys

As we know from the introduction, in convenient DVD-RAM the laser crystallized mark consist of polycrystalline GST in metastable cubic phase. The metastable GST possesses a NaCl-like structure with Te fully occupying one FCC sublattice and the other FCC sublattice consist of Ge and Sb. There are 20% of vacant sites in the Ge-Sb sublattice. This structure details were obtained from the analysis of the X-ray powder patterns produced by the laser-recrystallized region [36, 35, 20].

One of the aims of the current work is to demonstrate that we have prepared a single crystalline GST films in the metastable phase. The RHEED and X-ray studies of the films described in the previous chapter have shown, that our films predominantly possess FCC crystal lattice. However this description is not complete, since it does not clarifies several important moments, like: whether Te, Sb and Ge atoms are intermixed, do we have vacancies in the structure, how perfect is the crystallinity of the film, is the unit cell of GST distorted, etc.

Epitaxy is possible due to the strong thermodynamical driving forces which act to orient the film coherently with the substrate. If the umbrella flip mechanism holds (see 1.4) and we have really fabricated the metastable GST, then there is a chance to already have the amorphous building blocks oriented. According to [19], this building blocks are based on the tetrahedrally coordinated Ge atoms surrounded by Te. Due to epitaxial constraints this tetrahedral blocks then would have some long range order and will act as a crystal. It seems that this was observed by HRTEM even in sputtered GST [48, 49]. If one does careful analysis of the scattered X-ray intensity at the Bragg points, the atomic occupation of both tetrahedral and octahedral sublattices sites will be determined.

In this chapter we do this analysis by measuring and calculating the integrated intensities of the Bragg reflections. The vacancies concentration is also estimated. The crystal quality of the films will be discussed in the third section of this chapter, where the analysis of the X-ray peak widths is described. For all the analysis we used the samples grown at 200 °C in incubated epitaxial regime (see 4.5).

5.1 Film symmetry, orientation and lattice constants

Figure 5.1(a)-(c) shows a typical X-ray reciprocal space map of a GST film grown on GaSb(001) at 200 °C. For figures 5.1(a,c) the color scale is logarithmic, while for the figure 5.1(b) the color scale is linear. Thick solid lines indicate the dominant cubic phase of the film, since the intensities of the corresponding reflections are the highest. The HK0 in-plane mesh is similar to the one shown in Fig. 4.9 in the previous chapter. The only difference is the lower intensity of the hexagonal symmetry reflections, probably

due to a better stoichiometry. The out-of-plane maps 5.1(b)-(c) were obtained from a different sample then the one used for the map 5.1(a).

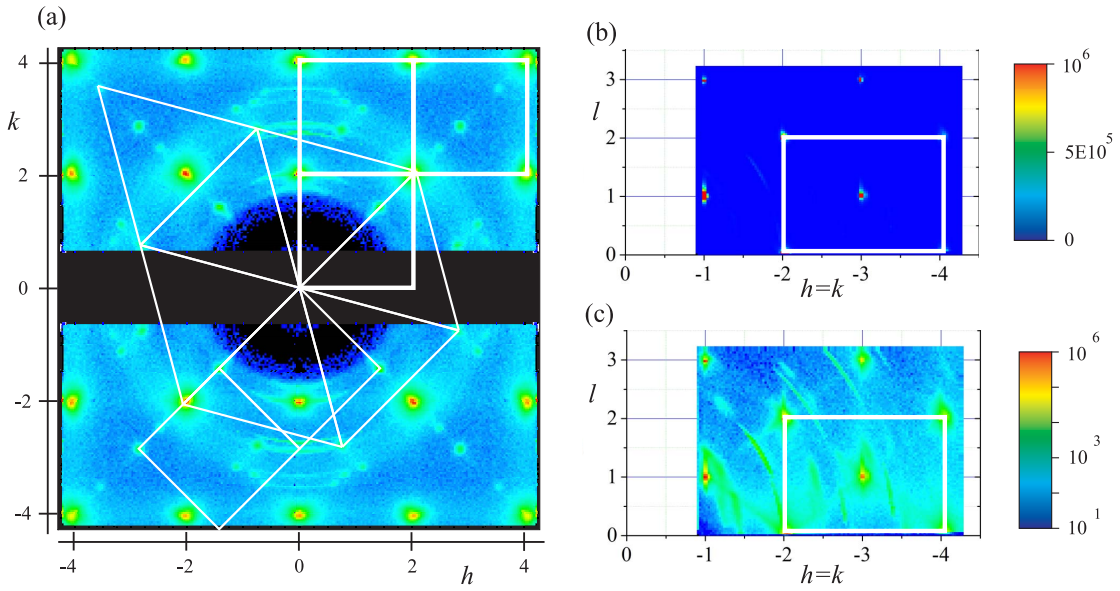

Figure 5.1: (a) Reciprocal space map for the $(h, k, 0)$ plane of a GST film. The white solid lines show the in-plane symmetries of the epitaxial phases. The color represents logarithmic intensity. (b) Out-of-plane h=k X-ray map. The intensity scale is linear. (c) The same map as (b) but plotted using the same logarithmic scale as (a) to see additional features.

All observed reflections on all samples agree very well with the X-ray diffraction powder data for GeTe-Sb_2Te_3 alloys. Some of the weak reflections match only the interplanar distances of hexagonal phases of Ge-Sb-Te alloys. The intensity of the weak polycrystal rings were lower for samples grown at higher temperatures, and were almost absent for samples grown above 200 °C.

Therefore, reciprocal space mesh scans reveal a strongly dominant cube-on-cube epitaxially oriented FCC cubic phase in the film. Small amounts of differently oriented cubic phase and different phases seem also to grow in the film, depending on the alloy composition.

5.2 Octahedral and tetrahedral site occupation in the epitaxial cubic phase

The body centered cubic (BCC) structure of the RHEED and X-ray reflections (see Fig 4.6 and 4.9) can be imagined as a primitive Bravais lattice with three primitive translation vectors. These basis vectors can be reciprocated constructing the real space lattice. As is well known [87], the result will be the face centered cubic (FCC) Bravais lattice. From the distance between reflections we obtain the elemental unit cell of this FCC lattice with a lattice constant of 6.02 Å. The symmetry of the crystal is Fm-3m. A rhombohedral distortion of the GST unit cell is evident from the reflection shapes, and

will be discussed later.

As we know from the introduction, there is quite a wide composition range where GeTe-Sb_2Te_3 pseudobinaries could form a cubic phase. In our epitaxial films we find an atomic arrangement such that the average crystal lattice possesses an Fm-3m symmetry. A larger unit cell, such as the proposed spinel structure for the quasi-amorphous state of 124-GST [88], would immediately lead to the appearance of additional (h,k,l even and odd mixed) reflections in reciprocal space. If there were a pronounced alloy ordering in the sublattices on a longer range scale, fractional order reflections would be visible. Thus, an ordered spinel lattice structure for our crystalline phase does not fit.

Nevertheless, there is still a chance to have tetrahedrally coordinated atoms in the structure, distributed, for example, as in the zinc blende structure, or disordered spinel structure. By disorder, here, we mean the Sb, Ge and Te atom replacements, while the FCC lattice itself is preserved. As long as the overall FCC symmetry is preserved, no additional reflections will be produced.

Tetrahedral coordination of Ge atoms has been repeatedly observed in sputtered amorphous 225-GST films as a part of rigid building blocks [19, 48, 49]. We can identify the presence of tetrahedrally coordinated atoms by careful analysis of the reflection structure factors. Furthermore, we can determine the occupation of each sublattice site by the different atoms. In this section we describe this analysis.

Normally, the absolute intensity scale is not used in structural studies due to the complexities involved in its experimental determination. The result is the loss of information such as the total amount of material (in grams) participating in the scattering process. This information is often obtained indirectly by other methods under the assumption that all the material is staying in this single crystalline phase. This is probably not the case for us, however the determination of an absolute intensity scale would not be reliable due to the complicated grazing incidence geometry especially optimized for surface diffraction experiments. Therefore, how much of the material is in crystalline form, and how much is in amorphous form remains an open question.

5.2.1 Structural model and fitting parameters

Several studies [89, 20, 35, 90, 36, 37] find that the structure of cubic Ge-Sb-Te is distorted NaCl, with the Ge, Sb atoms and various amounts of vacancies randomly occupying one of FCC sublattices, while the other sublattice is Te. We adopt this model and in addition allow the atoms to occupy tetrahedrally coordinated positions. As we have already mentioned, these atoms should be distributed according to the Fm-3m symmetry (or FCC lattice with a certain basis).

The last assumption we use is the full occupation of the second FCC sublattice in the NaCl structure by Te atoms. This assumption is based on reported structures of GeTe-Sb_2Te_3 pseudobinaries.

Figure 5.2 shows the unit cell of our model crystal. The crystal has an FCC Bravais lattice with tellurium atoms at (0,0,0) and an FCC lattice with Ge, Sb or vacancy at (1/2,0,0). In addition, germanium may sit at a tetrahedral sites. These sites are represented by two FCC lattices at (1/4,1/4,1/4) and (1/4,1/4,-1/4). The crystal could be imagined as three FCC sublattices shifted from the reference FCC tellurium sublattice by the corresponding vectors. The four colors in Fig. 5.2 show each FCC sublattice. The three sublattices are occupied by Ge, Sb or vacancies. We repeat here once again,

n	x_n	y_n	z_n	w_n^{Ge}	w_n^{Sb}	w_n^{Te}
0	0	0	0	0	0	1
1	1/2	0	0	w_1^{Ge}	w_1^{Sb}	0
2	1/4	1/4	1/4	w_2^{Ge}	0	0
3	1/4	-1/4	1/4	w_3^{Ge}	0	0

Table 5.1: Fitting parameters and sublattice coordinates

that each sublattice may incorporate any other type of atom, but they do not order on long range scales due to the observed FCC symmetry. The other limiting case would be if each of the sublattices were occupied only by atoms of a certain type.

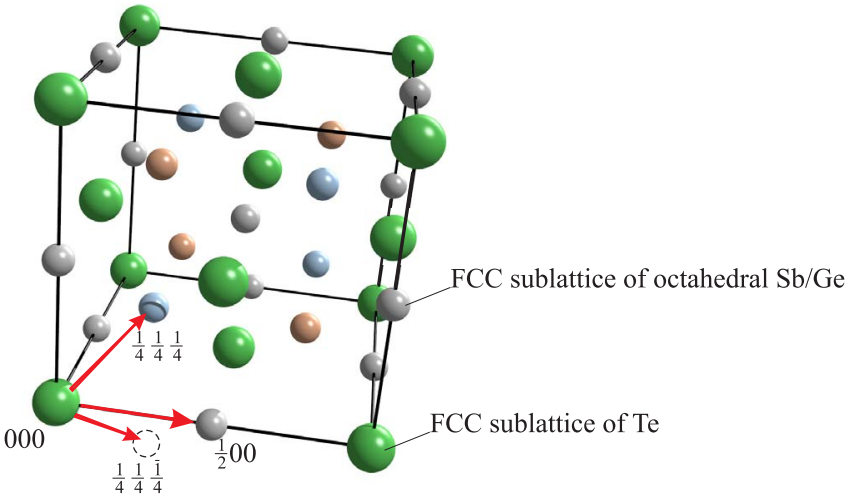

Figure 5.2: Model of a FCC crystal with one FCC sublattice fully occupied by Te and another is randomly occupied by Ge, Sb or a vacancy. Two additional FCC sublattice shaded in red and blue indicate possible tetrahedrally-coordinated positions of Ge atoms.

With these assumptions, the structure factor of a Bragg reflection becomes:

$$F_{hkl} = 4 \cdot \sum_{n=0}^{3} f_n e^{-M_{nq}} e^{2\pi i(hx_n+ky_n+lz_n)} \tag{5.1}$$

where $e^{-M_{nq}}$ is the Debye-Waller factor, h,k,l are Miller indices and x_n,y_n,z_n are the atomic coordinates within the unit cell. The summation runs over all four sublattices. The atomic scattering factor f_n is expressed in terms of the atomic scattering factors of Te, Sb and Ge atoms:

$$f_n = w_n^{Ge} f_{Ge} + w_n^{Sb} f_{Sb} + w_n^{Te} f_{Te} \tag{5.2}$$

where w_n^j is the probability to have an atom of type j in the n^{th} sublattice. The coefficients w_n^j are the fitting parameters listed in table 5.1. Assuming that one FCC sublattice is fully occupied by Te atoms, the number of fitting parameters is reduced to

four. This assumption may not be needed, if a bigger number of reflections is measured. We use 20 different reflections.

The absolute intensity scale is the fifth fitting parameter. This parameter, actually, could be used to estimate the amount of material participating in the scattering process, or the fraction of epitaxially oriented film. This was not attempted here, since the experimental realization is difficult and would probably produce unreliable results. So, we retain it as a fitting parameter.

Least squares fitting was used to find the best set of the five parameters Scale, w_1^{Ge}, w_1^{Sb}, w_2^{Ge} and w_3^{Ge}. For the fitting, we construct the function of five variables S(Scale,w_1^{Ge},w_1^{Sb},w_2^{Ge},w_3^{Ge}):

$$S = \sum_{hkl} (F_{cal}^2 \cdot Scale - F_{exp}^2)^2 \tag{5.3}$$

where the summation runs over approximately 20 experimentally measured reflections for each sample. The function S is then minimized.

We have measured three samples grown under the same conditions which demonstrate basically the same fitting results.

5.2.2 Fitting results

Figure 5.3 shows typical peak shapes of different (h, k, l) reflections obtained from the film grown in the incubated epitaxial regime (see previous chapter for the explanation). The solid lines show Gaussian fits to the experimental points. The sharp contributions from the substrate were excluded.

We can clearly see that the Gaussian fits are reasonably good, and we can use equation 2.39 for determination of the structure factor squared $F_{hkl}F_{hkl}^*$. According to this equation, for each (h,k,l)-reflection we should apply three correction factors: polarization correction, linear gamma table correction and area correction. The results show, that after applying the corrections, the experimentally obtained structure factors $F_{hkl}F_{hkl}^*$ of the (133)-type and (331)-type reflections are close in magnitude. Since the geometry of the experiment is different for these equivalent reflections, this proves that we made all our geometry corrections right. A small systematic factor $\cos(\gamma)$ remains which we introduced to improve the fit, however it does not change any conclusions. The source of this systematic error can be understood, since the area correction was calculated using a parallel projection with equal $4{\times}4\,\mathrm{mm}^2$ detector and front slits (see 2.3.3 and 2.3.4 for the details).

The experimentally determined structure factors of different reflections are shown in Fig. 5.4(a) as spheres with diameters proportional to the structure factor $(F_{hkl}F_{hkl}^*)^{\frac{1}{2}}$. Figure 5.4(b) shows calculated structure factors using the parameters from table 5.2. This table is obtained after least squares fitting. Figure 5.4(c) shows measured and fitted structure factors for various reflections. The histogram is sorted by reflection type: fundamental (h, k, l all even) or superstructure (h, k, l all odd).

The minimization of the function 5.3 yields the values for the parameters w_1^{Ge},w_1^{Sb},w_2^{Ge} and w_3^{Ge} listed in tables 5.2 and 5.3 for two different samples.

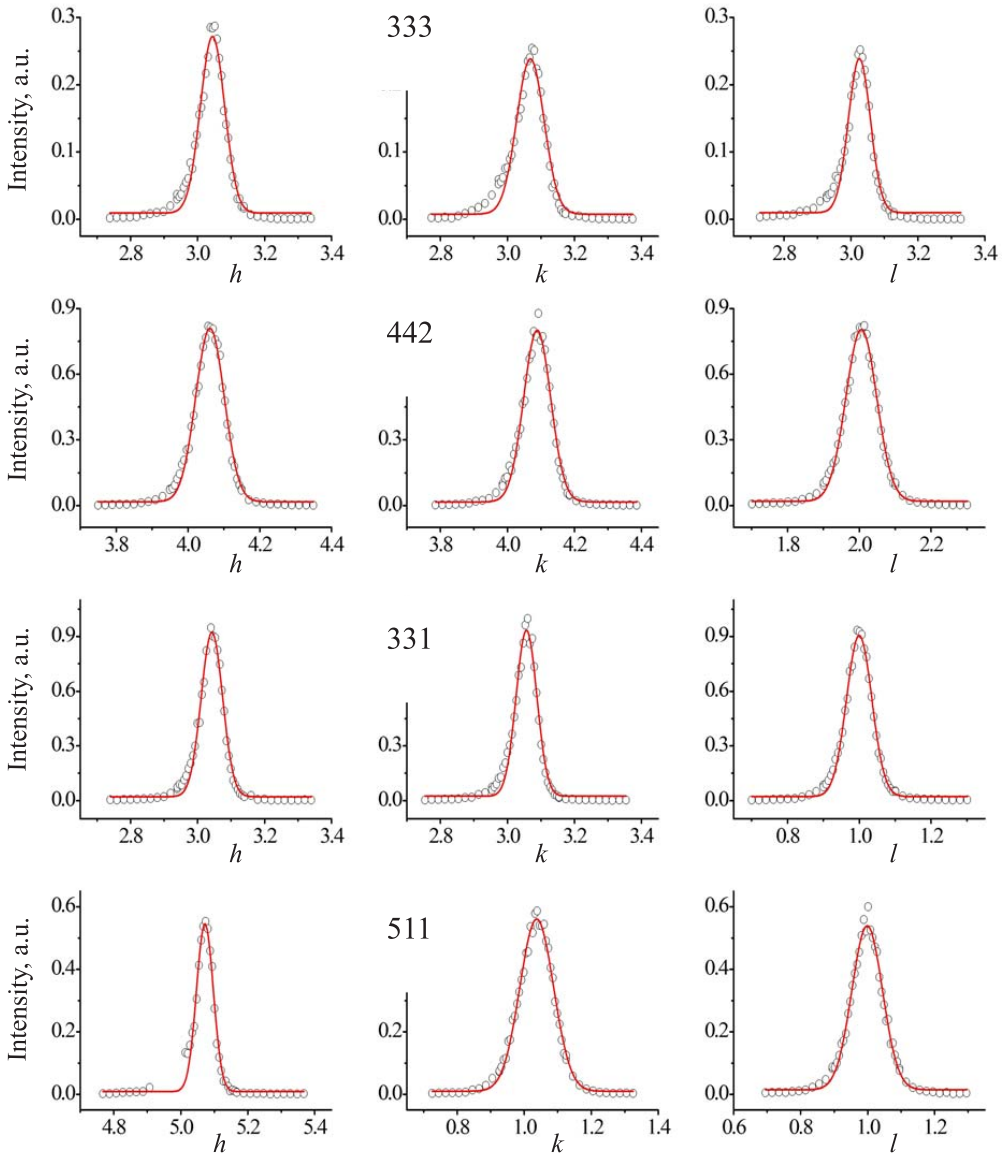

Figure 5.3: X-ray (h, k, l) scans for four different reflections. The red curves are Gaussian fits to the experimental points

The statistical error of the fit σ was calculated from the equation:

$$\sigma = \frac{1}{N} \sum_{N} \| \frac{F_{cal}^2 \cdot Scale - F_{exp}^2}{F_{exp}^2} \| \cdot 100\% \tag{5.4}$$

where N is the number of measured reflections.

If we do not set any requirements on the Ge, Sb and Te stoichiometry, the fitting results give the GeTe structure, where one FCC sublattice is fully occupied by the Te and another FCC sublattice is fully occupied by Ge. If we force the number of Ge and

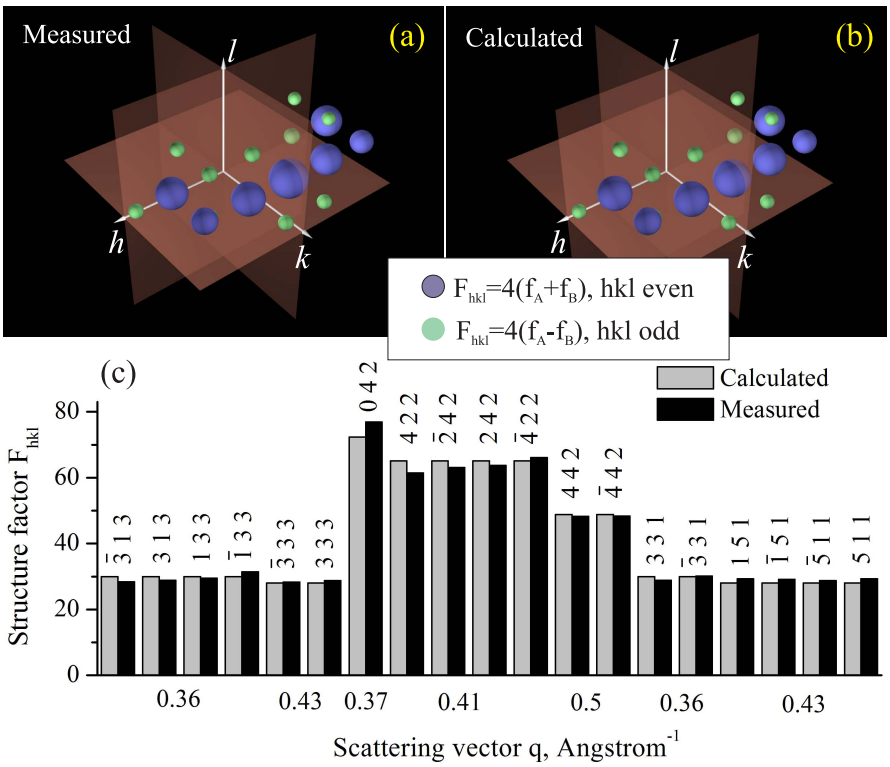

Figure 5.4: Experimentally determined and simulated structure factors: (a) spheres at corresponding (h, k, l) points of reciprocal space with diameters proportional to the experimentally determined structure factors. (b) Calculated structure factors. (c) Calculated and experimentally determined structure factors collected in a one-dimensional histogram. In the histogram, the structure factors are sorted according to (h, k, l) odd-even-odd, grouping fundamental and superstructure refections together.

Sb atoms to be equal, the fitting results demonstrate that the Ge-Sb sublattice is not completely filled by Ge and Sb atoms. There are about 20% of vacant sites in this sublattice, as expected for metastable GST.

Figure 5.5 shows the unit cells of the fit structures for the cases of restricted and unrestricted compositions. What we see is that tetrahedral sublattices are never filled. This indicates that we have a GeTe-like structure, as expected for GST, with vacancies in the Ge-Sb sublattice yielding an average electron density of 32 to 33 per site. If we input 20% of vacancies, as reported in the literature, we are getting the same electron density in the Ge sublattice as for GeTe. From this point of view, therefore, the GeTe and GST structures are indistinguishable. To prove that our antimony is sitting in the Ge sublattice, we should either be able to prove full crystallization of the film, so that no amorphous inclusions are present in the film or do an energy-dispersive experiment at the Sb edge to see if sublattice- sensitive reflections are simultaneously sensitive to the Sb edge.

The fact that we do not observe pure Ge, Sb or Te reflections from the film indicates the absence of significant phase separation into the pure elements. However, there is

Sample	w_1^{Ge}	w_1^{Sb}	w_2^{Ge}	w_3^{Ge}	σ
s2_0137	1.06	0	0	0	6.15%
s2_0129	0.9719	0.05	0.04	0	11.08%

Table 5.2: Fitting parameters. The composition is not restricted.

Sample	w_1^{Ge}	w_1^{Sb}	w_2^{Ge}	w_3^{Ge}	σ
s2_0137	0.4	0.4	0	0	7.55%
s2_0129	0.38	0.38	0	0	13.0%

Table 5.3: Fitting parameters. The composition is restricted to a Ge:Sb ratio of 1:1

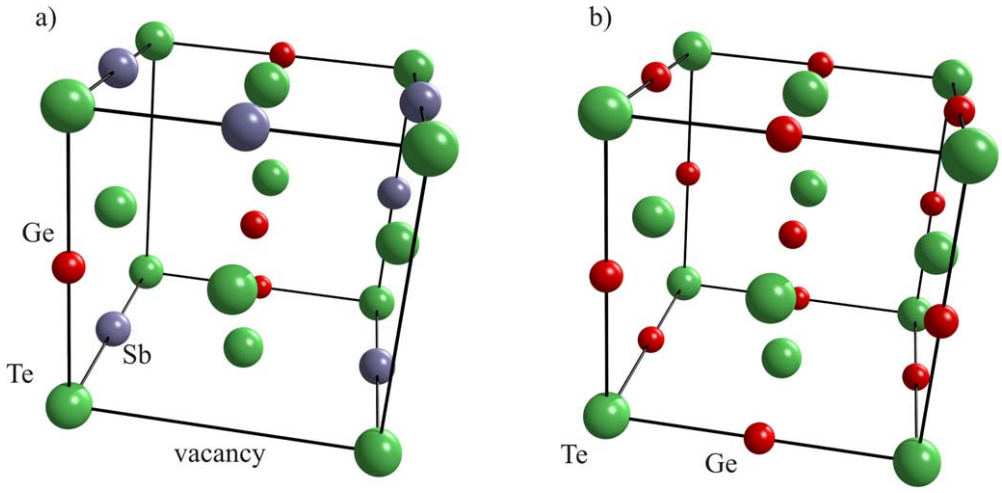

Figure 5.5: The results of the fit give NaCl like structures: (a) for the restricted Ge:Sb ratio of 1:1 the structure is cubic $Ge_2Sb_2Te_5$ with 20% of vacancies, (b) without restrictions the structure is GeTe.

still a chance to have them in the amorphous state, since the growth temperatures are not very high. To resolve this uncertainty, one would need to anneal the films and repeat the X-ray mesh scans to seek for pure Sb, Ge and Te, however, as we know, the film completely desorbs and decomposes above 220 °C. One would therefore need to cap these layers before annealing.

Another thing we should think about is the possibility of the film to decompose into pure GeTe and Sb_2Te_3 binaries. The X-ray in-plane mesh then would satisfy the observed cubic GeTe and hexagonal Sb_2Te_3 symmetries. However, antimony telluride has a long stacking period along the c-axis, thus the 001 reflections would be visible. However, we do not observe these reflections in our l scans.

To gain a feeling for the accuracy of our structure analysis, we take a closer look at our measured and calculated structure factors. The structure factors, as we already mentioned, are shown on Fig. 5.4(a) and (b) for the measured and calculated cases, respectively. Green and blue colors emphasize that we have only two types of reflections in reciprocal space with intensity proportional to the square of the sum and the difference of atomic scattering factors. From crystallography we know that the number

System	Ge	Sb	Te	Source
GeTe	0.6738	-	0.3834	Calculated [91]
$Ge_2Sb_2Te_5$	3.55	3.55	1.2	[89, 35, 90, 36]
$GeSb_2Te_4$	0.7520	0.4485	0.4279	Calculated [91]

Table 5.4: Debye-Waller factors for GST and GeTe

of superstructure reflections is equal to the number of sublattices minus one. The larger the difference of these two structure factors, the closer the electron density in the GeSb sublattice to that of Te. At the ultimate limit of equal electron densities, the structure reduces to simple cubic, which leads to vanishing (111)-type superstructure reflections. Therefore, the reciprocal lattice also reduces to simple cubic. If there were a contribution from a third sublattice, the selection rules would be different. For our case, this could be tetrahedrally coordinated Ge atoms. As is well known [51], the tetrahedrally coordinated sublattice in FCC crystals produces an additional selection rule for even order reflections: $h+k+l=2+4n$. Thus, due to destructive interference, the reflections of 042 type would be much weaker than the reflections of 242 type, which was not observed.

5.2.3 The role of Debye-Waller factors

In this section we would like to discuss a problem which can be very important specifically for structural studies of phase change materials. The problem is which Debye-Waller factor to choose for each of the atoms in our calculations.

We have an insufficient number of reflections to fit Debye-Waller factors. Therefore, we have used the values published in previous papers about the structure of Ge-Sb-Te phase change materials [89, 90, 20, 35, 36, 37]. There, the Debye-Waller factors are used as one of the fitting parameters. It was found that the Debye-Waller factors were twice as high for the Ge-Sb sublattice than for the Te sublattice in metastable GST and GeTe, and were in general quite big. However, the same Debye-Waller factors for both Ge and Sb were used, while one can expect that Ge atoms should have higher values of thermal displacement in the lattice than Sb, since they are significantly lighter. The Ge and Sb atoms are believed to be randomly distributed in the sublattice and, therefore should be on equivalent sites on average. This is supported by another group calculating the Debye-Waller factors for stoichiometric Ge Sb_2 Te_4 on the basis of their theory [91]. The Debye-Waller factor was high only for the Ge atoms compared to Sb and Te, but not for the whole sublattice, while in general having quite small numbers. Table 5.4 collects the Debye-Waller factors for our system reported in the literature.

The Debye-Waller factors are temperature dependent. Our measurements are done at room temperature, thus the presented Debye-Waller factors are for room temperature. The importance of these factors is obvious: they scale the atomic scattering factors selectively for each atom according to equation 2.22. Therefore the occupancy of the sublattice by Ge, Sb and vacancies is drastically affected. However, the presence of vacancies in the Ge sublattice is very important for ultra fast switching [92]. Therefore, a good knowledge of the Debye-Waller factor is crucial and requires careful investigation.

An explanation for the difference between the experimental and calculated Debye-

Waller factors (see table 5.4) are the static displacements in the Ge-Sb sublattice. It is well known that GeTe (a prototype of cubic GST), besides a rhombohedral distortion has a buckled lattice [32], so that Ge and also Te are not at perfect lattice site positions. As mentioned by Kolobov et al. [19], the large Debye-Waller factor is due to static displacements created by the presence of longer and shorter bonds. However, it seems strange that this static Debye-Waller factor is reported to increase with temperature [89].

We think that for GST there is, probably, a large static (non-thermal) contribution to the Debye-Waller factors. Calculations, however, provide only thermal Debye-Waller factors. Therefore, leaving the Debye-Waller factor as one of the fitting parameters seems most suitable to study the structure of GST.

5.3 Broadening of the X-ray peaks

We observe non-trivial peak shapes in reciprocal space depending on crystallographic direction and scattering vector length. In addition, the intense central part of each peak is approximated well by a Gaussian function, while the broad parts of a reflection behave differently.

In a real crystal, many reasons may lead to X-ray peak broadening. Some of those which should exist in our films will be discussed below. However, none of them reproduces all the features observed in the experiment, either predicting too small broadening or a different peak shape. Therefore, we conclude that our broadening is due to the rhombohedral distortion of the cubic unit cell, epitaxially aligned on the cubic substrate. The details will be discussed below.

First, we discuss the question where to cut the integration of a very broad reflection when obtaining the integrated intensity.

5.3.1 Integrated intensities from broad reflections

In the previous section, where integrated intensities were calculated, the Bragg peaks were fitted by Gaussian functions (see Fig. 5.3). The shoulders of the reflections had orders of magnitude lower intensities and were attributed to the background. We assumed that the intensity decays fast enough to have a negligible contribution to the integrated intensity. Obviously, the integral of a background (integral of a constant) does not converge. The background, due to the nature of incoherent scattering, is not present in the integrated intensity (2.21). Therefore, after background subtraction the experimental data is fitted by a pure Gaussian which has a limited area.

Coherent scattering may produce a peak which does not decay as fast as Gaussian. If its integral does not converge, integration over a limited volume may have different meaning. Moreover, even if the integral only slowly converges, if during integration the dominant intensity is not collected before the contribution from the next peak appears, an error is introduced in the result.

Figure 5.6(a,b) shows an ω scan through the (020) Bragg reflection in linear and logarithmic scales, respectively. Red curves in both plots are Gaussian fits to the experimental points. The blue curves are Lorentzian fits to the logarithm of the intensity, which will be discussed later. On the logarithmic scale we clearly see that the Gaussian fit is bad for $|\Delta\omega|>2$ degrees, while the intensity is still not at background level. The

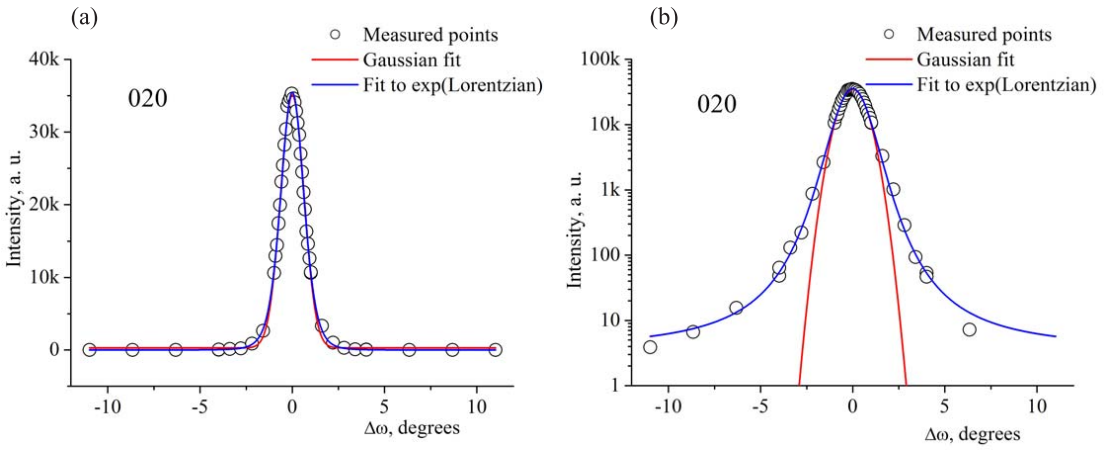

Figure 5.6: Bragg reflection on linear (a) and logarithmic (b) scales. The red curves are Gaussian fits to the experimental points. The blue curves are Lorentz fits to the logarithm of the intensity.

shoulders that are not well approximated by the Gaussian function seem to produce a 3D cloud in reciprocal space (see, for example, the mesh scan in Fig. (5.1(a)). If they are due to coherent scattering, they should contribute to the structure factor and the area under the Gaussian fits is insufficient. Since the integration in 3D space in spherical coordinates is proportional to $\int_0^{\Delta q_2} I(Q+\Delta q) 4\pi \Delta q^2 d\Delta q$, we plot $I(\Delta\omega)\Delta\omega^2$. This function is shown in Fig. 5.7(a) for the experimental black curve and for the red Gaussian fit. The difference in area below the corresponding curves represents the fitting error in terms of integrated intensities. For the present case the error may be as high as 40 %.

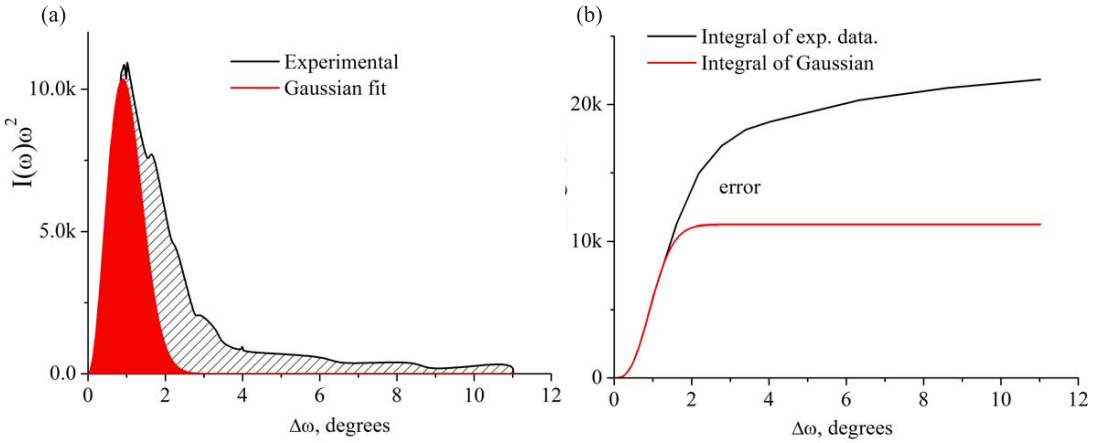

Figure 5.7: (a) $I(\omega)\Delta\omega^2$ function for the Gaussian fit (red) and the experimental data (black). (b) The 3D integrated intensity with distance from the peak center for Gaussian fit (red) and the measured data (black).

This does not necessarily mean that we incorrectly determine our structure. Since we are interested in relative structure factors, we just need to confirm that all measured reflections possess the same characteristic line shape.

There seems to be no general answer to the problem what contributes to integrated intensities for highly imperfect crystals. Should broad tails of Bragg reflections be included or subtracted from the integration? To obtain the structure factor of a Bragg reflection, one needs to integrate the peak intensity. This integrated intensity concept is based on the assumption that the integral of the Bragg reflection decays fast and converges. If the fitting function is unknown, the concept may not be used properly. Practically, Gaussian or Voight fitting functions are used, which have limited areas. These functions are theoretically predicted for crystals with many types of imperfections (see below).

5.3.2 Experimentally observed broadening effects and broadening anisotropy

A peak is generally broadened by two contributions: instrumental and physical. Instrumental broadening is due to the properties of the X-ray beam and diffractometer. Physical broadening is due to crystal imperfections. If the profile functions for the instrumental and physical broadening are known, the effects can be separated.

For the physical broadening, in the most general case the reflection profile is determined by the correlation function of the atomic positions. In diffraction it is commonly assumed that the correlation function consists of two terms, one describing size effects and one describing strain effects. It is well established that the size term produces Lorentzian profiles (exponential correlation function), while strain alone produces Gaussian profiles (Gaussian correlation function). Therefore, peak profiles are normally fitted by Voight functions, which are a convolution of the above two [93, 94, 95, 96, 97, 98, 99].

However, for our case Gaussian and Voight functions approximate well only the central parts of the reflections. Long reflection tails cannot be fitted by these functions, as demonstrated in Fig. 5.6. To fit these reflection tails properly, one needs to know the strain fields produced by all defects in the crystal.

For various types of defects proper peak profiles were calculated by Krivoglaz et. al [59]. He separates all defects into two categories: defects which produce peak broadening and others which don't. Point defects, such as substitutional or interstitial atoms, vacancies or nuclei of different phases are defects which do not produce peak broadening. In kinematical theory this means that an infinite crystal with point defects would possess Bragg reflections with a FWHM equal to zero. Characteristic features of point defects are long reflection tails following a power law [100, 101, 102, 103]. Defects of higher dimensions like misfit or threading dislocations, antiphase domains or grains produce peak broadening. This means that defects of this type produce a limited FWHM of the Bragg peak. However, similar to the diffraction from point defects, diffraction from dislocations also contains long tails following a universal power law [104, 105]. As we will see we have both in our Ge-Sb-Te alloys, quite strong peak broadening and long low-intensity tails. The central parts of the reflections were analyzed and the possible reasons will be discussed below. Fitting of the long low-intensity tails, however, requires further investigation.

As we have seen, our films contain enormous amounts of vacancies which may act as a point defects. We therefore expect to see their characteristic diffraction features (tails). Since our Ge-Sb-Te films are relaxed, they should also have misfit dislocations. Thus one need to estimate broadening due to dislocations. However, in our case the strain

fields from the dislocations are complicated, since the cubic unit cell of GST besides the 1% lattice mismatch has a rhombohedral distortion.

The problem can also be tackled from a different angle. We find that the logarithm of the peak intensities can be fitted by a Lorentzian. Moreover, this function approximates well the whole peak profile, including the central regions and the diffuse tails. Despite that there is no physical motivation for choosing such a fitting function for the entire curve, nevertheless some insight can be gained. For example, in the central part this function is Gaussian, implying a strain-induced source of broadening, while for larger scattering vectors the function obeys a power law, which implies strong distortions in the vicinity of defects.

Figure 5.8(a),(b) shows h and k scans through in-plane Bragg reflections obtained from the X-ray map shown in Fig. 5.8(c). The vertical axis shows the logarithm of the intensity. The FWHM of these reflections is quite small, on the order of 0.05 reciprocal lattice units, however, in logarithmic scale we see additional broad tails. The blue curve is a Lorentzian fit to the logarithm of the intensity. We find that such a fit reproduces the overall shape of all peaks very well. Besides the good fit, we do not have a physical argument for the choice of the fitting function. However, it allows us to deduce an asymptotic behavior from it.

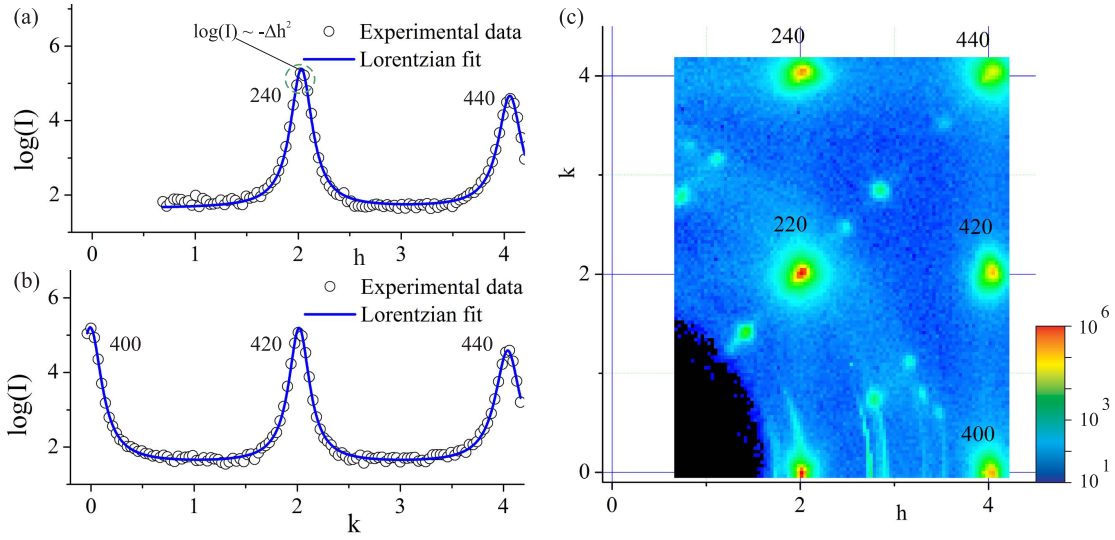

Figure 5.8: (a) k=4, l=0 scan through Bragg reflections. Logarithm of intensity is fitted by two Lorenzian peaks (blue curves) (b) Same as in (a) but for h=4, l=0 scans through Bragg reflections. (c) In-plane X-ray map on a logarithmic scale shows regions in reciprocal space free of polycrystal and misoriented phase peaks.

Our fitting function is

$$I(\Delta q) = e^{1/(\Delta q^2+1)}.$$

For $\Delta q \to q$, where q is the scattering vector at the peak center, the Lorentzian exponential term can be approximated by the Taylor series:

$$1/(\Delta q^2 + 1) = 1 - \Delta q^2 + O(\Delta q^4).$$

In this case, our fitting function becomes

$$I(\Delta q) \approx e^{1-\Delta q^2}, \Delta q \to q$$

which is Gaussian. This is may be the reason why our fitting function fits well to the central Gaussian parts. Gaussian profiles could be explained more easily by strained grains present in the film. We will return to this question later.

Analogously, we can take the Taylor expansion of the peak function for $\Delta q \to \infty$:

$$I(\Delta q) = e^{1/(\Delta q^2+1)} \approx 1 + \frac{1}{\Delta q^2} + O(\frac{1}{\Delta q^4}), \Delta q \to \infty$$

Such asymptotic behavior has been noticed in scattering from crystals with point defects [100, 101, 102, 103] and in thermal diffuse scattering. Since we have a high density of vacancies in GeTe-Sb_2Te_3 alloys which may act as point defects, such an asymptotic behavior could be produced. However, point defects do not affect long range periodicity and thus produce sharp Bragg peaks. Thus, point defects cannot explain the broad central parts of the peak.

Let us now turn to an additional feature commonly seen in X-ray maps from our phase-change alloys. This is an interesting peak main axes aligned with the crystallographic directions. These observations will lead to an explanation for the source of the broadening.

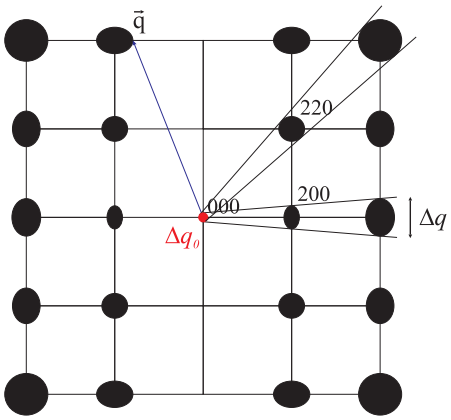

Figure 5.9: Full widths at half max (FWHM) of different in-plane $(h, k, 0)$ reflections. The peaks have elliptic shapes. Each ellipse main axes equals the FWHM of the corresponding h or k scans. The spots are magnified by a factor of 10.

Figure 5.9 shows the observed anisotropic peak shapes depending on crystallographic direction. We see that the FWHMs of each peak in the h and k directions are different, and, in general, grow with the scattering vector $\vec{q}$. The data is taken from the same sample as the X-ray map shown in Fig. 5.8(c). From this mesh we see that the main axes of the ellipses are aligned with the (010) or (100) directions.

Figure 5.10 demonstrates that the problem is three-dimensional. The peaks possess an ellipsoidal broadening in 3D reciprocal space.

The data of Fig. 5.10 is obtained from linear scans through the peaks along h,k and l. We therefore do not know whether the ellipsoid main axes are always aligned along

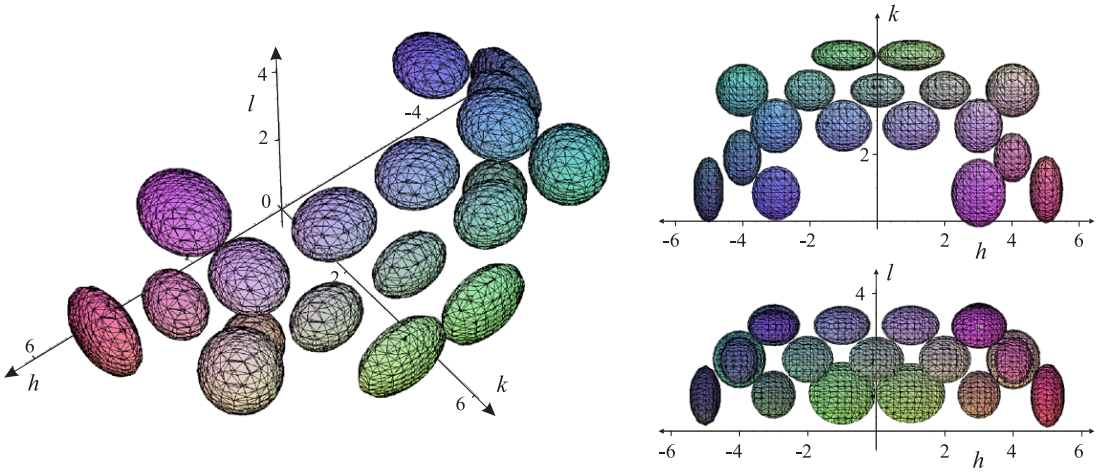

Figure 5.10: Full widths at half max (FWHM) of different integer order reflections. The ellipsoid centers coincide with the positions of the reflections. Each ellipsoid has a major axis diameter equal to the FWHMs of the corresponding h,k or l-scans, with a scale factor of 20.

h, k or l. This is so for the case of Fig. 5.8(c). However, the mesh scan in Fig. 4.9 also demonstrates ellipsoidal Bragg peaks, but with the main axes either along or orthogonal to the scattering vector $\vec{q}$.

Considering all our observations, we can suggest the following model. It has been reported that the structure of GeTe at room temperature is rhombohedral [32], with a rhombohedral angle of 88.18 °. GeTe is the prototype of GST and represents one of the endpoints of the GeTe-Sb_2Te_3 pseudobinary line. Therefore, we think that our film has a rhombohedral distortion as well. When the rhombohedral unit cell is placed on a cubic substrate it becomes strained. As soon as the strain relaxes, it is energetically favorable to align at least one of the axes of the rhombohedral unit cell with one of the crystallographic directions of the cubic substrate. During epitaxy, nucleation and growth starts at different places on the surface, thus the relaxation and alignment for each individual nucleation center occurs in an arbitrary direction. Figure 5.11(a) shows the four possibilities to place a rhombic unit cell on a square substrate epitaxially. The resultant diffraction pattern should then have four additional Bragg reflections at each Bragg point of the substrate, as schematically shown in Fig. 5.11(b). The rhombohedral angle for Fig. 5.11(b) is 88.18 °. However, due to the small rhombohedral distortion, incomplete strain relaxation and elastic interaction between individual grains and the substrate, the film is forced to have the cubic lattice on average. X-ray scattering from the grains results in an averaged diffraction pattern as shown in Fig. 5.11(c).

If the third dimension is considered, then there are eight possibilities to place the rhombohedral unit cell onto the cubic substrate, resulting in eight reciprocal lattices. After averaging the resultant reflections would be ellipsoidal, with the alignment along the h,k and l crystallographic directions.

It is worth to note here that the model does not explain the broadening of reflections like 020 and 040 along the scattering vector $\vec{q}$ and a constant contribution to the broadening, which does not depend on the order of the reflection (see Fig. 5.9). How-

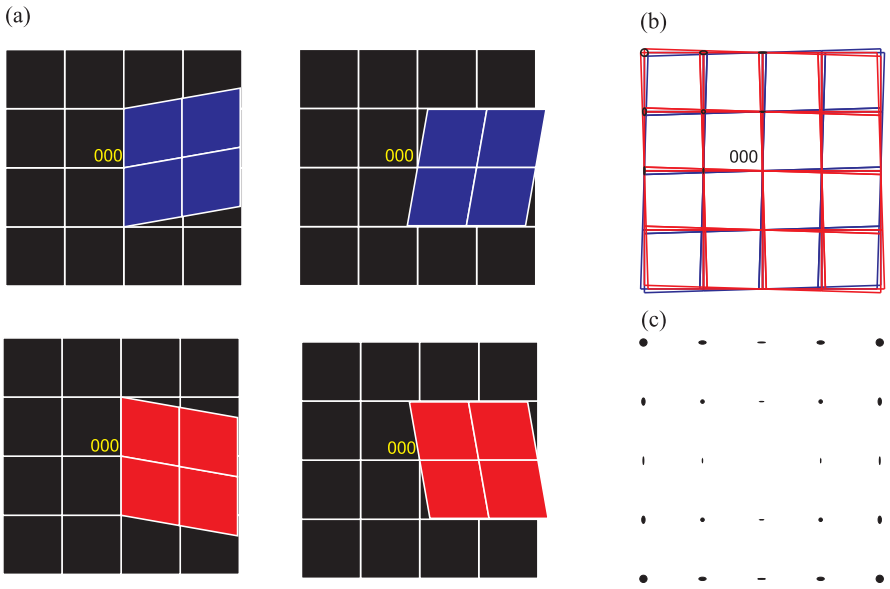

Figure 5.11: Mechanism of the broadening due to rhombohedral elongation of the film unit cell. (a) different limiting in-plane orientations, (b) superimposed reciprocal lattices for these four cases (c) resulting broadening.

ever this can be explained within the framework of the standard models for strain- and size-induced broadening. The analysis is discussed below.

5.3.3 Broadening due to strain, size and distortion effects

Peak broadening was the topic of intense scientific discussions since the 1940[s], when scientists observed broad reflections of cold worked metals [106, 107, 108, 109, 96, 95, 110]. They found that the Scherrer X-ray line broadening due to small particle size is not applicable to cold worked metals. Instead, the strain introduced into the crystals by the work produced even stronger X-ray line broadening than could be explained by the size of the crystalline aggregates. For cases in which both effects are present, Willamson and Hall [110] proposed a method for separating the two contributions. They suggested to plot peak width over scattering vector and approximate it by a line. The intersection of the linear fit with y-axis gives the apparent particle size, while slope of the curve gives the apparent strain. The geometry of the experiment were simple ω-2θ scans from powder samples.

Since we are using single crystalline (or at least strongly oriented) films with rhombohedral distortion and hkl scans, we have to adopt the Willamson-Hall method for our purposes.

Figure 5.12 shows the geometry of an ω-2θ scan in reciprocal space. It is easy to see that the ω-2θ scan represents a radial scan in reciprocal space along the scattering vector $\vec{q}$. We now want to relate the width of the peak in reciprocal space units to the angular width of the peak to be able to use hkl scans. For the peak width Δq=$\vec{q}_2$–$\vec{q}_1$ the following relation is valid:

$$\Delta\vec{q} = 2|\vec{k}_i|(\sin(\theta_1 + \beta/2) - \sin(\theta_1)) \tag{5.5}$$

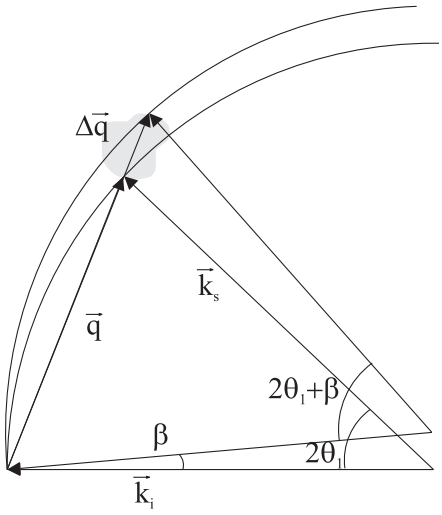

Figure 5.12: A radial scan in reciprocal space is an ω-2θ scan in real space

where β is the angular FWHM of the peak expressed in radians. Since the width of the peak β is much smaller then the scattering angle θ we can write:

$$\Delta q = |\vec{k_i}| \cos(\theta)\beta \tag{5.6}$$

For the pure particle size broadening, the Scherrer [51] formula is valid:

$$\beta_p = \frac{\lambda}{L_{hkl} \cos\theta} \tag{5.7}$$

where L_{hkl} is the apparent particle size in the hkl direction. Substituting 5.7 into 5.6 and taking into account that $|\vec{k_i}|=2\pi/\lambda$ we get the uncertainty principle:

$$\Delta q \cdot L = 2\pi \tag{5.8}$$

which is obvious, since it comes directly from the Fourier transform of the crystal shape function. If we look carefully at the interference function (2.20) of a parallelepiped crystal, we clearly see that the shape of all peaks in reciprocal space is the reciprocal of the parallelepiped shape of the crystal.

The main conclusion here is that for pure particle size broadening, the width of the peaks in hkl scans *does not depend* on the scattering vector length q.

Analogously, for pure strain broadening, Stokes and Wilson [106, 107, 108] have shown that

$$\beta_s = 2\epsilon \tan\theta \tag{5.9}$$

where ϵ is the width of the strain distribution function orthogonal to diffracting planes. Substituting 5.9 into 5.6 and remembering that $|\vec{q}| = 2|\vec{k_i}| \sin\theta$ we have the following relation of the full width Δq:

$$\Delta q = \epsilon q \tag{5.10}$$

The idea is that in the case of pure strain, the peak widths along the scattering vector

in reciprocal space increase *linearly* with $\vec{q}$.

In the presence of both size and strain effects, Williamson and Hall suggested a method for separating the two effects. Depending on strain and particle size statistical distribution functions (Cauchy or Gaussian), one can just add the linear or squared integral breadths β_p and β_s. We found best linear behavior for our case if we plot Δq^2 over q^2. What is different from polycrystals, we can do it for various orientations separately. For $\Delta\vec{q}$, in addition to the widths of $\omega - 2\theta$ scans parallel to the vector $\vec{q}$, we also plot the widths of ω scans orthogonal to $\vec{q}$.

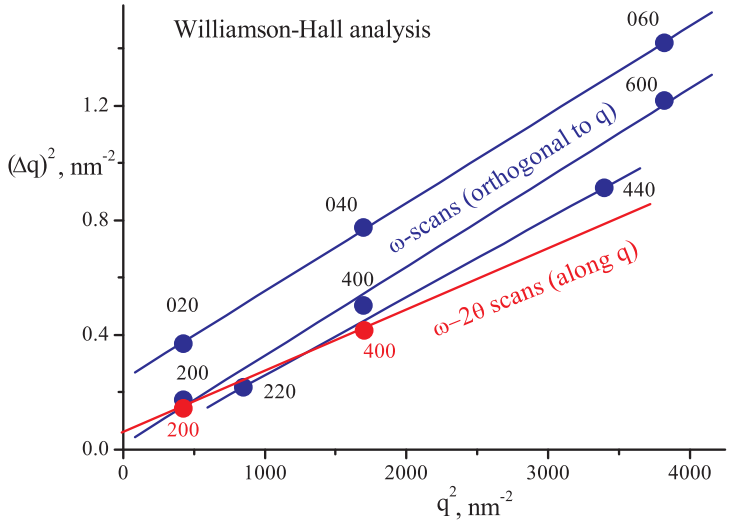

Figure 5.13: The FWHM of various reflections depending on the length of the scattering vector $\vec{q}$. Blue points are the peak widths orthogonal to the scattering vector $\vec{q}$. Red points are the widths along the scattering vector.

Figure 5.13 shows such a Williamson-Hall plot for various in-plane reflections. We see that in general the peak widths increase with the scattering vector $\vec{q}$ and the slope of the linear fit depends on the scan direction. For the reflections of the main crystallographic directions h or k like 020 and 200 the effects of rhombohedral and tensile strain are separable (see Fig. 5.11(c)). For the orthogonal scan direction, the slope is entirely represented by the average rhombohedral angle distortion of the unit cell. The value for the rhombohedral distortion is 0.46 °. This is four times smaller than the reported distortion of the GeTe unit cell and may be due to the presence of Sb in the structure. For the scans along the scattering vector $\vec{q}$, the slope yields an apparent tensile strain of 1.3%, which is 0.3% larger than the lattice mismatch between the GST and GaSb. This finding implies additional source of strain.

A constant contribution to the broadening gives the apparent grain size of approximately 30 nm. Due to a strong lattice distortions, reducing the accuracy of the constant determination, this value is not reliable.

6 Summary

Epitaxial growth of Ge-Sb-Te (GST) alloys on GaSb(001) substrates was studied in this work. The growth process was monitored by grazing incidence X-ray diffraction (GIXRD) and reflection high energy electron diffraction (RHEED) in real time. The analysis allows us to distinguish four different growth regimes of GST on GaSb(001): amorphous, polycrystalline, incubated epitaxial and direct epitaxial.

At relatively low temperatures below 100 °C, the film grows in the amorphous phase. At these growth temperatures, the film possesses a rather smooth morphology. The deposited material completely sticks to the surface, without significant sublimation.

In the temperature range of 100–160 °C the film grows polycrystalline. It has the lowest density of 4.5 g/cm^3 at these growth conditions, indicating a porous growth.

Epitaxial growth is observed for substrate temperatures of 180–210 °C. Initially, a 0.6 nm thick amorphous layer forms on the surface, which after a certain incubation time or critical thickness crystallizes epitaxially. The RHEED and XRD measurements confirm the cube-on-cube epitaxial relationship between the GST layer and the substrate. At these growth conditions, *in situ* XRD confirm continuous epitaxial growth without degradation of crystallinity and loss of orientation for thicknesses up to 70 nm. The determined lattice constant of the film is 6.01 Å, close to that of metastable GST and GeTe. The film exhibits the roughest surface morphology due to 3D growth and the highest density close to that of the metastable GST at these growth conditions. X-ray diffraction reveals some fraction of 45 ° rotated and <111> oriented cubic GST domains present in the film. The determined growth rate was normalized to the ratio of measured and tabulated GST film density. The normalized growth rate is 0.3 nm/min at these temperatures, which is half the flux rate of 0.6 nm/min, implying significant sublimation of the film.

For growth temperatures above 220 °C, the film grows epitaxially from the very beginning, however the growth rate rapidly decreases with temperature due to the high vapour pressure of the film. At these growth conditions, the disorder in the film accumulates with the layer thickness leading to completely amorphous growth for layer thicknesses of approximately 20 nm. For growth temperatures above 270 °C, the observed growth rate is zero.

The composition of the films determined from X-ray fluorescence on reference samples rapidly approaches the 2:2:5 ratio for Ge, Sb and Te, respectively.

The crystal structure of the films grown in the incubated epitaxial regime was analyzed in this work. The reciprocal lattice of the film has a body centered cubic (BCC) symmetry with two types of reflections indicating a face centered cubic (FCC) crystal with two sublattices as in sodium chloride. The averaged electron density ratio in the two FCC sublattices is the same as the one in GeTe or metastable GST with 20 % vacancies. We do not observe atoms on tetrahedrally coordinated sites of the crystal.

The analysis of X-ray peaks demonstrates anisotropic (ellipsoidal) peak shapes aligned in reciprocal space along the h,k and l crystallographic directions. The broadening in-

creases with the order of the reflection. The phenomenon is explained by the rhombohedral distortion of the cubic unit cell of the metastable GST. The results give a rhombohedral angle of 89.54 °. The peak broadening has a constant contribution due to the film granularity with an apparent grain size of 30 nm. An average tensile strain of 1.3 % is also detected in the film due to GST and GaSb lattice mismatch and compositional inhomogeneity.

A new experimental method for the determination of the integrated intensity of the X-ray reflections from epitaxial GST films is developed in this work. The method can be applied to any epitaxial films having very broad Bragg reflections, which cannot be captured entirely by the active area of the X-ray detector. The necessary theoretical basis and the geometrical corrections are derived. The validity of the method has been experimentally proven.

For automated diffractometers which use reciprocal space coordinates for navigation in reciprocal space, a motor synchronization algorithm is proposed in this work. This algorithm allows to automatically set the necessary diffractometer motor speeds to move along a certain direction in reciprocal space. For the case of asynchronous motor movements, the maximum deviation from a given direction in reciprocal space is calculated. The results demonstrate that for certain cases, the data can also be acquired during motor movements without introducing errors. The method has been implemented for our six circle diffractometer, and the validity of the approach has been demonstrated during reciprocal space mapping experiments.

Bibliography

[1] G. E. Moore. Craming more components into integrated circuit. *Electronics*, 38, 1965.

[2] *International Technology Roadmap for Semiconductors http://www.itrs.net/Links/2007ITRS/ExecSum2007.pdf*, 2007.

[3] G. I. Meijer. Who wins the non-volatile memory race? *Science*, 319:1625, 2008.

[4] Baccarani G. and Reggiani S. Performance limits of cmos technology and perspectives of quantum devices. *Comptes Rendus de lÁcademie des Sciences - Series IV - Physics*, 1:843, 2000.

[5] Rairigh D. Limits of cmos technology scaling and technologies beyond-cmos. *Institute of Electrical and Electronics Engineers, Inc.*, 2005.

[6] T. Ohta. Phase-change optical memory promotes the dvd optical disk. *Journal of Optoelectronics and Advanced Materials*, 3:609, 2001.

[7] E. Ohno, N. Yamada, T. Kurumizawa, K. Kimura, and M. Takao. Tegesnau alloys for phase change type optical disk memories. *Japanese Journal of Applied Physics*, 28:1235, 1989.

[8] N. Yamada, E. Ohno, K. Nishiuchi, N. Akahira, and M. Takao. Rapid-phase transitions of gete-sb_2te_3 pseudobinary amorphous thin films for an optical disk memory. *Journal of Applied Physics*, 69:2849, 1991.

[9] D. J. Adelerhof. Media development for dvd+rw phase change recording. In *European Phase Change and Ovonics Symposium*, 2004.

[10] K. Yusu, T. Nakai, S. Ashida, N. Ohmachi, N. Morishita, and N. Nakamura. High speed crystallization characteristics of ge-sb-te-bi used for next generation rewritable dvd with blue laser na=0.65. In *European Phase Change and Ovonics Symposium*, 2005.

[11] S. R. Ovshinsky. Reversable electrical switching phenomena in disordered structures. *Physical Review Letters*, 21:1450, 1968.

[12] P. Fons and A. V. Kolobov. Sub-nanosecond time-resolved structural measurements of the phase-change alloy ge_2sb_2te_5. *Japanese Journal of Applied Physics*, 46:3711, 2007.

[13] S. L. Cho, H. Horii, and J. H. Park. A novel cell technology using n-doped gesbte films for phase change ram. *Symposium on VLSI Technology Digest of Technical Papers*, 2003.

[14] S. Lai and T. Lowrey. Oum-a 180 nm non-volatile memory cell element technology for stand alone and embedded applications. *International Electron Devices Meeting*, 100:803, 2001.

[15] Y. C. Chen, S. Raoux, and M. Wuttig. *Phase Change Materials: science and applications*, chapter 15, pages 331–354. Springer, 1st edition, 2009. ISBN 978-0-387-84873-0.

[16] F. Jedema. Designing optical media of the future. *Nature Materials*, 6:90, 2007.

[17] M. Wuttig. Towards a universal memory? *Nature Materials*, 4:265, 2005.

[18] Wuttig M. and Yamada N. Phase change materials for rewritable data storage. *Nature Materials*, 6:824, 2007.

[19] A. V. Kolobov and P. Fons. Understanding the phase-change mechanism of rewritable optical media. *Nature Materials*, 3:703, 2004.

[20] T. Matsunaga and N. Yamada. Structural investigation of gesb_2te_4: A high-speed phase-change material. *Physical Reviev B*, 69:103111, 2004.

[21] W. Braun, R. Shayduk, T. Flissikowski, M. Ramsteiner, H. T. Grahn, H. Riechert, A. Kolobov, and P. Fons. Epitaxy of ge-sb-te phase change memory alloys. *Applied Physic Letters*, 94:041902, 2009.

[22] R. Shayduk and W. Braun. Epitaxial films for ge-sb-te phase change memory. *Journal of Crystal Growth*, 311:2215, 2009.

[23] R. Shayduk and W. Braun. Positioning errors during stepped scans in x-ray crystallography. *Journal of Applied Crystallography*, 41:768, 2008.

[24] V. M. Kaganer, B. Jenichen, R. Shayduk, W. Braun, and H. Riechert. Kinetic optimum of volmer-weber growth. *Physical Rewiev Letters*, 102:016103, 2009.

[25] V. M. Kaganer, B. Jenichen, R. Shayduk, and W. Braun. Structure of fe_3si/gaas(001) epitaxial films from x-ray crystal truncation rods. *Physical Review B*, 7:125325, 2008.

[26] W. Welnic and M. Wuttig. Reversible switching in phase-change materials. *Materials Today*, 11:20, 2008.

[27] D. Lencer, M. Salinga, B. Grabowski, T. Hickel, J. Neugebauer, and M. Wuttig. A map for phase change materials. *Nature Materials*, 7:972, 2008.

[28] J. Feinleib, J. deNeufville deNeufville, S. C. Moss, and S. R. Ovshinsky. Rapid reversable light-induced crystallization of amorphous semiconductors. *Applied Physics Letters*, 18:25, 1971.

[29] D. Adler, H. K. Henisch, and S. N. Mott. The mechanism of threshold switching in amorphous alloys. *Reviews of Modern Physics*, 50:209, 1978.

[30] J. Siegel, A. Schropp, J. Solis, and C. N. Afonso. Rewritable phase-change optical recording in ge_2sb_2te_5 films induced by picosecond laser pulses. *Applied Physics Letters*, 84:2250, 2004.

[31] N. Kh. Abrikosov and G. T. Danilova-Dobryakova. An investigation of the structural diagram of sb_2te_3-gete. *Izvestiya Akademii Nauk SSSR, Neorganicheskie Materialy*, 1:187, 1964.

[32] J. Goldak and C. S. Barret. Structure of alpha gete. *Journal of Chemical Physics*, 44:3323, 1965.

[33] E. Donges. Uber tellurohalogenide des dreivertigen antimons und wismuts und uber antimon- und wismut(iii)-tellurid und wismut(iii)-selenide. *Zeitschrift fur anorganische und allgemeine Chemie*, 265:56, 1951.

[34] N. Yiwata, M. Harigaya, K. Tani, K. Hayakawa, and T. Fujikawa. Sb k-edge absorption fine structure of sb_2te_3. *Journal of Synchrotron Radiation*, 8:752, 2001.

[35] T. Matsunaga, N. Yamada, and Y. Kubota. Structures of stable and metastable ge_2sb_2te_5, an intermetallic compound in gete-sb_2te_3 pseudobinary systems. *Acta Crystallographica*, B60:685, 2004.

[36] N. Yamada and T. Matsunaga. Structure of laser-crystallized ge_2sb_$2 + x$te_5 sputtered thin films for use in optical memory. *Journal of Applied Physics*, 88: 7020, 2000.

[37] T. Matsunaga and N. Yamada. A study of highly symmetrial crystal structures, commonly seen in high-speed phase-change materials, using synchrotron radiation. *Japan Journal of Applied Physics*, 41:1674, 2002.

[38] I. I. Petrov, R. M. Imamov, and Z. G. Pinsker. Electron-diffraction determination of the structures of ge_2sb_2te_5 and gesb_4te_7. *Soviet Physics - Crystallography*, 13:339, 1968.

[39] K. A. Agaev and A. G. Talybov. Electron-diffraction analysis of the structure of gesb_2te_4. *Soviet Physics - Crystallography*, 11:400, 1966.

[40] J. L. F. Da Silva, A. Walsh, and H. Lee. Insights into structure of the stable and metastable (gete)_m(sb_2te_3)_n compounds. *Physical Review B*, 78:224111, 2008.

[41] Z. Sun, S. Kyrsta, D. Music, R. Ahuja, and J. M. Schneider. Structure of the ge-sb-te phase-change materials studied by theory and experiment. *Solid State Communications*, 143:240, 2007.

[42] S. Kohara, K. Kato, S. Kimura, and H. Tanaka. Structural basis for the fast phase change of ge_2sb_2te_5: Ring statistics analogy between the crystal and amorphous states. *Applied Physics Letters*, 89:201910, 2006.

[43] J. Akola and R. O. Jones. Structural phase transitions on the nanoscale: The crucial pattern in the phase-change materials ge_2sb_2te_5 and gete. *Physical Review B*, 76:235201, 2007.

[44] J. Akola and R. O. Jones. Binary alloys of ge and te: Order, voids, and the eutectic composition. *Physical Review Letters*, 100:205502, 2008.

[45] J. Hegedus and S. R. Elliot. Microscopic origin of the fast crystallization ability of ge-sb-te phase change memory materials. *Nature Materials*, 7:399, 2008.

[46] D. C. Koningsberger and R. Prins. *X-ray Absorption: Principles, Applications, Techniques of EXAFS, SEXAFS and XANES*. Chemical Analysis. Wiley, 1988.

[47] L. Pauling. *The Nature of The Chemical Bond*. Cornell University Press, New York, Ithaca, 3 edition, 1960. ISBN 978-0801403330.

[48] E. T. Kim and J. Y. Lee. Investigation of structural sransformation of ge_2sb_2te_5 thin films using high resolution electron microscopy. *Applied Physic Letters*, 91:101909, 2007.

[49] Y. J. Park. In situ transmission electron microscopy study of the nucleation and grain growth of ge_2sb_2te_5 thin films. *Applied Surface Science*, 252:8102, 2006.

[50] S. Elliot, S. Raoux, and M. Wuttig. *Phase Change Materials: science and applications*, chapter 4, pages 63–79. Springer, 1st edition, 2009. ISBN 978-0-387-84873-0.

[51] B. E. Warren. *X-ray diffraction*. Dover Publications, 1990. ISBN 978-0486663175.

[52] J. M. Cowley. *Diffraction physics*. North Holland, 3 edition, 1995. ISBN 978-0444822185.

[53] A. A. Sokolov and I. M. Ternov. Synchrotron radiation. *Soviet Physics Journal*, 10:66, 1967.

[54] E. Vlieg. Integrated intensities using a six-circle surface x-ray diffractometer. *Journal of Applied Physics*, 30:532, 1997.

[55] D. Waasmaier and A. Kirfel. *Acta crystallographica*, A51:413, 1995.

[56] *International tables for Crystallography*, C, 1992.

[57] S. Brennan and P. L. Cowan. *Rev. Sci. Instrum.*, 63:850, 1992.

[58] Henke B. L., Gullikson E. M., and Davis J. C. X-ray interactions: photoabsorption, scattering, transmission, and reflection at e=50-30000 ev, z=1-92. *Atomic Data and Nuclear Data Tables*, 54:181, 1993.

[59] M. A. Krivoglaz. *Diffraction of X-rays and neutrons in nonideal crystals*. Springer-Verlag Berlin Heidelberg New York, 1996. ISBN 3-540-50564-4.

[60] D. J. Srolovitz. On the stability of surfaces of stressed solids. *Acta Metallurgica*, 37:621, 1989.

[61] M. I. Richard, T.-U. Schülli, E. Wintersberger, G. Renaud, and G. Bauer. In situ ivestigation by gisaxs and gixd of the growth mode, strain state and shape of ge islands during their growth on si(001). *Nuclear Instruments in Physics Research B*, 246:35, 2006.

[62] I. N. Stranski and L. V. Krastanow. *Abhandlungen der Mathematisch-Naturwissenschaftlichen Klasse. Akademie der Wissenschaften und der Literatur in Mainz*, 146:797, 1939.

[63] B. Jenichen, W. Braun, V. M. Kaganer, A. G. Shtukenberg, L. Daweritz, C.-G. Schulz, and K. H. Ploog. Combined molecular beam epitaxy and diffractometer system for *in situ* x-ray studies of crystal growth. *Review of Scientific Instruments*, 74:1267, 2003.

[64] C. Schamper, H. L. Meyerheim, and W. Moritz. Resolution correction for surface x-ray diffraction at high beam exit angles. *Journal of Applied Crystallography*, 26: 687, 1993.

[65] E. D. Specht and F. J. Walker. A method for the accurate determination of crystal truncation rod intensities by x-ray diffraction. *Journal of Applied Crystallography*, 26:166, 1993.

[66] O. Robach, Y. Garreau, K. Aid, and M. B. Véron-Jolliot. Corrections for surface x-ray diffraction measurements using z-axis geometry: finite size effects in direct and reciprocal space. *Journal of Applied Crystallography*, 33:1006, 2000.

[67] X. Torrelles and J. Rius. Faster acquisition of structure-factor amplitudes in surface x-ray diffraction experiments. *Journal of Applied Crystallography*, 37:395, 2004.

[68] N. Jedrecy. Coupling between spatial and angular variables in surface x-ray diffraction: effects on the line shapes and integrated intensities. *Journal of Applied Crystallography*, 33:1365, 2000.

[69] D.-M. Smilgies. Geometry-independent intensity correction factors for grazing-incidence diffraction. *Review of Scientific Instruments*, 73:1706, 2002.

[70] M. F. Toney and D. G. Weisler. Instrumental effects on measurements of surface x-ray diffraction rods: Resolution function and active sample area. *Acta Crystallographica*, A49:624, 1993.

[71] *Certified Scientific Software SPEC.* PO Box, 390640, Cambridge, MA 02139, USA, 2008. URL `www.certif.com`. The diffractometer control software SPEC by Certified Scientific Software, Inc.

[72] G. M. Fikhtengoltz. *Course of differential and integral calculus (*In Russian*).* FIZMATLIT, 8 edition, 2003. ISBN 5-9221-0158-7.

[73] M. Lohmeier and E. Vlieg. Angle calculations for a six-circle x-ray diffractometer. *Journal of Applied Crystallography*, 26:706, 1993.

[74] W. R. Busing and H. A. Levy. Angle calculations for 3- and 4- circle x-ray and neutron diffractometers. *Acta Crystallographica*, 22:457, 1967.

[75] B. Z. Nosho, B. R. Bennet, E. H. Aifer, and M. Goldenberg. *Journal of Crystal Growth*, 236:155, 2002.

[76] F. Maeda, M. Sugiyama, and Y. Watanabe. *Physical Review B*, 62:1615, 2000.

[77] W. Braun. *Applied RHEED: Reflection High-Energy electron Diffraction During Crystal Growth*. Springer-Verlag Berlin Heidelberg New York, 1999. ISBN 3-540-65199-3.

[78] O. Romanyuk, V. M. Kaganer, R. Shayduk, B. P. Tinkham, and W. Braun. Staircase model of gasb(001) (1x3) and c(2x6) phases. *Physical Review B*, 77:235322, 2008.

[79] S. Huang, Z. Niu, Z. Fang, H. Ni, Z. Gong, and J. Xia. Complex quantum ring structures formed by droplet epitaxy. *Applied Physics Letters*, 89:031921, 2006.

[80] W. Braun, H. Möller, and Y. H. Zhang. Reflection high-energy electron diffraction during substrate rotation: A new dimension for *in situ* characterization. *Journal of Vacuum Science Technology B*, 16(3):1507, 1998.

[81] M. H. R. Lankhorst, B. W. Ketelaars, and R. A. M. Wolters. Low-cost and nanoscale non-volatile memory concept for future silicon chips. *Nature Materials*, 4:347, 2005.

[82] W. K. Njoroge, H. W. Woltgens, and M. Wuttig. Density changes upon crystallization of ge_2sb_2.04te_4.74 films. *Journal of Vacuum Science Technology A*, 20:230, 2002.

[83] J. A. Venables. *Introduction to Surface and Thin Film Processes*. Cambridge University Press, 1 edition, 2008. ISBN 978-0521785006.

[84] A. D. McNaught and A. Wilkonson. *IUPAC. Compendium of Chemical Terminology*. Blackwell Scientific Publications, Oxford, 2 edition, 1997. ISBN 0-9678550-9-8. URL `http://goldbook.iupac.org`.

[85] F. Rosebury. *Handbook of Electron Tube and Vacuum Techniques*. American Institute of Physics, 1 edition, 1992. ISBN 978-1563961212. URL `http://www.amazon.com/gp/product/1563961210`.

[86] M. Yano, K. Yamamoto, T. Utatsu, and M. Inoue. Reflection high-energy electron diffraction study of gasb surface during molecular beam epitaxy. *Journal of Vacuum Science Technology B*, 12(2):1133, 1994.

[87] C. Kittel. *Introduction to Solid State Physics*. Wiley, 7 edition, 1995. ISBN 978-0471111818.

[88] W. Welnic, A. Pamungkas, R. Detemple, C. Steimer, S. Bluegel, and M. Wuttig. Unravelling the interplay of local structure and physical properties in phase-change materials. *Nature Materials*, 5:56, 2006.

[89] N. Yamada and T. Matsunaga. Studies of high-speed phase-change materials using synchrotron radiation. In *European Phase Change and Ovonics Symposium*, 2003.

[90] T. Nonaka, G. Ohbayashi, Y. Toriumi, Y. Mori, and H. Hashimoto. Crystal structure of gete and ge_2sb_2te_5 meta-stable phase. *Thin Solid films*, 370: 258, 2000.

[91] I. D. Feranchuk, L. I. Gurskii, L. I. Komarov, O. M. Lugovskaya, F. Burgaez, and A. Ulyanenkov. A new method for calculation of crystal susceptibilities for x-ray diffraction at arbitrary wavlength. *Acta Crystallographica*, A58:370, 2002.

[92] M. Wuttig, D. Lüsebrink, D. Wamwangi, W. W. Strokenic, M. Gilles, and R. Dronskowski. The role of vacancies and local distortions in the design of new phase-change materials. *Nature Materials*, 6:122, 2007.

[93] T. H. de Keijser, J. I. Langford, E. J. Mittemeijer, and A. B. P. Vogels. Use of the voigt function in a single-line method for the analysis of x-ray diffraction line broadening. *Journal of Applied Crystallography*, 15:308, 1982.

[94] R. A. Young and D. B. Wiles. Profile shape functions in rietveld refinements. *Journal of Applied Crystallography*, 15:430, 1982.

[95] B. E. Warren and B. L. Averbach. The effect of cold-work distortion on x-ray patterns. *Journal of Applied Physics*, 21:595, 1950.

[96] B. E. Warren and B. L. Averbach. The separation of cold work distortion and particle size broadening in x-ray patterns. *Journal of Applied Physics*, 23:497, 1952.

[97] H. M. Rietveld. Line profiles of neutron powder-diffraction peaks for structure refinement. *Acta Crystallographica*, 22:151, 1967.

[98] D. Balzar. Profile fitting of x-ray diffraction lines and fourier analysis of broadening. *Journal of Applied Crystallography*, 25:559, 1992.

[99] H. Ledbetter D. Balzar. Voigt-function modeling in fourier analysis of size- and strain-broadened x-ray diffraction peaks. *Journal of Applied Crystallography*, 26: 97, 1993.

[100] M. Moreno, B. Jenichen, V. Kaganer, W. Braun, A. Trampert, L. Daweritz, and K. H. Ploog. Mnas nanoclusters embedded in gaas studied by x-ray diffuse and coherent scattering. *Physical Review B*, 67:235206, 2003.

[101] P. H. Dederichs. Diffuse scattering from defect clusters near bragg reflections. *Physical Review B*, 4:1041, 1971.

[102] P. H. Dederichs. The theory of diffuse x-ray scattering and its application to the study of point defects and their clusters. *Journal of Physics F: Metal Physics*, 3: 471, 1973.

[103] H. Peisl. Diffuse x-ray scattering from the displacement field of point defects and defect clusters. *Journal of Applied Crystallography*, 8:143, 1975.

[104] I. Groma. X-ray line broadening due to an inhomogeneous dislocation distribution. *Physical Review B*, 57:7535, 1998.

[105] V. M. Kaganer, A .Shalimov, J. Bak-Misiuk, and K. H. Ploog. Asymptotic x-ray scattering from highly mismatched epitaxial films. *Journal of Physics: Condensed Matter*, 18:5047, 2006.

[106] A. R. Stokes and A. J. C. Wilson. A method of calculating the integral breadths of debye-scherrer lines: generalization to non-cubic crystals. *Mathematical Proceedings of the Cambridge Philosophical Society*, 40:197, 1944.

[107] A. R. Stokes and A. J. C. Wilson. The diffraction of x-rays by distorted crystal aggregates - i. *Proceedings of the Physical Society*, 56:174, 1944.

[108] A. J. C. Wilson. The diffraction of x-rays by distorted-crystal aggregates. ii. diffraction by bent lamellae. *Acta Crystallographica*, 2:220, 1949.

[109] B. E. Warren, B. L. Averbach, and B. W. Roberts. Atomic size effect in x-ray scattering by alloys. *Journal of Applied Physics*, 22(12):1493, 1951.

[110] G. K. Williamson and W. H. Hall. X-ray line broadening from filed aluminium and wolfram. *Acta Metallurgica*, 1:22, 1953.

[111] S. Privitera, E. Rimini, C. Bongiorno, R. Zonca, A. Pirovano, and R. Bez. Crystallization and phase separation in ge_2 + $x$sb_2te_5. *Journal of Applied Physics*, 94(7):4409–4413, 2003.

[112] Roman Shayduk. Use of linear scans to obtain f_hkl^2 and the integrated intensity. *Journal of Applied Crystallography*, 43:1121–1123, 2010.

[113] Simone Raoux. Phase change materials. *Annual Reviews of Materials Research*, 39:25–48, 2009.

[114] V. M. Kaganer, R. Köhler, M. Schmidbauer, and R. Opitz. X-ray diffraction peaks due to misfit dislocations in heteroepitaxial structures. *Physical Review B*, 55:1793, 1997.

[115] V. M. Kaganer, O. Brandt, A. Trampert, and K. H. Ploog. X-ray diffraction peak profiles from threading dislocations in gan epitaxial films. *Physical Review B*, 72: 045423, 2005.

[116] M. A. Krivoglaz. The effect of correlation in the arrangement of dislocations on the diffraction of x-rays by deformed crystals. *Physica Metallov i Metallowedeniye*, 55:5, 1983.

[117] M. A. Krivoglaz. Theory of x-ray scattering by crystals containing dislocations, screw and edge dislocations randomily distributed throughout the crystal. *Physica Metallov i Metallowedeniye*, 15:18, 1963.

[118] H. M. Rietveld. A profile refinement method for nuclear and magnetic structures. *Journal of Applied Cystallography*, 2:65, 1969.

List of Figures

List of Tables

Acknowledgements

I would like to express my deepest gratitude to all the people I worked with...

...Prof. Dr. Klaus H. Ploog for giving me the chance to carry out my doctoral research at Paul-Drude-Institute.

...Prof. Dr. Henning Riechert for the careful reading of the manuscript.

...Dr. Wolfgang Braun for his permanent support throughout the whole work. He was the first person I really learned from how to apply high-energy electron diffraction to study the surfaces of solids. He was always willing to meet and help me with all my scientific and other problems. Moreover, I was always impressed by his optimism, enthusiasm and good life spirit. I am very grateful to him for his support.

...Dr. Bernd Jenichen for the help to understand grazing incidence X-ray diffraction, X-ray beamlines and our diffractometer. With him I gained my first experience with diffraction experiments at the synchrotron.

...Dr. Vladimir Kaganer for very many scientific discussions on the topic of X-ray scattering. His impressive theoretical background in the field and in general physics has significantly extended my outlook. He is the person I would always like to have in reach when doing any X-ray diffraction experiment.

...Dr. Tatsuro Watahiki for the great help with the X-ray experiments. It was my great pleasure to communicate with him through the whole time. He was always ready to discuss any particular scientific problems with me, even if they concerned only my work. I will certainly miss him.

...Dr. Paul Fons and Dr. Alexander Kolobov for the important discussions on the topic of this work and for the careful reading of the manuscript. Without the composition analysis of my samples they carried out this work would be incomplete.

...Dr. Frank Große for several scientific discussions and for the proofreading of this manuscript.

...Dr. Manfred Ramsteiner and Dr. Timur Flissikowski for their laser switching experiments.

...Frau Petra Grasnick for all the paperwork she did for me, especially for all the negotiations with the foreigner office, which I never liked to visit.

...Steffen Behnke and Carsten Stemmler for technical support.

...Ferhat Katmis for several X-ray measurements.

...Peter Rodenbach, André Prößdorf, Sergiy Bokoch and Brad Tinkham for the scientific and non-scientific discussions during many coffee breaks.

...Anne-Kathrin Bluhm and Claudia Herrmann for the AFM and SEM measurements.

...Frau Ilka Schuster for printing me conference posters.

Selbständigkeitserklärung

Hiermit erkläre ich, die vorliegende Arbeit selbständig ohne fremde Hilfe verfasst und nur die angegebene Literatur und Hilfsmittel verwendet zu haben.

Ich habe mich an keiner anderen Universität um einen Doktorsgrad beworben und besitze auch keinen entsprechenden Doktorsgrad.

Ich erkläre die Kenntnis der dem Verfahren zugrunde liegenden Promotionsordnung der Mathematisch-Naturwissenschaftlichen Fakultät I der Humboldt-Universität zu Berlin.

Berlin, den 26.10.2009 Roman Shayduk